



**Michigan  
Technological  
University**

Michigan Technological University  
**Digital Commons @ Michigan Tech**

---

Dissertations, Master's Theses and Master's Reports

---

2023

## **MICROSCOPIC AND LABORATORY SCALE CHARACTERIZATION METHODS TO EVALUATE BIOMASS DECONSTRUCTION**

Meenaa Chandrasekar  
*Michigan Technological University, meenaac@mtu.edu*

Copyright 2023 Meenaa Chandrasekar


---

### **Recommended Citation**

Chandrasekar, Meenaa, "MICROSCOPIC AND LABORATORY SCALE CHARACTERIZATION METHODS TO EVALUATE BIOMASS DECONSTRUCTION", Open Access Dissertation, Michigan Technological University, 2023.

<https://doi.org/10.37099/mtu.dc.etr/1603>

Follow this and additional works at: <https://digitalcommons.mtu.edu/etr>

 Part of the [Biochemical and Biomolecular Engineering Commons](#)

MICROSCOPIC AND LABORATORY SCALE CHARACTERIZATION METHODS  
TO EVALUATE BIOMASS DECONSTRUCTION

By

Meena Chandrasekar

A DISSERTATION

Submitted in partial fulfillment of the requirements for the degree of

DOCTOR OF PHILOSOPHY

In Chemical Engineering

MICHIGAN TECHNOLOGICAL UNIVERSITY

2023

© 2023 Meena Chandrasekar

This dissertation has been approved in partial fulfillment of the requirements for the Degree of DOCTOR OF PHILOSOPHY in Chemical Engineering.

Department of Chemical Engineering

Dissertation Advisor: *Dr. Rebecca G. Ong*  
Committee Member: *Dr. David R. Shonnard*  
Committee Member: *Dr. Michael R. Gretz*  
Committee Member: *Dr. Smitha Rao Hatti*  
Department Chair: *Dr. Michael E. Mullins*

## Table of Contents

List of Figures .....	vii
List of Tables .....	xiii
Author Contribution Statement.....	xiv
Acknowledgments.....	xv
Abstract.....	xvi
1 Introduction.....	1
1.1 Motivation .....	1
1.2 Research Objectives .....	2
1.2.1 Objective 1: Design and construct a microfluidic reactor for time-lapsed imaging of pretreatment and enzymatic hydrolysis of lignocellulosic biomass 3	
1.2.2 Objective 2: Utilize the imaging reactor to compare the deconstruction of hollow, semi-solid, and solid pith wheat straw cultivars.....	3
1.2.3 Objective 3: Develop a roller bottle method using gravitational mixing for high solids loading enzymatic hydrolysis.....	4
2 Background.....	5
2.1 Lignocellulosic biomass .....	5
2.1.1 Cellulose .....	5
2.1.2 Hemicellulose .....	6
2.1.3 Lignin.....	7
2.1.4 Types of lignocellulosic biomass.....	8
2.1.5 Cell wall morphology and chemical composition .....	8
2.1.6 Tissue types and cell wall composition .....	9
2.1.7 Biomass recalcitrance .....	11
2.2 Lignocellulosic biofuel production .....	12
2.2.1 Pretreatment .....	12
2.2.1.1 Dilute acid pretreatment.....	13
2.2.1.2 Dilute alkali pretreatment .....	13
2.2.1.3 AFEX pretreatment.....	14
2.2.2 Enzymatic hydrolysis.....	14
2.2.3 Fermentation .....	15
2.2.4 Analytical techniques for evaluating biomass deconstruction.....	16
2.2.5 High-solids enzymatic hydrolysis.....	16
2.2.5.1 High solids enzymatic hydrolysis configurations .....	17
2.2.5.2 Fermentation inhibition at high solids loading .....	18
2.3 Imaging in lignocellulosic biofuel production .....	19
2.3.1 Electron microscopy .....	20
2.3.2 Atomic force microscopy.....	22

2.3.3	Confocal Raman microscopy .....	22
2.3.4	Fluorescence microscopy .....	23
2.3.4.1	Lignin autofluorescence .....	24
2.3.4.2	Immunolocalization .....	25
2.4	Microfluidics .....	26
2.4.1	Important applications of microfluidics .....	27
2.4.2	Photolithography .....	28
2.4.3	PDMS microdevices in bioenergy .....	28
3	Design and construction of a microfluidic reactor for time-lapsed imaging of pretreatment and enzymatic hydrolysis of lignocellulosic biomass. ....	30
3.1	Introduction .....	30
3.2	Materials and Methods .....	31
3.2.1	SU-8 mold preparation using soft photolithography .....	31
3.2.2	Polydimethylsiloxane (PDMS) reactor prepared using the SU-8 100 mold .....	31
3.2.3	Sectioning samples using a cryomicrotome .....	32
3.2.4	Pretreatment experiments with time-lapsed imaging .....	32
3.2.5	Enzymatic hydrolysis with time-lapsed imaging .....	33
3.2.6	Immunolocalization of xylan .....	33
3.2.7	Sample preparation for pretreated biomass composition analysis .....	33
3.2.8	Acetyl bromide soluble lignin (ABSL) analysis .....	34
3.2.9	Matrix polysaccharide analysis .....	34
3.2.10	End-product analysis for pretreatment supernatant and hydrolysates .....	34
3.2.11	Confocal microscopy, image processing, and data analysis .....	34
3.2.12	Calculations .....	35
3.3	Results and Discussion .....	35
3.3.1	Initial autofluorescence signals were higher for the cell types near the vascular bundles than the parenchyma cells .....	36
3.3.2	Dilute acid pretreatment resulted in a greater decline in fluorescence in the parenchyma cells than in the vascular bundles .....	37
3.3.3	Progressive loss of fluorescence signals and swelling occurred during dilute alkali pretreatment .....	39
3.3.4	Composition of the residual biomass and the pretreatment supernatant conform to the CLSM results .....	40
3.3.5	Antibody labeling with arabinoxylan specific LM11 indicated changes in xylan during dilute acid pretreatment .....	41
3.3.6	Protoxylem cell walls were the slowest to hydrolyze during enzymatic hydrolysis of the acid and alkali pretreated samples .....	43
3.4	Conclusion .....	45
3.5	Funding .....	45
3.6	Acknowledgments .....	45

4	Will pith solidness in wheat straw increase sugar yields during enzymatic hydrolysis? .....	46
4.1	Background .....	46
4.2	Materials and Methods .....	47
4.2.1	Wheat straw samples.....	47
4.2.2	Preparation of PDMS (polydimethyl siloxane) reaction chamber .....	47
4.2.3	Sectioning samples using a cryomicrotome.....	47
4.2.4	Pretreatment experiments with time-lapsed imaging.....	48
4.2.5	Enzymatic hydrolysis with time-lapsed imaging.....	48
4.2.6	Biomass pretreatment for composition analysis .....	48
4.2.7	Acetyl bromide soluble lignin (ABSL) analysis.....	49
4.2.8	Matrix polysaccharide analysis.....	49
4.2.9	End-product analysis for pretreatment supernatant and hydrolysates 49	
4.2.10	Confocal microscopy, image processing, and data analysis .....	49
4.2.11	Calculations.....	50
4.3	Results .....	50
4.3.1	Lignin autofluorescence decrease was greatest for the protoxylem cells in the Choteau samples during dilute acid and alkali pretreatments.....	51
4.3.2	The epidermis cell wall thickness varied the most for the Choteau (solid) samples.....	55
4.3.3	Lignin removal and hemicellulose hydrolysis during pretreatment were evaluated through composition analysis.....	56
4.3.4	Glucose and xylose conversion following enzymatic hydrolysis was positively affected by stem solidness .....	57
4.3.5	Enzymatic hydrolysis images .....	59
4.4	Discussion .....	60
4.5	Conclusion.....	61
4.6	Funding.....	61
4.7	Acknowledgments .....	62
5	A high solids field to fuel research pipeline to identify interactions between feedstocks and biofuel production .....	63
5.1	Background .....	63
5.2	Materials and Methods .....	64
5.2.1	Biomass Growth, Harvest and Processing .....	64
5.2.2	Cell Wall and Bulk Chemical Composition of Biomass .....	65
5.2.3	Ammonia Fiber Expansion (AFEX) Pretreatment.....	65
5.2.4	High Solids Roller Bottle Enzymatic Hydrolysis .....	66
5.2.5	High Solids Loading Enzymatic Hydrolysis-Shake Flask Method ..	67
5.2.6	Fermentation .....	67
5.2.7	Calculations: .....	68
5.2.7.1	Extent of liquefaction:.....	68
5.2.7.2	Glucan conversion:.....	68
5.2.7.3	Glucose yield: .....	68

	5.2.7.4	Xylan conversion: .....	68
	5.2.7.5	Xylose yield: .....	69
	5.2.7.6	Ethanol yield: .....	69
5.3	Results .....		69
	5.3.1	Feedstocks and pretreatment.....	69
	5.3.2	Enzymatic hydrolysis buffer pH and concentration influences sugar release and fermentability of the hydrolysates .....	70
	5.3.3	Sugar yields decline with increasing solids loading due to low water availability for liquefaction. ....	73
	5.3.4	Enzymatic hydrolysis in roller bottles led to greater liquefaction and higher sugar yields compared to shake flasks .....	76
	5.3.5	The Field-to-Fuel Platform successfully replicates fermentation results observed in larger scale experiments .....	80
5.4	Discussion .....		83
5.5	Conclusion.....		86
5.6	Funding.....		86
5.7	Acknowledgments .....		86
6	Conclusion .....		87
	6.1	Microfluidic imaging reactor (Chapter 3) .....	87
	6.2	Wheat straw (Chapter 4).....	87
	6.3	Roller bottle enzymatic hydrolysis (Chapter 5) .....	88
7	Future work .....		89
	7.1	Microfluidic imaging reactor (Chapter 3) .....	89
	7.2	Wheat straw (Chapter 4).....	89
	7.3	Roller bottle enzymatic hydrolysis (Chapter 5) .....	90
8	Reference List .....		91
9	Supplementary information .....		113
	9.1	Imaging reactor.....	113
	9.2	Roller bottle.....	118
A	Copyrights documentation.....		125
	A.1	A high solids field-to-fuel research pipeline to identify interactions between feedstocks and biofuel production. Biotechnology for biofuels .....	125

## List of Figures

Figure 2.1. Lignocellulosic biomass composition. Created with BioRender.com.....	5
Figure 2.2. Illustration of cellulose microfibrils. Created with BioRender.com. ....	6
Figure 2.3. Hemicellulose monomers. ....	7
Figure 2.4. A) Monolignols and B) generic lignin subunits. ....	8
Figure 2.5. Cell wall morphology indicating the different cell wall layers, cell corners, and middle lamella. Created with BioRender.com. ....	9
Figure 2.6. A brightfield micrograph of corn stem (grass) cross section showing the important cell types. ....	11
Figure 2.7. Biochemical conversion of lignocellulosic biomass. Reproduced based on [60]. ....	12
Figure 2.8. Enzymatic hydrolysis. Created with BioRender.com. Reproduced based on [84]. ....	15
Figure 2.9. A) A shake flask (batch mode) showing accumulation of solids along the periphery, which leads to improper mixing, B) Horizontal mixing using a laboratory scale roller aide in overcoming solids accumulation, C) Low water availability in 18% solids w/w dry biomass enzymatic hydrolysis, D) No water available in 28% solids w/w dry biomass enzymatic hydrolysis. ....	18
Figure 2.10. Commonly used imaging techniques to elucidate cell wall properties. Created with BioRender.com. ....	20
Figure 2.11. Schematic representation of A) SEM and B) TEM. Reproduced based on [145] and [146] using BioRender.com. ....	21
Figure 2.12. Schematic representation of A) atomic force microscopy (AFM) and B) confocal Raman microscopy. Created with BioRender.com. Reproduced based on [98]. ....	22
Figure 2.13. Schematic representation of A) Epifluorescence microscope and B) Confocal laser scanning microscope. Created with BioRender.com. Reproduced based on [169]. ....	24
Figure 2.14. CLSM image of a corn stem section showing lignin autofluorescence. The excitation wavelength was 405 nm with a DAPI emission bandpass filter (480- 550 nm). ....	25
Figure 2.15. Photolithography process for SU-8 photoresist on a Si/SiO <sub>2</sub> substrate. Created with BioRender.com. ....	28
Figure 3.1. A) Microfluidic imaging reactor containing an untreated corn stem sample. Vascular bundles in the B) rind and D) pith region of a 60 μm thick untreated corn stem show strong lignin autofluorescence, with greatest intensity near the cell corners throughout the cross section (white arrows). The initial fluorescence intensities increased gradually for parenchyma (Pa), sclerenchyma (Sc),	



metaxylem (Me), and protoxylem (Pr) cell walls in the C) rind and E) pith regions. The excitation wavelength was 405 nm with a DAPI emission bandpass filter (480-550 nm).....36

Figure 3.2. Vascular bundles in the rind (A-D) and pith (F-I) regions exhibited a gradual loss of fluorescence intensity after dilute acid pretreatment for 15 min (B, G), 30 min (C, H), and 45 min (D, I). The different cell types, including parenchyma (Pa), sclerenchyma (Sc), metaxylem (Me), and protoxylem (Pr) were selected as regions of interest (ROI) to quantify changes in lignin autofluorescence. Parenchyma cell walls have lower lignin autofluorescence fluorescence than the other cell types at all pretreatment stages (white arrows). (E, J) No significant structural changes occurred for all the cell types in both the rind and the pith regions after 45 min (brightfield images). Dilute acid pretreatment was carried out on a 60 µm thick corn stem section using 1 M sulfuric acid at 100 °C. The excitation wavelength was 405 nm with a DAPI emission bandpass filter (480-550 nm). .....38

Figure 3.3. Different cell types in the rind (A-D) and pith (E-H) showed variation in initial fluorescence followed by rapid loss of fluorescence signals during the first 15 min of dilute acid pretreatment. Dilute acid pretreatment was carried out on a 60 µm thick corn stem section using 1 M sulfuric acid at 100 °C. The excitation wavelength was 405 nm with a DAPI emission bandpass filter (480-550 nm).....39

Figure 3.4. The rind (A-D) and pith (E-H) regions showed a gradual loss of fluorescence signals after 15 min (B, F), 30 min (C, G) and 45 min (D, H) of dilute alkali pretreatment with 62.5 mM sodium hydroxide at 100°C. The different cell types, including parenchyma (Pa), sclerenchyma (Sc), metaxylem (Me), and protoxylem (Pr) were selected as regions of interest (ROI) to quantify changes in lignin autofluorescence. The excitation wavelength was 405 nm with a DAPI emission bandpass filter (480-550 nm). Cell wall thickness (I, J) increased for all cell types in both the rind and the pith region following alkaline pretreatment. Values for all subfigures are reported as mean ± S.D, n=3. ....40

Figure 3.5. (A-D) CLSM images of a vascular bundle of corn stem in the rind region with immunolabeling for arabinoxylan using LM11 monoclonal antibody and Alexa Fluor 568 secondary antibody for untreated, 15 min, 30 min, and 45 min dilute acid pretreated samples. (E-F) CLSM images of a vascular bundle in the pith region with immunolabeling for arabinoxylan using LM11 monoclonal antibody and Alexa Fluor 568 secondary antibody for untreated, 15 min, 30 min, and 45 min dilute acid pretreated samples. The samples were excited using a 559 nm laser and with emission at 580-620 nm. (I) Acetyl bromide soluble lignin (ABSL) decreased for the dilute alkali pretreated sample due to lignin solubilization (J&K) Arabinose and xylose composition decreased for the dilute acid pretreated sample due to hemicellulose hydrolysis (L) Cumulative xylose release during dilute acid pretreatment was higher than during dilute alkali pretreatment. Values for all subfigures are reported as mean ± S.D, n=2. ....42

- Figure 3.6. Brightfield images of corn stem samples during enzymatic hydrolysis after dilute acid (A-M) and alkali (N-Z) pretreatment. The parenchyma (Pa) cell walls hydrolyzed more readily than the cell walls in the vascular bundle (Va). After 48 hr (G, T) it became impossible to distinguish cells derived from the pith and rind. Glucose (AA) and xylose (AB) conversion during enzymatic hydrolysis of acid and alkali pretreated samples. Values for all subfigures are reported as mean  $\pm$  S.D, n=2. The error bars are smaller than the symbols for most of the data points. The conversions were calculated on an untreated, dry biomass basis. ....44
- Figure 4.1. A) Images of McNeal (hollow), Vida (semisolid), and Choteau (solid) samples. B, C and D) CLSM images of untreated McNeal, Vida, and Choteau samples showing lignin autofluorescence. The excitation wavelength was 405 nm with a DAPI emission bandpass filter (480-550 nm).....51
- Figure 4.2. A gradual loss of lignin autofluorescence signals was observed for McNeal (A-D), Vida (E-H), and Choteau (I-L) samples after 15 min (B, F, J), 30 min (C, G, K), and 45 min (D, H, L). Dilute acid pretreatment was carried out on 60  $\mu$ m thick McNeal, Vida, and Choteau sections using 1 M sulfuric acid at 100  $^{\circ}$ C. The excitation wavelength was 405 nm with a DAPI emission bandpass filter (480-550 nm). ....52
- Figure 4.3. Different cell types in the McNeal (A-D), Vida (E-H) and Choteau (I-L) samples showed variations in their lignin autofluorescence intensities during dilute acid pretreatment with 1M sulfuric acid at 100  $^{\circ}$ C. Values for all subfigures are reported as mean  $\pm$  S.D., n=3.....53
- Figure 4.4. A gradual loss of lignin autofluorescence signals was observed for McNeal (A-D), Vida (E-H), and Choteau (I-L) samples after 15 min (B, F, J), 30 min (C, G, K), and 45 min (D, H, L). Dilute alkali pretreatment was carried out on 60  $\mu$ m thick McNeal, Vida, and Choteau sections using 62.5 mM sodium hydroxide at 100  $^{\circ}$ C. The excitation wavelength was 405 nm with a DAPI emission bandpass filter (480-550 nm).....54
- Figure 4.5. Different cell types in the McNeal (A-D), Vida (E-H) and Choteau (I-L) samples showed variations in their lignin autofluorescence intensities during dilute alkali pretreatment with 62.5 mM sulfuric acid at 100  $^{\circ}$ C. Values for all subfigures are reported as mean  $\pm$  S.D., n=3. Three regions of interest were selected for each cell type to obtain the fluorescence intensity profile. ....55
- Figure 4.6. The cell wall thickness increased more following dilute alkali pretreatment than dilute acid pretreatment. Dilute acid pretreatment was carried out on a 60  $\mu$ m thick wheat straw samples using 1 M sulfuric acid and dilute alkali pretreatment with 62.5 mM sodium hydroxide at 100 $^{\circ}$ C. Values for all subfigures are reported as mean  $\pm$  S.D., n=3. Three regions of interest were selected for each cell type to obtain the cell wall thickness. ....56
- Figure 4.7. A) Acetyl bromide soluble lignin (ABSL) decreased for the dilute alkali pretreated McNeal, Vida, and Choteau samples due to lignin solubilization. B) Arabinose and C) xylose composition decreased for the dilute acid pretreated

McNeal, Vida, and Choteau samples due to hemicellulose hydrolysis. Values are reported as percentage of acid insoluble residue (AIR). D) Cumulative xylose release during dilute acid pretreatment was higher for the Choteau sample than the McNeal and Vida samples. There was <1% xylose release than during dilute alkali pretreatment for all the three samples. Values for all subfigures are reported as mean $\pm$ S.D, n=2 composition analysis replicates (A, B, C) and pretreatment supernatant (D) replicates. ....	57
Figure 4.8. Glucose and xylose conversion for Choteau, Vida and McNeal samples after dilute acid and dilute alkali pretreatment. Values for all subfigures are reported as mean $\pm$ S.D., n=2 hydrolysate replicates. ....	58
Figure 4.9. Brightfield images of dilute acid-pretreated McNeal (A-H), Vida (I-P), and Choteau (Q-X) samples during enzymatic hydrolysis. ....	59
Figure 4.10. Brightfield images of dilute alkali pretreated McNeal (A-H), Vida (I-P), and Choteau (Q-X) samples during enzymatic hydrolysis. ....	60
Figure 5.1. A) Increasing buffer pH and concentration decreased hydrolysate final pH. B) Increasing buffer pH (3.0 to 4.5) and concentration (0.1 to 0.2 M) increased glucose conversion and glucose concentration for AFEX pretreated CS at 6% glucan loading. C) Increasing buffer pH (3.0 to 4.5) and concentration (0.1 to 0.2 M) increased xylose conversion and xylose concentration for AFEX pretreated CS at 6% glucan loading for buffer pH 3.0 and 4.5. Values for all subfigures are reported as the mean $\pm$ SD, n=2. ....	72
Figure 5.2. A) Ethanol concentration was more affected by buffer pH (3.0 > 4.5) than concentration for both <i>S. cerevisiae</i> and <i>Z. mobilis</i> in 6% glucan loading hydrolysate. B) Ethanol yield was not affected significantly by hydrolysate buffer pH. For both <i>S. cerevisiae</i> and <i>Z. mobilis</i> , while the yields were higher at a lower buffer concentration for both cases. All hydrolysates were made from AFEX pretreated CS at 6% glucan loading. All fermentations were conducted at a pH of $5.8 \pm 0.1$ . Values for all subfigures are reported as the mean $\pm$ SD, n=2. ....	73
Figure 5.3. A) 6% glucan loading produced higher volume of hydrolysate than 9% glucan loading for all centrifugation times. Also, the volume of hydrolysate was not affected by the centrifugation times. B) Although the glucose concentrations were similar for both solids loading conditions, the glucose conversion was higher for 6% glucan loading than 9% glucan loading for all buffer concentrations. C) Xylose conversion was higher for 6% glucan loading than 9% glucan loading for all buffer concentrations. Values for all subfigures are reported as the mean $\pm$ SD, n=2. ....	75
Figure 5.4. Roller bottle enzymatic hydrolysis achieves better liquefaction than the shake flask method, with equivalent final hydrolysate volumes despite different starting hydrolysis volumes. A) Final hydrolysate volumes are similar for roller bottle and shake flask hydrolysis. B) Extent of liquefaction is greater for roller bottle enzymatic hydrolysis. CS = corn stover, SOR = sorghum, MSC = miscanthus, NP = native prairie, SG = switchgrass. Numbers refer to the biomass harvest year.	

Values for all subfigures are reported as the mean $\pm$ SD, n=2. Values for all subfigures are reported as the mean $\pm$ SD, n=2. ....	77
Figure 5.5. A) Glucose yield was higher for the roller bottle hydrolysates than the shake flask hydrolysates for all the feedstocks. B) Xylose yield was higher for the roller bottle hydrolysates than the shake flask hydrolysates. C) Hydrolysate glucose concentration was similar for both roller bottle and shake flask samples. D) Hydrolysate xylose concentration was similar for both roller bottle and shake flask samples. CS = corn stover, SOR = sorghum, MSC = miscanthus, NP = native prairie, SG = switchgrass. Numbers refer to the biomass harvest year. Values for all subfigures are reported as the mean $\pm$ SD, n=2. Values for all subfigures are reported as the mean $\pm$ SD, n=2. ....	78
Figure 5.6. CO <sub>2</sub> production by A) <i>S. cerevisiae</i> Y945 and B) <i>Z. mobilis</i> 2032 show some feedstock-specific differences during fermentation of hydrolysates generated in roller bottles or shake flasks. For each feedstock, columns represent separate paired replicates, where the two fermentations (shake flask and roller bottle system) were run simultaneously. (Plots in the same column across feedstocks were not necessarily run in the same batch of fermentations.).....	79
Figure 5.7. Max CO <sub>2</sub> volume is correlated with the final volume of ethanol produced during fermentation for both <i>S. cerevisiae</i> Y945 and <i>Z. mobilis</i> ZM2032. Samples are 6% glucan loading hydrolysates produced using the roller bottle and shake flasks from all five grass feedstocks that had been pretreated in the 5-gallon reactor (2008 corn stover, 2010 and 2012 switchgrass, and 2014 miscanthus, native prairie, and sorghum). ....	80
Figure 5.8. Clustered correlation matrix for <i>S. cerevisiae</i> Y945 fermentation data (black labels) and hydrolysate composition (red text labels). The plot was generated using the corplot package in R with hclust (hierarchical clustering order). The size and color correspond to the direction and magnitude of the correlation. Correlations that were insignificant ( $p > 0.05$ ) were not plotted. †The process ethanol yield is the ratio of sugars initially present in the hydrolysate (glucose and xylose) to ethanol produced assuming 0.51 g ethanol/g sugars as the theoretical maximum. ‡The metabolic yield is the ratio of sugars (glucose and xylose) consumed during fermentation to ethanol produced assuming 0.51 g ethanol/g sugars as the theoretical maximum. ....	81
Figure 5.9. Max CO <sub>2</sub> volume is correlated with the final volume of ethanol produced during fermentation for both <i>S. cerevisiae</i> Y945 and <i>Z. mobilis</i> ZM2032. Samples are 6% glucan loading hydrolysates produced using the roller bottle and shake flasks from all five grass feedstocks that had been pretreated in the 5-gallon reactor (2008 corn stover, 2010 and 2012 switchgrass, and 2014 miscanthus, native prairie, and sorghum). ....	82
Figure 5.10. <i>Saccharomyces cerevisiae</i> grown in drought year (2012) switchgrass hydrolysates showed significantly reduced or delayed CO <sub>2</sub> production compared to when it was grown in 2010 switchgrass hydrolysates from a year with normal precipitation. Each graph represents a separate batch of hydrolysate and each	

column represents paired replicates that were fermented in the same respirometer experiment.....	83
Figure 5.11. Process flowchart for the field-to-fuel platform including small scale AFEX pretreatment, roller bottle enzymatic hydrolysis and respirometer fermentation using <i>S. cerevisiae</i> and <i>Z. mobilis</i> . Created with BioRender.com. ....	85
Figure 9.1. Vascular bundles in the rind (A-D) and pith (E-H) regions did not show any significant structural changes after dilute acid pretreatment after 15 min (B, F), 30 min (C, G), and 45 min (D, H). Dilute acid pretreatment was performed on a 60 $\mu\text{m}$ thick corn stem section using 1 M sulfuric acid at 100 $^{\circ}\text{C}$ . ....	115
Figure 9.2. Different cell types in the rind (A-D) and pith (E-H) showed variation in initial fluorescence followed by rapid loss of fluorescence signals during the first 15 min of dilute alkali pretreatment using 62.5 mM NaOH. ....	116
Figure 9.3. (A-D) CLSM images of a vascular bundle of corn stem in the rind region with immunolabeling for arabinoxylan using LM11 monoclonal antibody and Alexa Fluor 568 secondary antibody for untreated, 15 min, 30 min, and 45 min dilute acid pretreated samples. (E-F) CLSM images of a vascular bundle in the pith region with immunolabeling for arabinoxylan using LM11 monoclonal antibody and Alexa Fluor 568 secondary antibody for untreated, 15 min, 30 min, and 45 min dilute acid pretreated samples. The samples were excited using a 559 nm laser and with emission at 580-620 nm. The different cell types, including parenchyma (Pa), sclerenchyma (Sc), metaxylem (Me), and protoxylem (Pr) were selected as regions of interest (ROI) to quantify changes in the LM11 binding across the various samples. ....	116
Figure 9.4. Different cell types in the rind (A-D) and pith (E-H) did not show much variation in the LM11 fluorescence signals in the untreated samples, while there was a gradual loss of LM11 fluorescence signals for all cell types in the 15 min, 30 min, and 45 min dilute acid pretreated samples.....	117
Figure 9.5. Roller Bottle and shake flask hydrolysate composition. Bars represent the average with error bars as $\pm$ standard deviation.....	123
Figure 9.6. Clustered correlation matrix for <i>Z. mobilis</i> 2032 fermentation data and hydrolysate composition (red text labels). The plot was generated using the corrplot package in R with hclust (hierarchical clustering order). The size and color correspond to the direction and magnitude of the correlation. Correlations that were insignificant ( $p < 0.05$ ) were not plotted. ....	124

## List of Tables

Table 9.1-1. Composition of untreated, dry biomass and the residual biomass after dilute acid and dilute alkali pretreatment. Values are reported as mean $\pm$ S.D, n=3. ....	113
Table 9.1-3. Composition of pretreatment supernatant at different time points of dilute acid and dilute alkali pretreatment. Values are reported as mean $\pm$ S.D, n=2. ....	113
Table 9.1-4. Hydrolysate concentration was analyzed using HPLC at different time points during the enzymatic hydrolysis of the pretreated samples. Values are reported as mean $\pm$ S.D. n=2. ....	114
Table 9.2-1. Untreated feedstock composition for different types of cellulosic biomass. ....	118
Table 9.2-2. Summary of <i>Saccharomyces cerevisiae</i> Y945 fermentation results. Values are reported as the mean $\pm$ s.d. (n=3 or 4). ....	119
Table 9.2-3. Summary of <i>Zymomonas mobilis</i> 2032 fermentation results. Values are reported as the mean $\pm$ s.d. (n=3 or 4). ....	121

## Author Contribution Statement

The idea of conducting microscopy of thin whole sections of lignocellulosic biomass during pretreatment and enzymatic hydrolysis was formulated by my advisor, Dr. Rebecca G. Ong. I worked on my specific research goals towards this concept. The material presented in the Abstract and in Chapters 1 and 3 have been submitted for publication in a manuscript entitled "*Design and construction of a microfluidic reactor for time-lapsed imaging of pretreatment and enzymatic hydrolysis of lignocellulosic biomass*", by Meenaa Chandrasekar, Jeana Collins, Sanaz Habibi, and Rebecca G. Ong.

The importance of stem solidness for herbaceous bioenergy feedstocks was identified by my advisor, Dr. Rebecca G. Ong. The process of testing three cultivars of the same species (wheat straw) to understand the impact of stem solidness on enzymatic saccharification was formulated by my advisor, Dr. Rebecca G. Ong. I worked on carrying out microscopic imaging during the deconstruction of the hollow, semisolid and solid wheat straw samples. The material presented in the Abstract and in Chapters 1 and 4 have been included in a manuscript entitled "*Will pith solidness in wheat straw increase sugar yields during enzymatic hydrolysis?*", by Meenaa Chandrasekar, Eric Olson, and Rebecca G. Ong.

The idea of utilizing laboratory scale roller to carry out high throughput enzymatic hydrolysis at high solids loading was formulated by my advisor, Dr. Rebecca G. Ong. I worked on my specific research goal of optimizing the process parameters for the high solids enzymatic hydrolysis method. Leela Joshi, Karleigh Krieg and I performed the enzymatic hydrolysis experiments. Derek Debrauske performed the respirometer fermentation experiments. Sarvada Chipkar provided the method for the shake flask experiments. The material presented in the Abstract and in Chapters 1 and 5 have been published in a manuscript entitled "*A high solids field-to-fuel research pipeline to identify interactions between feedstocks and biofuel production. Biotechnology for biofuels*", by Meenaa Chandrasekar, Leela Joshi, Karleigh Krieg, Sarvada Chipkar, Emily Burke, Derek J. Debrauske, Kurt D. Thelen, Trey K. Sato, and Rebecca G. Ong. This work is reproduced with permission from Springer Nature. The publishing agreement can be found in Appendix A.1.

## Acknowledgments

I would like to express my deepest appreciation to my advisor, Dr. Rebecca Garlock Ong, for allowing me to pursue research under her invaluable guidance. Her expertise and mentorship have been instrumental in shaping my academic journey. Her unwavering support and positive mindset have been a constant source of inspiration, especially during the most daunting moments. I am profoundly grateful for everything she has done.

I am also thankful to Dr. Trey Sato for his guidance in publishing my first research article. His project vision has significantly influenced my approach to research and writing, leaving a lasting positive impact.

I am grateful to the Ong Lab members, especially Ms. Leela Joshi, Ms. Karleigh Krieg, Ms. Sulihat Aloba, Dr. Sarvada Chipkar, and Ms. Andrea Senyk for their timely help with my experiments.

I express my gratitude to Dr. David R. Shonnard, Dr. Michael R. Gretz, and Dr. Smitha Rao Hatti for their generous contribution of knowledge and expertise towards completing my dissertation. Their guidance has been invaluable in this endeavor, and I sincerely appreciate their support.

I sincerely thank Dr. John Sandell for his valuable insights in various aspects of my teaching assistantship and research. I admire his passion for engineering and teaching.

I would like to extend my heartfelt thanks to Dr. Raisa Carmen Andeme Ela, a remarkable friend and an exceptional source of motivation.

I would like to thank the Department of Chemical Engineering and Michigan Technological University for their generous provision of essential resources for my research. Additionally, I am immensely grateful for the nurturing and supportive community at Michigan Tech, which has played a pivotal role in fostering my academic and personal development.

I would like to thank all my family members and friends for their incredible emotional support. Their belief in me has kept my spirits and motivation high during this process.

Above all, I bow down to the Lord Almighty, whose grace and strength were experienced from the very inception to the completion of this work.



## Abstract

Renewable fuels from lignocellulosic biomass are an appealing option because they can seamlessly integrate into the existing fuel distribution infrastructure. Lignocellulosic biomass constitutes nonedible plant material obtained from plant cell walls. The natural recalcitrance of lignocellulosic biomass poses a challenge in accessing the cell wall carbohydrates during biochemical conversion. Despite various approaches, enzymatic hydrolysis of lignocellulosic biomass remains economically impractical due to incomplete knowledge about biomass recalcitrance and the influence of environmental factors on biomass quality. Biomass recalcitrance is linked to lignin and hemicellulose in the plant cell wall. Their distribution varies within the cell wall and among tissue types within the same biomass.

The first goal of this dissertation was to construct a microfluidic imaging reactor to better understand the tissue-specific deconstruction of plant materials. Confocal laser scanning microscopy was conducted on thin sections (60  $\mu\text{m}$  thickness) of corn stems at different time points during dilute acid and dilute alkali pretreatment. The digestibility of the acid and alkali-pretreated biomass sections during enzymatic hydrolysis were evaluated using brightfield imaging. The ability to immunolabel plant materials within the reactor was demonstrated using LM11, an arabinoxylan-specific antibody. Corn stem parenchyma cells were more susceptible to deconstruction than vascular bundles in both pretreatment and enzymatic hydrolysis. After 48 hours of enzymatic hydrolysis, only the protoxylem remained undegraded. The alkali-pretreated sample was more readily hydrolyzed than the acid-pretreated sample during enzymatic hydrolysis, possibly due to the maximum operating temperature of the reactor.

The second goal was to investigate how increasing stem solidness impacts enzymatic digestibility in wheat straw using the microfluidic imaging reactor. This was based on the rationale that the pith parenchyma cells are more digestible than the other vascular cell types. Stem sections from three greenhouse-grown wheat cultivars with different stem solidness (hollow, semisolid, and solid) were pretreated with 1 M sulfuric acid and 62.5 mM sodium hydroxide at 100 °C. During subsequent enzymatic hydrolysis, the solid stemmed samples showed considerably greater glucose and xylose conversions than the hollow and semisolid cultivars, which based on the imaging was largely due to the greater digestibility of the pith parenchyma cells.

The third goal was to develop a high-throughput, moderate-scale enzymatic hydrolysis method at high-solids loading to study the impact of drought and extreme weather conditions on biomass deconstruction. At the laboratory scale, high solids loading results in improper mixing and low saccharification due to low water availability. This was overcome using horizontal mixing on a laboratory scale roller to improve enzyme accessibility and obtain higher sugar yields. The saccharification for the roller bottle method was about 25-50% higher than the traditional shake flask method. This was evaluated for a variety of AFEX-pretreated feedstocks, including corn stover, sorghum, miscanthus, native prairie, and switchgrass.

# 1 INTRODUCTION

## 1.1 Motivation

Global energy demand has increased due to the rapidly growing world population, which largely relies on fossil fuels. Fossil fuels are nonrenewable, and their combustion causes massive emissions of greenhouse gases (GHG) [1]. A significant share of these emissions are from the transportation sector (approximately 23%) [2]. Although electrification of transportation has become exceedingly popular due to the zero tailpipe emissions, the need for charging infrastructure, limited capacity of vehicle batteries, and extended charging times are some challenges that need to be addressed. Fuels produced from renewable sources are particularly appealing as they can be used with the existing fuel distribution infrastructure [3]. Biofuels are conventionally produced from edible sources like corn grain and sugarcane (first-generation biofuels), however, this has raised concerns about food security and price inflation [4]. In this context, lignocellulosic feedstocks have emerged as a viable option for producing liquid transportation fuels and chemicals [5]. Lignocellulosic biomass is the nonedible plant material derived from the plant cell wall. The U.S. alone can potentially produce about one billion tons of lignocellulosic biomass annually and sustainably [6].

Enzymatic hydrolysis of plant cell wall carbohydrates for production of monomeric sugars has become increasingly popular in biofuel production due to the mild process conditions, low environmental impacts, and the possibility of obtaining other valuable chemicals from the residual biomass [7]. However, the inherent recalcitrance of natural lignocellulosic biomass hinders the accessibility of the cell wall carbohydrates during biochemical conversion. Current strategies to overcome biomass recalcitrance are (i) conducting a pretreatment prior to enzymatic hydrolysis, (ii) perturbing the biosynthesis of cell wall components that cause recalcitrance, and (iii) engineering enzymes with improved catalytic efficiency [8]. A complete understanding of biomass recalcitrance and the effects of environmental stressors on biomass quality could potentially lead to solutions that make the biofuel production process economically viable and environmentally friendly [9, 10].

Biomass recalcitrance is often attributed to the presence of lignin and hemicellulose in the plant cell wall [10]. The distribution of lignin and hemicellulose varies within the cell wall and between the tissue types within the same biomass type [11]. Thick-walled cell types like sclerenchyma, vascular bundles, and epidermis have higher lignin and hemicellulose content when compared to the thin-walled parenchyma cells [12, 13]. This spatial variability in recalcitrance influences the biomass deconstruction [14, 15]. Several studies have tried interpreting tissue-level biomass recalcitrance by characterizing fractionated tissues through composition analysis and imaging pretreated biomass [16-18]. However, the major bottlenecks in conducting microscopic studies to evaluate tissue-specific biomass recalcitrance are: (i) imaging ground biomass impedes understanding tissue-specific changes during biomass deconstruction, (ii) handling pretreated biomass is extremely difficult, which poses several challenges in obtaining thin sections for imaging without losing the original lignocellulosic structure in the sample and (iii) the exact same

sample cannot be imaged at different stages in the process when the pretreatment is carried out in bulk.

Environmental factors like drought and weather extremes affect biomass quality due to inhibitors that form within the cell wall due to weather stress or during the pretreatment [19, 20]. Abiotic stressors like drought and extreme temperatures affect feedstock quality and yield. Decreased biomass yield due to drought could interrupt feedstock supply for biofuel production. Several studies have focused on developing crop drought tolerance or identifying ideal locations to cultivate drought-tolerant crops to ensure uninterrupted feedstock supply [21, 22]. In addition to feedstock supply, weather extremes during plant growth can adversely affect biomass deconstruction and lower biofuel yields. Very few studies have evaluated the field-to-fuel effect of weather extremes on biomass deconstruction and biofuel yields under industrially relevant conditions [20, 23, 24]. In larger bioreactors in the industry, high solids loading is favored because a larger biomass loading results in higher sugar concentrations after enzymatic hydrolysis, resulting in higher bioethanol concentrations following fermentation [83]. Hence, at the laboratory scale, a platform for high throughput, moderate-scale biomass deconstruction at high-solids loading is essential to evaluate the effect of environmental factors on biomass deconstruction. The main challenges in conducting such studies are (i) the large number of feedstock samples (sometimes in limited quantity) grown under multiple conditions that need to be evaluated to determine the effect of environmental factors, (ii) fermentation experiments have a scale limit (minimum hydrolysate volume requirement), which means the pretreatment and enzymatic hydrolysis scales should be designed for this requirement.

## 1.2 Research Objectives

The overarching goal of this dissertation was to develop characterization methods to overcome a few of the most compelling bottlenecks in microscopic and laboratory-scale high-solids enzymatic hydrolysis of lignocellulosic biomass. In this work, first, a microfluidic imaging reactor was constructed to conduct pretreatment and enzymatic hydrolysis on thin biomass sections while carrying out confocal laser scanning microscopy at different time points. Second, the microfluidic imaging reactor was utilized to evaluate the biomass deconstruction of three wheat cultivars with hollow, semisolid, and solid stems to understand the benefit of stem solidness from the biofuel production perspective. Third, a horizontal roller bottle high-solids enzymatic hydrolysis method was developed using gravitational tumbling to overcome the mass transfer limitations in conventional shake flasks.

The specific objectives are as follows:

### **1.2.1 Objective 1: Design and construct a microfluidic reactor for time-lapsed imaging of pretreatment and enzymatic hydrolysis of lignocellulosic biomass**

Confocal laser scanning microscopy (CLSM) combined with immunohistochemistry can provide a deeper understanding of the influence of tissue and cell types on biomass deconstruction. This objective aimed to construct a microfluidic imaging reactor to better understand tissue-specific deconstruction of plant materials. CLSM was conducted on thin sections (60  $\mu\text{m}$  thickness) of corn stems and the changes in lignin autofluorescence at different time points during dilute acid and dilute alkali pretreatment were recorded for different cell types. The digestibility of the acid and alkali-pretreated biomass sections during enzymatic hydrolysis were evaluated using brightfield imaging. The ability to immunolabel plant materials within the reactor was demonstrated using LM11, an arabinoxylan-specific antibody. The microfluidic imaging reactor was successfully used to visualize the progression of biomass pretreatment and enzymatic hydrolysis and the differential effectiveness based on tissue types. In particular, corn stem parenchyma cells showed more susceptibility to deconstruction than the vascular bundles during both pretreatment and enzymatic hydrolysis, and only the protoxylem remained undegraded following 48 hours of enzymatic hydrolysis. During enzymatic hydrolysis, the alkali-pretreated sample was hydrolyzed more readily than the acid-pretreated sample, however this was likely a function of the maximum operating temperature of the reactor.

*Publication:* Chandrasekar, M.; Collins, J.; Habibi, S.; Ong, R. G. Design and construction of a microfluidic reactor for time-lapsed imaging of pretreatment and enzymatic hydrolysis of lignocellulosic biomass. Submitted for publication to "Bioresource Technology" on 13<sup>th</sup> June, 2023.

### **1.2.2 Objective 2: Utilize the imaging reactor to compare the deconstruction of hollow, semi-solid, and solid pith wheat straw cultivars**

Stem solidness is a variable trait in grasses, which can either be hollow or solid at maturity. Greater stem solidness is expected to be a desirable trait for bioenergy production due to the larger amounts of thin-walled, less recalcitrant, and readily digestible parenchyma cells. Most grass species are either hollow or solid and so cannot be used to investigate the impact of the trait on bioenergy production, however wheat shows variability in the stem solidness trait and is a useful feedstock to investigate the effect of grass stem solidness on enzymatic digestibility and potential for biofuel production. For this project, stem sections from three greenhouse-grown wheat cultivars with hollow (McNeal), semisolid (Vida), and solid (Choteau) wheat stems were subjected to pretreatment in a custom imaging reactor using either 1 M sulfuric acid and 62.5 mM sodium hydroxide, respectively, at 100 °C. Subsequent enzymatic hydrolysis of these pretreated sections were carried out for 72 hours. Imaging was carried out over the course of pretreatment and enzymatic hydrolysis using a confocal laser scanning microscope. Lignin autofluorescence changes during pretreatment indicated a high susceptibility to

pretreatment of the pith parenchyma cell walls in the Choteau (solid) sample. The enzymatic hydrolysis indicated that the Choteau (solid) samples had higher glucose and xylose conversions compared to the hollow-stemmed cultivars. Brightfield images during enzymatic hydrolysis also show that the pith parenchyma cells of Choteau (solid) degraded completely by 48 hours, while the rind region of Choteau (solid) and the other two hollow-stemmed cultivars (McNeal and Vida) remained largely intact, even after 72 hours. These findings highlight the potential to engineer the stem solidness trait into hollow-stemmed grass-based feedstocks like switchgrass as a means to increase digestibility.

*Publication:* Chandrasekar, M.; Olson E.; Ong, R. G. Will pith solidness in wheat straw increase sugar yields during enzymatic hydrolysis? Under preparation.

### **1.2.3 Objective 3: Develop a roller bottle method using gravitational mixing for high solids loading enzymatic hydrolysis**

Several studies have documented the effects of weather extremes on biomass yield and composition. However, it is important to evaluate the effect of abiotic stressors on biomass deconstruction and biofuel yields at industrially-relevant process conditions, such as high solids loading. At the laboratory scale, high solids loading leads to issues with enzyme accessibility and mixing due to low water availability. This objective aimed to develop a roller bottle enzymatic hydrolysis method using horizontal mixing to improve enzyme accessibility and obtain higher sugar yields. Process parameters, including solids loading, buffer pH, buffer concentration, and centrifugation time, were optimized for enzymatic hydrolysis of AFEX pretreated corn stover samples. Respirometer fermentation experiments on *S. cerevisiae* and *Z. mobilis* fermentation were conducted at UW-Madison and results were validated against previously published data generated using high-solids hydrolysis and fermentation in bioreactors. The saccharification for the roller bottle method was about 25-50% higher than the traditional shake flask method for a variety of AFEX-pretreated feedstocks, including corn stover, sorghum, miscanthus, native prairie, and switchgrass. During fermentation, the shake flask hydrolysates had slower and more inhibited fermentations than the roller bottle hydrolysates.

*Publication:* Chandrasekar, M., Joshi, L., Krieg, K., Chipkar, S., Burke, E., Debrauske, D. J., Thelen, K. D., Sato, T. K., & Ong, R. G. (2021). A high solids field-to-fuel research pipeline to identify interactions between feedstocks and biofuel production. *Biotechnology for biofuels*, 14(1), 179. <https://doi.org/10.1186/s13068-021-02033-6>.

## 2 BACKGROUND

### 2.1 Lignocellulosic biomass

Lignocellulosic biomass is the nonedible plant material that is present in the cell wall of plants like grasses, shrubs, and trees (**Figure 2.1**Error! Reference source not found.). It is comprised of three main biopolymers, cellulose (40-50%), hemicellulose (25-30% wt.), lignin (15-20% wt.), as well as small amounts of pectin, and trace inorganic compounds [25]. Cellulose, hemicellulose, and lignin are intricately intertwined to form a complex matrix [26]. The relative amounts and structure of these constituents varies between plant species and within each plant and depends on the growth stage.

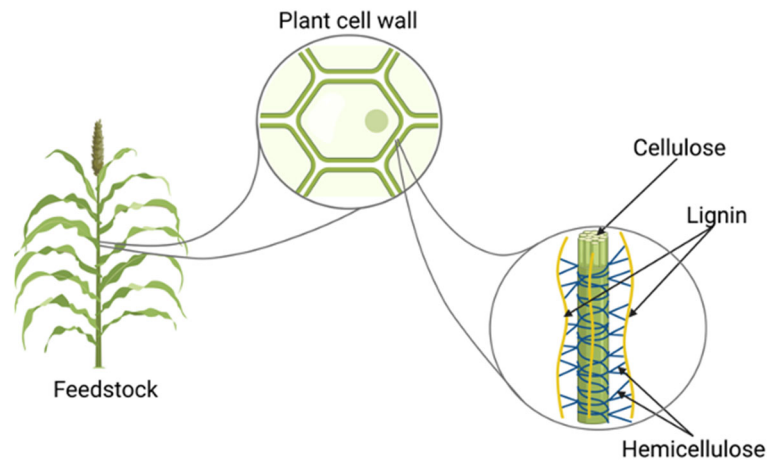


Figure 2.1. Lignocellulosic biomass composition. Created with BioRender.com.

#### 2.1.1 Cellulose

Cellulose is a polymer composed of  $\beta$ -D-glucopyranose units connected through  $\beta$ -(1 $\rightarrow$ 4)-glycosidic bonds (**Figure 2.2**). The degree of polymerization can range from 10,000 to 15,000 glucopyranose units, which varies depending on the type of feedstock [27]. Multiple cellulose chains (approximately 20-300) are linked together through hydrogen bonds or van der Waals forces to form cellulose microfibrils. The length of each microfibril is about a few microns, and diameter about 2 to 20 nm depending on the plant species and morphology [31]. The degree of polymerization also varies depending on the feedstock type. In lignocellulosic biomass, cellulose is predominantly found in a crystalline form, while a smaller fraction exists in an amorphous form [28].

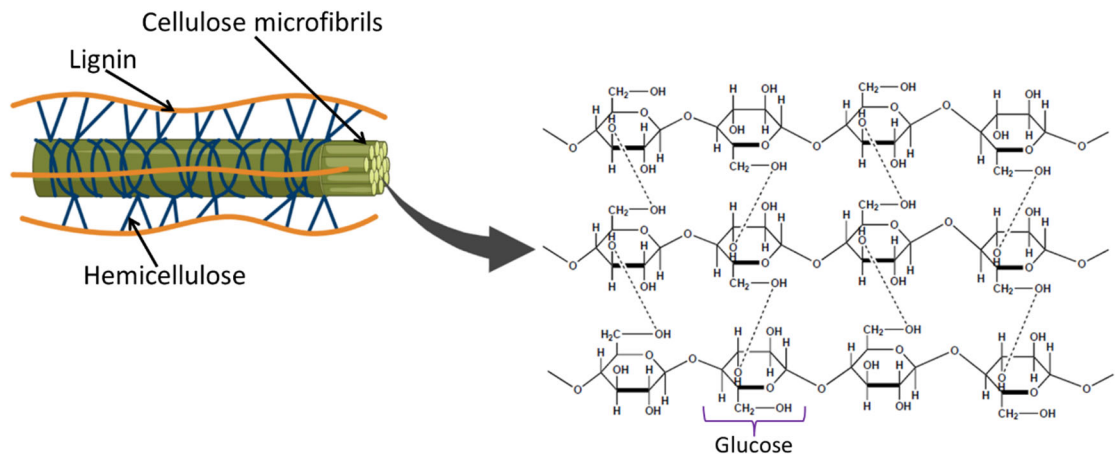
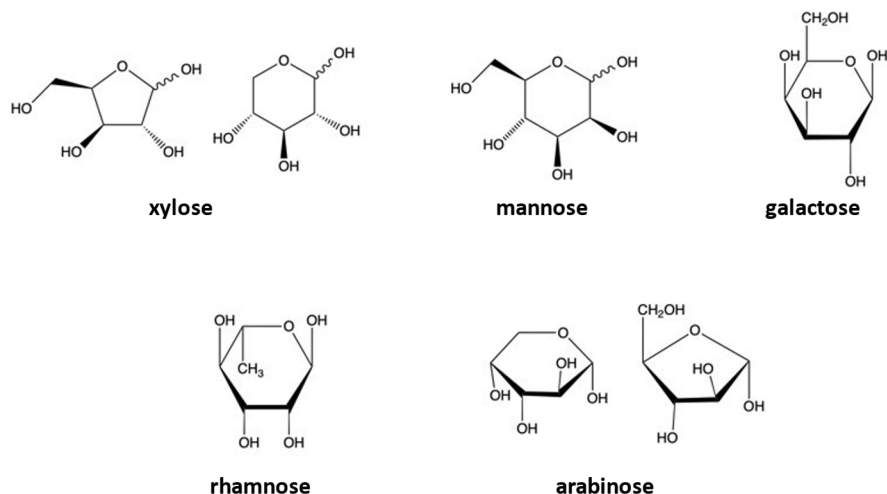


Figure 2.2. Illustration of cellulose microfibrils. Created with BioRender.com.

### 2.1.2 Hemicellulose

Hemicellulose is a heterogeneous polymer comprised of different monomeric sugars, including xylose, rhamnose, arabinose, glucose, mannose, and galactose (**Figure 2.3**). The backbone of hemicellulose can be either a homopolymer or a heteropolymer, connected through  $\beta$ -(1 $\rightarrow$ 4)- or  $\beta$ -(1 $\rightarrow$ 3)-glycosidic bonds. Hemicelluloses generally have lower molecular weights than cellulose. The composition of hemicellulose components varies between grasses, softwoods, and hardwoods [29].

Glucuronoarabinoxylan is the most abundant hemicellulose component in grasses, which has a xylan backbone and side chains of arabinose and glucuronic acid, which are often acetylated [30]. The major hemicellulose component in softwood cell walls is galactoglucomannan, followed by xylan [31]. Xylan is the main hemicellulose component in hardwoods with negligible amounts of 4-O-methylglucuronic acid and acetyl groups. The composition of the individual monomers vary based on the plant species [29].



**Figure 2.3. Hemicellulose monomers.**

### 2.1.3 Lignin

Lignin, a phenolic polymer, is constructed from three primary monolignols: *p*-coumaryl alcohol, coniferyl alcohol, and sinapyl alcohol (**Figure 2.4**). These monolignols undergo a series of radical reactions to polymerize and form the three main structural units of lignin: *p*-hydroxyphenyl (H), guaiacyl (G), and sinapyl (S) units. The hydrophobic lignin polymer predominantly comprises these structural units and is connected by C-C and  $\beta$ -O-4 ether bonds [13]. The composition of *p*-hydroxyphenyl (H), guaiacyl (G), and sinapyl (S) lignin units differs between grasses, softwoods, and hardwoods [32]. Grass lignin has a high proportion of H units and comparable amounts of G and S units. The main lignin component of softwoods is G units, with low quantities of H units. Hardwood lignin consists principally of G and S units with minor amounts of H units [13, 33].



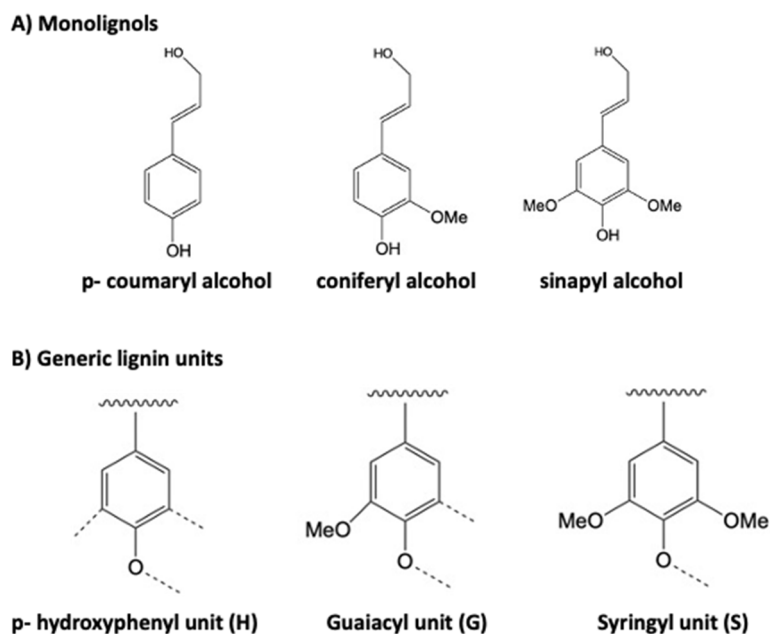


Figure 2.4. A) Monolignols and B) generic lignin subunits.

## 2.1.4 Types of lignocellulosic biomass

Lignocellulosic biomass for the production of biofuels is derived from three key sectors: agriculture, forestry, and industry [34]. The main agricultural feedstocks for biofuel production are dedicated energy crops and forestry or agricultural residues, such as bark, wood chips, sawdust, rice husks, wheat straw, corn cobs and stover, and sugarcane bagasse [35]. Among the dedicated energy crops, perennial grasses are becoming increasingly popular as a source of lignocellulosic biomass because they can grow with minimal maintenance on marginal soil. This soil type is often characterized by challenging conditions such as drought, flooding, stoniness, and low nutrient content [36, 37]. Switchgrass (*Panicum virgatum* L.), a native North American prairie grass, has been widely acknowledged since the mid-1980s for its remarkable potential as a bioenergy source. This is primarily due to its high productivity across a broad geographic range, its ability to thrive on marginal land, and the environmental benefits it offers, such as carbon sequestration and erosion control [38].

## 2.1.5 Cell wall morphology and chemical composition

When considering biofuel production from plant cell walls, it is crucial to recognize that the composition of cell walls varies substantially in terms of quality and quantity among different feedstocks [39]. Furthermore, even within the same feedstock, different cell types may exhibit variations in their cell wall composition. The cell wall of plants is typically structured into multiple layers, including the primary and secondary cell walls (Figure 2.5). The middle lamella is the region between adjacent cell walls and is rich in lignin and pectin and devoid of cellulose [40]. It holds the cells together, providing structural integrity and cohesion within the plant tissue. During the elongation phase of

cell growth, the primary cell wall is formed [27]. It is comprised of cellulose, hemicellulose, pectin, and a few structural proteins. The primary cell walls can be classified as either type I or type II. Type I is present in grasses and wood and mainly consists of cellulose, pectin, and xyloglucan as the major hemicellulose component. On the other hand, type II is found in grasses and other commelinid monocots and primarily consists of cellulose, mixed-linkage glucan, and arabinoxylan, which is the major hemicellulose component [27]. After the elongation phase ceases, the secondary cell wall is formed, which is typically thicker and consists of multiple layers. It is comprised of cellulose, xylan, lignin, structural proteins, and minor amounts of pectin [41]. The primary cell wall is present in all cell types, whereas the secondary cell wall is specifically found in specialized cell types. These specialized cells require thick cell walls to resist negative pressure caused by transpiration, provide mechanical strength to support the plant, and enable the transport of water and nutrients [42]. These cells and the cell corners possess a significant amount of lignin, with a high G:S ratio. The predominant hemicellulose components in softwoods are mannan and xylan [40]. Willow and poplar are examples of hardwood feedstocks, characterized by abundant large water-conducting vessels surrounded by narrow fibers. The lignin composition in these hardwoods comprises both G and S units. Xylose is the primary hemicellulose component in these feedstocks [43].

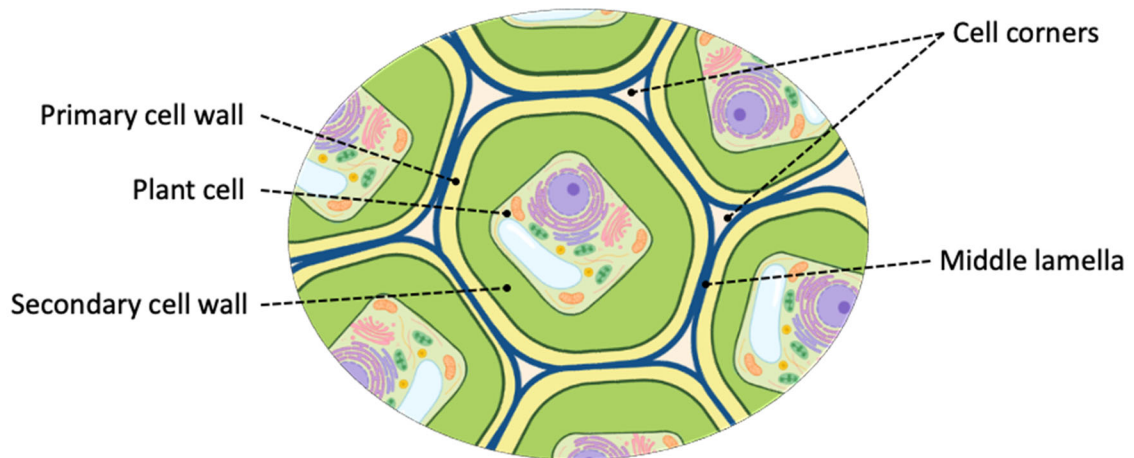


**Figure 2.5. Cell wall morphology indicating the different cell wall layers, cell corners, and middle lamella. Created with BioRender.com.**

### **2.1.6 Tissue types and cell wall composition**

Various biomass, such as softwoods, hardwoods, and grasses, exhibit distinct tissue compositions, including parenchyma and various types of sclerenchyma cells. Parenchyma cells form a large proportion of the tissue volume in plants. The abundance of parenchyma cells varies based on the plant species, environmental conditions, and the plant organ. Respiration, carbohydrate storage, photosynthesis, and nutrient assimilation are some important functions of parenchyma cells [44]. Sclerenchyma cells provide

protection against microbial attack and long-distance water transport are the main functions of sclerenchyma cells. These cells are present in fibers and water conducting tissues like xylem. The distribution of these cell types varies between different feedstocks [45]. Grasses exhibit a higher level of cell diversity compared to softwood and hardwood species. They possess an outer rind layer and an inner pith region. The rind layer is characterized by an abundance of lignin, along with a small number of parenchyma cells, a thick epidermis, several thick-walled sclerenchyma cells, and numerous vascular bundles (Figure 2.6) [14]. Vascular bundles are crucial in vertically transporting water and nutrients to different parts of the part. They consist of various tissues such as xylem, phloem, and fiber, all composed of thick-walled sclerenchyma cells [46]. On the other hand, the pith tissue in grasses is rich in cellulose and primarily composed of thin-walled parenchyma cells, with sporadically distributed thick-walled vascular bundles [47]. Regarding biofuel production, the most extensively studied cell types within plant species are parenchyma and sclerenchyma cells. Parenchyma cells are typically characterized by thin and uniform cell walls, although their chemical composition can vary depending on the specific tissue type. Parenchyma cells are considered the storage compartment for excess carbohydrates in the form of sugar or starch [48]. Sclerenchyma cells, on the other hand, can be further classified into sclereids, fibers, and tracheary elements. Sclereids and fibers possess uniformly thick secondary cell walls, while tracheary elements can form secondary cell walls in either an annular or helical pattern [48]. Xylem vessels serve as a conduit for water transport. In grasses, a vascular bundle typically has two metaxylem vessels and a protoxylem vessel. Metaxylem vessels are larger than the protoxylem [49]. Protoxylem vessels have a helical pattern of lignin deposition. Metaxylem vessels have a pitted and dense pattern of lignin deposition [50]. In woody biomass, xylem parenchyma, tracheids and vessels are the important cell types. The xylem parenchyma cells in wood are elongated and aligned in an axial orientation [51]. Unlike grasses, wood parenchyma cells have a thin secondary cell wall in addition to the primary cell wall. Tracheids have highly thickened cell walls that act as a mechanical support to the other cell types [44]. Vessel elements are wider cell types that form long tubes called vessels. The perforations facilitate the transport of nutrients and water throughout the biomass by interconnecting the vessels [51].

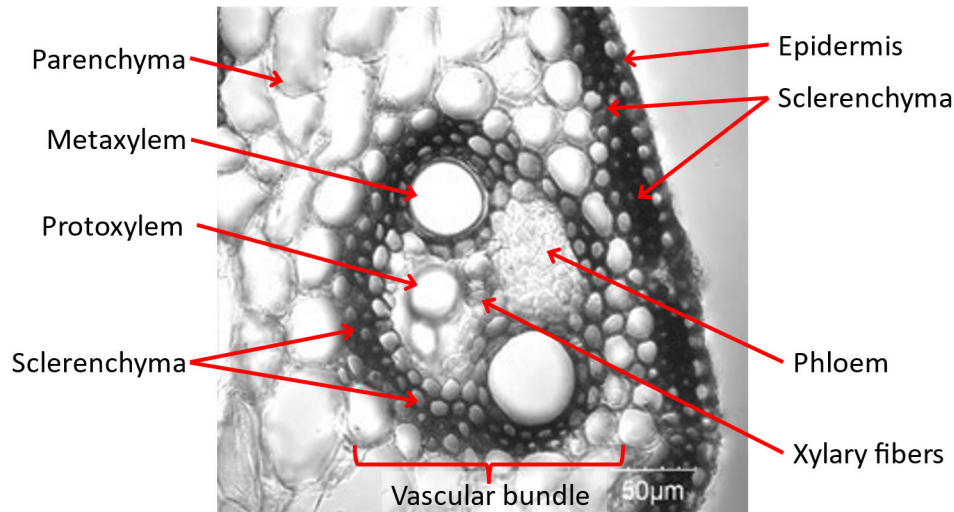


**Figure 2.6.** A brightfield micrograph of corn stem (grass) cross section showing the important cell types.

### 2.1.7 Biomass recalcitrance

Plants have developed intricate mechanisms to defend against microbial and chemical attacks on their cellulose, which combined is known as biomass recalcitrance. Biomass recalcitrance encompasses various molecular, chemical, and structural aspects of the plant cell wall [52]. The crystalline nature of cellulose and the aggregation of microfibrils make it naturally resistant to degradation. Additionally, lignin and hemicellulose contribute to recalcitrance by forming a physical barrier that impedes cellulose accessibility to enzymes [30]. As discussed in sections 2.1.1 to 2.1.6, the distribution of hemicellulose and lignin can significantly vary depending on numerous factors [19]. Consequently, biomass recalcitrance is influenced by factors such as cellulose crystallinity, arrangement of vascular tissues, the relative abundance of sclerenchymatous cells, the level of lignification, the type of lignin present, and the structural heterogeneity of cell wall components [53].

Biomass recalcitrance poses challenges to biofuel production by impeding the accessibility of cellulose to enzymes, limiting the mass transfer of water and chemicals, and consequently raising the overall process cost [8]. Lignin functions as a physical barrier that restricts the accessibility of cellulose and has been observed to irreversibly adsorb deconstruction chemicals, thereby impeding their ability to interact with the cellulose [54]. The presence of acetyl groups in hemicellulose contributes to resistance against cellulose hydrolysis. However, the impact of hemicellulose on biomass recalcitrance is generally less severe than that of lignin and cellulose crystallinity [52].

## 2.2 Lignocellulosic biofuel production

Various methods are available for converting biomass into energy [55]. It can be directly combusted to generate heat or transformed into syngas ( $\text{CO} + \text{H}_2$ ) or liquid transportation fuels. The conversion of biomass into liquid fuels can be achieved through two main routes: thermochemical and biochemical. The thermochemical route, also known as the biomass-to-liquid (BTL) conversion process, involves the pyrolysis or hydrothermal liquefaction of biomass. Pyrolysis is the degradation of biomass at high temperatures in nonoxidizing conditions to produce biochar, bio-oil, and pyrolysis gas. [56]. The generated gases can then undergo further catalytic or biological processing to transform them into fuels [57]. In the biochemical route, the polysaccharides in lignocellulosic biomass are converted to monomeric sugars, which are fermented by microorganisms into fuels and chemicals [34]. The deconstruction process usually involves three stages: pretreatment, enzymatic hydrolysis, and fermentation (Figure 2.7) [58]. The pretreatment overcomes the inherent biomass recalcitrance and improves cellulose accessibility to enzymatic degradation [9]. Enzymatic hydrolysis breaks down the pretreated biomass into monomeric sugars. These sugars are then fermented to bioethanol and other valuable products by microorganisms like yeast and bacteria [59].

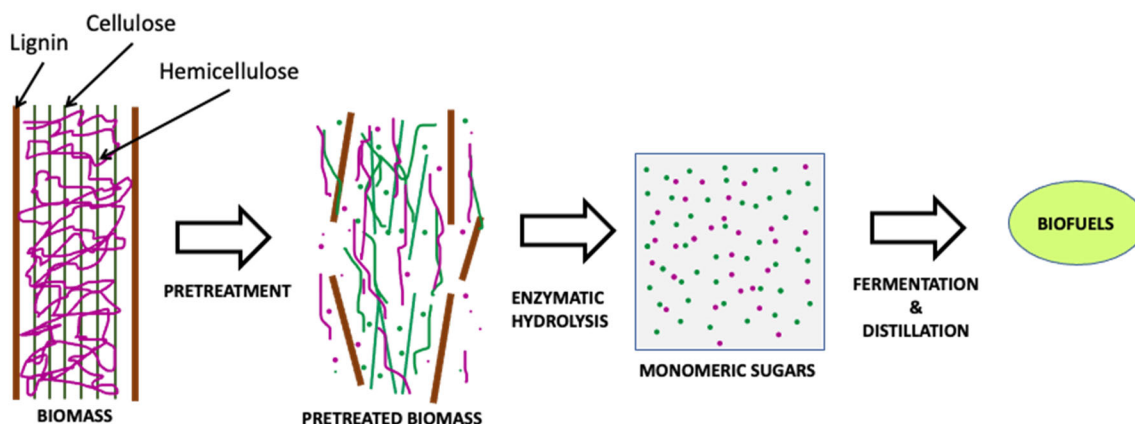


Figure 2.7. Biochemical conversion of lignocellulosic biomass. Reproduced based on [60].

### 2.2.1 Pretreatment

The main objectives of pretreatment are to efficiently generate readily-digestible, carbohydrate-rich solids suitable for enzymatic hydrolysis; while preventing formation of inhibitory compounds that can be toxic to fermentation microorganisms; and, in some cases, extracting high-quality lignin that can be marketed as a co-product [61]. Several pretreatment technologies have been developed and are often classified as physical, chemical, physicochemical or biological. Physical processes include size reduction, fiber separation, or delamination by milling or grinding. Physical pretreatments enhance enzymatic hydrolysis by reducing the biomass crystallinity and increasing the surface area [9]. Due to their relatively lower energy efficiency, physical pretreatment methods are not adopted as stand-alone pretreatment and are more suitable when used in combination with chemical pretreatment methods [62]. Biological pretreatment involves

using fungi or other microorganisms to degrade lignin while leaving the polysaccharides mostly unaffected [63]. Biological methods often require longer processing times, and there is usually some degradation of carbohydrates, which makes them less favorable in large-scale applications. Chemical and physicochemical pretreatment methods are cost-effective and have been studied extensively in the past. Some well-known chemical pretreatment methods are acid, alkali, ionic liquid, and ozonolysis [64-66]. Important physicochemical pretreatment methods are ammonia fiber expansion (AFEX), steam explosion, wet oxidation, and carbon dioxide explosion [67]. There are several advantages and disadvantages to each of these pretreatment technologies. As the ultimate goal of pretreatment is overcoming biomass recalcitrance, the choice of pretreatment method is influenced by the diversity of chemical composition and structure (as described in 2.1.6.) [10, 53]. In this dissertation, based on the method development requirements, the primary focus is on three specific pretreatment methods: dilute acid, dilute alkali, and ammonia fiber expansion (AFEX).

### ***2.2.1.1 Dilute acid pretreatment***

Dilute acid pretreatment, most commonly using sulfuric acid, but sometimes hydrochloric or phosphoric acid, reduces biomass recalcitrance through acid-catalyzed hydrolysis of hemicellulose into fermentable sugars [12]. The temperature range for dilute acid pretreatment varies from 80-210 °C and the residence time varies between few minutes to an hour, depending on the temperature [68, 69]. Combined severity is a combined metric based on the pretreatment conditions that depends on the acid concentration, temperature, and residence time. Optimum combined severity is the range at which the hemicellulose is converted into its monomeric sugars but not converted into furfural and 5-hydroxymethylfurfural. At extremely high severities, partial hydrolysis of cellulose occurs, which reduces the degree of polymerization of the cellulose [70]. Dilute acid pretreatment does not result in lignin fragmentation, however the lignin can relocalize and condense as spherical droplets on the cell wall surface [70, 71]. All these mechanisms result in an increase in pore size and surface area that improves subsequent enzymatic hydrolysis of cellulose. The main drawbacks of dilute acid pretreatment include the formation of inhibitory compounds that are toxic to fermentation microorganisms and the need for expensive reactor materials due to the corrosive nature of the acids [72].

### ***2.2.1.2 Dilute alkali pretreatment***

In contrast to dilute acid pretreatment, dilute alkali pretreatment is carried out at lower temperatures and times ranging from hours to days. The commonly used chemicals for alkali pretreatment are sodium, potassium, calcium, and ammonium hydroxide [73]. Sodium hydroxide is the most effective among these options. Solubilization of lignin through saponification of the  $\beta$ -O-4 bonds in lignin is the main mechanism of alkali pretreatment. This process also removes acetyl and uronic acid ester groups from hemicelluloses. As a result, the biomass porosity increases, facilitating access to the cellulose and hemicellulose during enzymatic hydrolysis. The solubilization of lignin also causes an expansion in the biomass, which increases the overall surface area. This swelling effect is a characteristic of alkali pretreatment [64, 65]. Alkali pretreatment is

influenced by the catalyst loading, solid-to-liquid ratio, temperature, and residence time [74]. Sugar degradation is lower during alkali pretreatment compared to acid pretreatment, however the lignin structure can be destroyed making it less suitable as a feedstock for coproducts [75].

### **2.2.1.3 AFEX pretreatment**

During AFEX pretreatment, moist biomass (0.1 to 2.0 g H<sub>2</sub>O/g dry biomass) is exposed to liquid anhydrous ammonia at a high pressure and temperature for a limited time and then rapidly depressurized [76]. The main mechanisms of AFEX are disruption of lignin-carbohydrate linkages, cleavage of hemicellulosic ester linkages, and partial reduction of cellulose crystallinity, all of which leads to increased enzymatic hydrolysis of cellulose. The rapid decompression of ammonia due to pressure release relocalizes biomass components and forms large pores in the cell wall, which makes the cellulose more accessible for enzymatic hydrolysis. The main parameters influencing the effectiveness of AFEX pretreatment are ammonia loading, temperature, pressure, moisture content, and residence time [77]. Liquid ammonia loading can vary between 0.3 to 2.0 g NH<sub>3</sub>/g dry biomass. The temperature for AFEX pretreatment can vary between 90-180 °C and the residence time between 5 and 60 min. Because ammonia is released as a vapor, following AFEX pretreatment the biomass is removed as a solid from the reactor and there is no loss of hemicellulose or lignin in a separate liquid stream, unlike in other pretreatment methods. During AFEX, ammonia (NH<sub>3</sub>) and hydroxide ions (OH<sup>-</sup>) penetrate the cell wall and break the ester linkages between hemicellulose and lignin through ammonolysis and hydrolysis, respectively, to form amides or acids [78]. Removal of acetyl groups from hemicellulose results in acetamide and acetic acid formation, which can be inhibitory to microorganisms [79]. However, several studies report that the quantities of such inhibitory compounds are relatively lower for AFEX than other chemical pretreatment methods [20, 80, 81]. Ammonia cost and its ineffectiveness on high lignin containing feedstocks like wood are some drawbacks of AFEX pretreatment [9].

## **2.2.2 Enzymatic hydrolysis**

The cellulose and hemicellulose in lignocellulosic biomass can be hydrolyzed into monomeric sugars using either concentrated acids or enzymes. Enzymatic hydrolysis is the preferred approach due to its lower energy requirement, milder process conditions, and reduced formation of fermentation inhibitors [82]. Three cellulase enzymes work synergistically to achieve complete hydrolysis of cellulose to glucose: endoglucanases, cellobiohydrolases, and  $\beta$ -glucosidases (**Figure 2.8**Error! Reference source not found.). Endoglucanases target the glucosidic linkages in the interior amorphous regions of cellulose [83]. Cellobiohydrolases act on both the reducing and non-reducing ends found in the crystalline regions of the cellulose chains, resulting in cellobiose formation. Finally,  $\beta$ -glucosidase hydrolyzes cellobiose into glucose monomers [61]. The intricate arrangement of cell wall polymers adds complexities to the enzymatic hydrolysis process.

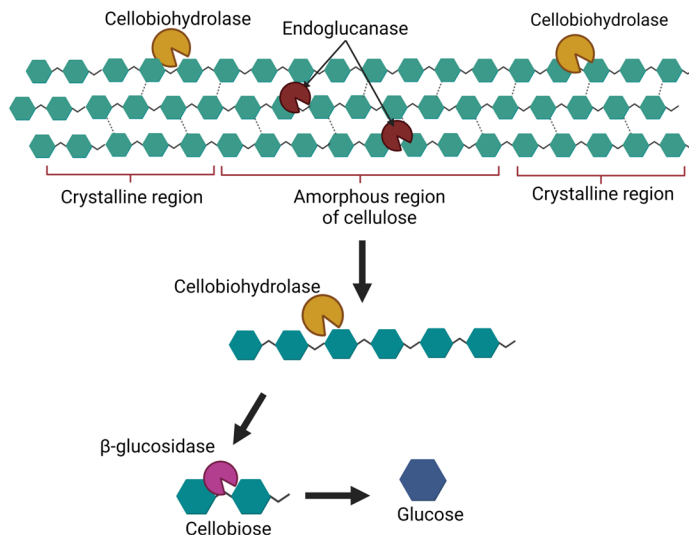


**Figure 2.8. Enzymatic hydrolysis.** Created with BioRender.com. Reproduced based on [84].

Due to the diversity of monomers that form hemicellulose (as described in 2.1.2), the enzymes required to hydrolyze hemicellulose are far more complex than the cellulases. Endo  $\beta$ -1-4-xylanase and  $\beta$ -xylosidase are responsible for the hydrolysis of xylan [85]. Other hemicellulose components are hydrolyzed by accessory enzymes such as  $\alpha$ -L-arabinofuranosidase,  $\alpha$ -glucuronidase,  $\alpha$ -galactosidase, acetyl xylan esterase, and ferulic acid esterase [86]. The combined effect of the cellulases and hemicellulases depends on the nature of the substrate and the pretreatment technology used [87]. For most types of pretreated biomass, a complex mixture of enzymes is required to achieve efficient biomass deconstruction.

### 2.2.3 Fermentation

During fermentation, microorganisms like yeast or bacteria utilize the monomeric sugars for their growth while simultaneously producing alcohol and carbon dioxide [88]. For efficient fermentation, the chosen microorganisms should possess high specific productivity, alcohol tolerance, and a wide pH range. The most employed microorganisms for fermentation are the yeast *Saccharomyces cerevisiae* and the bacterium *Zymomonas mobilis* [89, 90]. *S. cerevisiae* exhibits favorable traits such as the ability to ferment various hexoses, high product yield, and high product concentration. On the other hand, *Z. mobilis* offers advantages over *S. cerevisiae*, including faster glucose consumption and lower biomass accumulation [91]. Since hemicellulose hydrolysis generates xylose and other pentose sugars, engineered strains of *S. cerevisiae* and *Z. mobilis* have been developed to enable pentose fermentation [92, 93].

Some chemicals produced during the pretreatment can have detrimental effects on fermentation microorganisms. They can impede microbial growth by reacting with the cellular components and causing cellular membrane damage [94]. The type and concentration of fermentation inhibitors is determined by various pretreatment factors, including the chemical used and process conditions such as temperature, residence time,



and pH. Inhibitors generally fall into three main categories: aromatic compounds, furan derivatives, and weak aliphatic acids [95]. Acetic acid is a common inhibitor generated from hemicellulose hydrolysis during acid, alkali, and AFEX pretreatments. Aromatic inhibitors are typically derived from lignin and include compounds such as vanillin and 4-hydroxybenzaldehyde [59]. Furfural and 5-hydroxymethylfurfural (HMF) are examples of inhibitors formed from the degradation of pentoses and hexoses during the pretreatment process. Additionally, inhibitors like levulinic acid and formic acid are produced by the further degradation of 5-hydroxymethylfurfural [20, 59].

#### **2.2.4 Analytical techniques for evaluating biomass deconstruction**

Evaluating the biomass deconstruction at different stages provides valuable insights to understand biomass recalcitrance. The liquid stream is typically analyzed for the release of sugars and inhibitors, while the composition of the residual biomass is analyzed to understand modifications to cell wall polymers during pretreatment and enzymatic hydrolysis. However, in order to understand tissue-specific variations in biomass recalcitrance, it is also important to investigate morphological changes in the biomass at both macroscopic and microscopic levels [63, 96]. There are numerous characterization techniques used to evaluate the effect of deconstruction on biomass properties such as surface and structural morphology and chemical composition [97]. Morphological changes can be analyzed using microscopic techniques like scanning electron microscopy (SEM), transmission electron microscopy (TEM), confocal laser scanning (CLSM), and atomic force microscopy (AFM) [98]. Functional group-related information can be analyzed using Raman spectroscopy, Fourier-transform infrared spectroscopy (FT-IR), and NMR. Physical properties like crystallinity and porosity can be analyzed using X-ray diffraction (XRD) and solid-state nuclear magnetic resonance (NMR) [99]. Changes in structural carbohydrates and lignin can be analyzed using the standard laboratory procedures provided by NREL for the raw biomass and at various stages of the bioconversion [52].

#### **2.2.5 High-solids enzymatic hydrolysis**

To make biofuel production economically viable, it has been suggested that the fermentation broth should contain a minimum of 4 % bioethanol concentration before undergoing distillation [100]. A promising strategy to achieve this is by conducting the deconstruction process at a high biomass concentration during both pretreatment and enzymatic hydrolysis. Starting with a larger biomass loading results in higher sugar concentrations after enzymatic hydrolysis, resulting in higher bioethanol concentrations following fermentation [83]. The advantages of operating at higher solids loadings includes lower equipment costs due to reduced volume, lower operating costs due to reduced energy requirements, lower downstream processing costs due to higher concentrations of sugars in the product stream, and lower water consumption [101-103]. Typically, the term "high-solids" refers to a solid loading greater than 15% w/w dry biomass, or the absence of free water in the slurry at the beginning of the enzymatic hydrolysis process.

High solids loading enzymatic hydrolysis presents unique technical challenges related to low water availability [104]. Water plays a crucial role in enzymatic hydrolysis as a reactant for breaking glycosidic bonds in cellulose and hemicellulose; a medium for the diffusion of enzymes, substrate, and released sugars; and a viscosity-reducing agent for efficient mixing [105]. When water is limited during high-solids loading, several difficulties arise. First, the biomass slurry becomes highly viscous, impeding the diffusion of enzymes [106]. Second, enzymes experience greater end-product inhibition due to the high concentration of monomeric sugars produced. Cellobiose binds to the catalytic surface of cellobiohydrolase and endoglucanase, inhibiting their activity. Glucose primarily inhibits  $\beta$ -glucosidase, while also affecting cellobiohydrolase and endoglucanase to a lesser extent. Similarly, monomers like galactose, xylose, arabinose, and mannose can inhibit various hemicellulase enzymes [95, 107]. Third, achieving uniform temperature (e.g., 50 °C) and desired pH throughout the biomass slurry can be challenging due to localized hot spots that may form within the mixture [108]. However, maintaining optimal temperature and pH is crucial as enzyme-based reactions are highly sensitive to these factors [109].

Lignocellulosic biomass slurries exhibit non-Newtonian fluid behavior, displaying a pseudoplastic nature where viscosity decreases with increasing shear rate [100]. When these slurries are mixed, the fibers within the biomass tend to form interconnections. This behavior becomes more pronounced at high solids loading due to the presence of a large quantity of insoluble solids. At high solids loading (>15% w/w dry biomass) where water availability is limited, the lubrication between biomass fibers is significantly reduced, resulting in a more limited mixing of the biomass slurry. This indicates little to no convective mixing resulting in high energy consumption for mixing equipment [110]. The improper mixing can also lead to inadequate contact between the enzymes and the biomass, which is crucial for effective saccharification. The pseudoplastic behavior of the biomass slurries has a greater impact during the initial stages of enzymatic hydrolysis [111]. As the reaction progresses, the enzymes break down the insoluble solids and reduce fiber size, resulting in the liquefaction of the biomass slurry [101]. Additionally, the chemical composition of the feedstock can affect the viscosity, with feedstocks containing higher amounts of lignin and hemicellulose typically exhibiting increased viscosity. Analyzing the rheological properties of biomass slurries can provide valuable insights for selecting appropriate process parameters for enzymatic hydrolysis [112, 113].

#### **2.2.5.1 High solids enzymatic hydrolysis configurations**

Most often laboratory scale enzymatic hydrolysis is performed in Erlenmeyer flasks with a solids loading of less than 10% w/w dry biomass. The shake flask method operates as a batch process, where the entire pretreated biomass, water, and enzymes are added all at once, and the products are collected after enzymatic hydrolysis is complete. To investigate the biomass deconstruction process under conditions relevant to industry, it is crucial to conduct pretreatment and enzymatic hydrolysis at high solids loading exceeding 15% w/w dry biomass (**Figure 2.9**) [109]. However, at solids loadings above 10% w/w dry biomass, using a stirrer or shaking incubator becomes ineffective for proper

mixing [114], and results in uneven enzyme distribution, and localized accumulation of sugars, reducing hydrolysis efficiency [115].

Various strategies have been studied as alternative methods to overcome the difficulties arising during high solids loading hydrolysis including fed-batch addition of biomass to shake flasks, using horizontal bioreactors employing gravitational mixing, and the addition of surfactants to facilitate adsorption and desorption of enzymes on the substrate [116, 117]. In the fed-batch approach, the pretreated solids are introduced to the system in multiple installments, typically exceeding three or four, at different time points. This gradual addition of solids during the liquefaction stage reduces the amount of insoluble solids present at any given time [113], but increases the likelihood of microbial contamination during the process. Gravitational mixing minimizes particle settling and local accumulation of sugars within the reactor to ensure better enzyme distribution [102]. At industrial scales, horizontal reactors with paddles have efficiently increased sugar yields. Surfactant additives like carboxymethyl cellulose, polyethylene dioxide, and polyacrylamide have been used to alter the rheological properties of lignocellulosic biomass slurry to improve enzyme distribution [118].

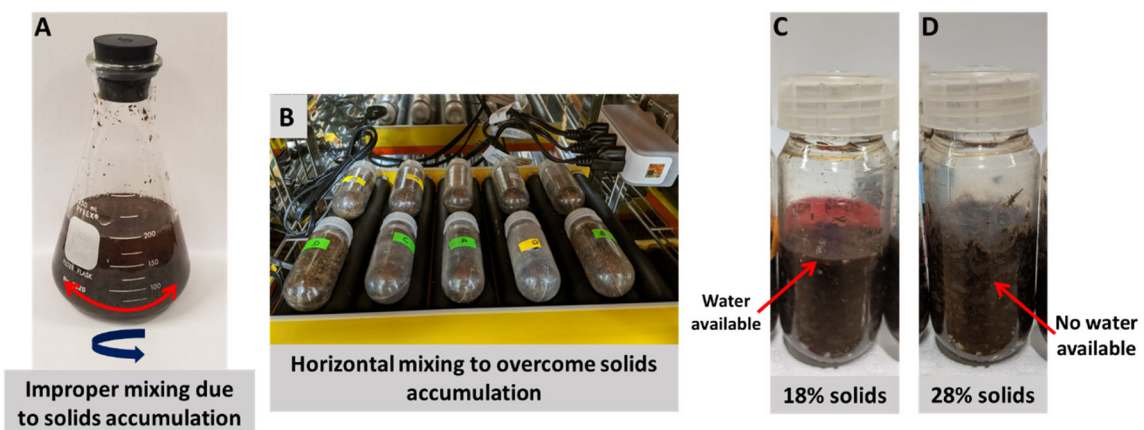


**Figure 2.9.** A) A shake flask (batch mode) showing accumulation of solids along the periphery, which leads to improper mixing, B) Horizontal mixing using a laboratory scale roller aide in overcoming solids accumulation, C) Low water availability in 18% solids w/w dry biomass enzymatic hydrolysis, D) No water available in 28% solids w/w dry biomass enzymatic hydrolysis.

### **2.2.5.2 Fermentation inhibition at high solids loading**

The inhibitory compounds produced during pretreatment are detrimental to the fermentation microorganisms (as described in 2.2.3). This situation is more severe at high solids loading due to the high concentration of these inhibitory compounds [119].

Washing the pretreated biomass before enzymatic hydrolysis, detoxifying the hydrolysates before fermentation, and designing pretreatment methods that produce minimal inhibitory compounds are the potential solutions to this problem [105]. Lu et al. found that washing the pretreated solids resulted in an increased ethanol yield for steam

exploded corn stover. The ethanol yield was 94% at 30% (w/w) solids loading for washed pretreated solids whereas it was 64% at 20% (w/w) solids loading for unwashed pretreated solids [119]. The use of activated charcoal to remove acetic acid, using laccase to oxidize phenolic inhibitors, and treating the hydrolysates with ion-exchange resins to remove inhibitors were some of the effective detoxification methods [120-122]. In a previous study on the scale up of enzymatic hydrolysis of alkaline hydrogen peroxide pretreated corn stover, they incorporated activated charcoal detoxification on the hydrolysates prior to fermentation. The results revealed that the fermentation batch that was treated with activated charcoal exhibited a more rapid utilization of glucose and xylose. However, the overall fermentation efficiency remained consistent at approximately 68% for both the conditions, with and without activated charcoal treatment [123]. Cannella et al. reported that adding cationic polyethylenimine (PEI) to SO<sub>2</sub> impregnation pretreated spruce samples aided in the adsorption of furan and aliphatic acids. They reported that there was no fermentation without PEI addition. The ethanol yield was higher for post hydrolysis PEI addition (37.8 g/kg) than for pre hydrolysis PEI addition (35.4 g/kg) [124]. The main disadvantage of the washing and detoxifying steps is the increase in ethanol production cost up to 22%, which is unfavorable for the industrial scale [125, 126]. Several studies investigated the elimination of the washing step through different approaches [83]. Lau et al. studied the inhibitory compound effect on fermentation for AFEX pretreatment of corn stover and distillers grain without the washing step. After enzymatic hydrolysis at 18% (w/w) solids loading, it resulted in 87-103% metabolic ethanol yields (based on consumed glucose and xylose) [126]. Further, through the use of *S.cerevisiae* 424A (LNH-ST), a strain engineered for improved xylose fermentation, the fermentation of AFEX pretreated corn stover hydrolysates resulted in a higher ethanol production of 0.17 g/L/hr for unwashed pretreated solids than 0.12 g/L/hr for washed pretreated solids [103]. Additionally, Lau et al. investigated the effect of the hydrolysate pH on fermentation yield and found that a pH of 5.5 at 30 °C is optimum for AFEX pretreated corn stover and *S.cerevisiae* [103]. Other studies have also reported an increase in ethanol yield when the hydrolysate pH is adjusted to 5.5 or 6 before fermentation. These were carried out on steam exploded and acid pretreated corn stover [127, 128]. These studies imply that eliminating the detoxifying step is feasible for AFEX pretreatment and by achieving an appropriate hydrolysate pH, it is possible to improve fermentation yields at high solids loading conditions.

## 2.3 Imaging in lignocellulosic biofuel production

Determining the morphological changes in biomass during pretreatment is important to understand the heterogeneity in biomass recalcitrance, which is influenced by the arrangement of cell wall components such as cellulose, hemicellulose, and lignin (as explained in sections 2.1). Microscopic techniques are crucial for analyzing the breakdown of lignocellulosic biomass (**Figure 2.10**) [98], as they allow us to investigate changes in particle size and structural changes within the plant microstructure during pretreatment and enzymatic hydrolysis. While compositional analysis of the hydrolysates can help assess sugar yield and concentration, imaging is necessary to observe localized changes in different regions of the biomass [129].

Over the past few decades, there have been significant advancements in microscopic techniques, such as label-free imaging and immunolabeling. These advancements have paved the way for new opportunities in qualitatively and quantitatively understanding the deconstruction of cell walls [130]. Electron microscopy and optical microscopy employ light beams and electron beams, respectively, to interact with samples and provide spatial information at both the micrometric and nanometric scales [98, 131, 132]. Atomic force microscopy uses a mechanical probe that contacts the sample surface to obtain the topochemical characteristics of the cell wall. Confocal Raman microscopy is a nondestructive method that reveals the chemical composition the cell wall at a microscopic level using the inelastic scattering of monochromatic light [98]. Fluorescence microscopy is used to visualize cell wall components and biomass deconstruction by taking advantage of lignin autofluorescence and can observe hemicellulose and enzyme interactions through immunolabeling [131, 133].

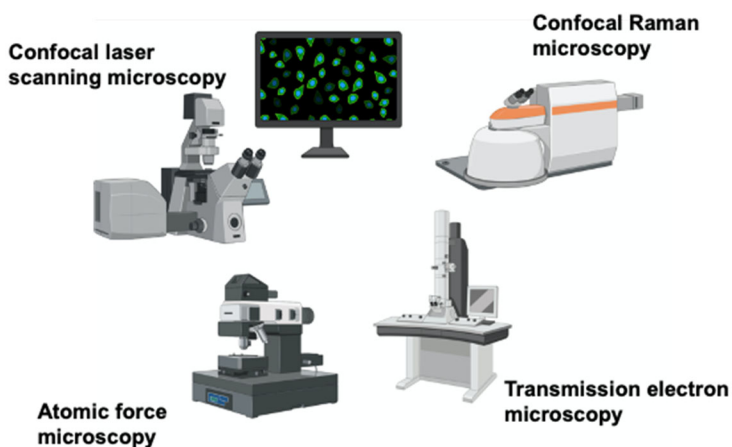


**Figure 2.10.** Commonly used imaging techniques to elucidate cell wall properties. Created with BioRender.com

### 2.3.1 Electron microscopy

Electron microscopy employs a beam of electrons and electromagnetic lenses to generate images of a specimen. The main advantage of electron microscopy over traditional light microscopy is the shorter wavelength of electrons, enabling the acquisition of high-resolution images. There are two fundamental types of electron microscopy: transmission electron microscopy (TEM) and scanning electron microscopy (SEM) [98]. The high magnification in TEM is particularly valuable in studying the structural characteristics of the middle lamella and secondary cell wall in plant cells during biomass deconstruction. In TEM, a high-energy electron beam passes through an extremely thin sample, experiencing scattering [134-136]. The transmitted (scattered) electron beam then interacts with a fluorescent screen or an electron detector to produce the resulting images (**Figure 2.11A** Error! Reference source not found.). To avoid electron scattering by gases, TEM must be conducted in a vacuum. For lignocellulosic biomass analysis with TEM, it is necessary to embed the biomass in resin. The obtained sample sections are stained with potassium permanganate before imaging to provide contrast to differentiate between cell

wall layers based on lignin concentration [71]. These sections are mounted on a 3 mm diameter TEM grid, typically composed of copper. In contrast to TEM, SEM is lower resolution and is typically used to visualize the surface of the biomass, rather than the interior of the cell wall. To be effective, the biomass sample is coated with a conductive and protective layer, such as gold or tungsten. The source electron beam interacts with the sample, leading to ionization and the emission of secondary and backscattered electrons (**Figure 2.11B**) [137]. Secondary electrons with energy below 50 eV are utilized to achieve topographic contrast in the images [138]. SEM has been used to determine the structural changes in lignin during pretreatment. Particularly, lignin droplet formation on the surface of the feedstocks during dilute acid pretreatment and steam explosion pretreatment have been elucidated using SEM in several studies [139-141]. Numerous previous studies have evaluated lignin distribution between the different cell wall layers using SEM and TEM, and found the highest lignin content in the compound middle lamella [33, 134, 136, 142]. Surface erosion, relocalization of cell wall components, and structural changes in the biomass during pretreatment can be studied using SEM [73, 130, 143]. Combined with potassium permanganate staining, TEM has been used to highlight the changes in lignin distribution within the cell wall for switchgrass during alkali pretreatment and corn stover during AFEX pretreatment [73, 143]. Despite being used widely, the potential drawbacks of SEM and TEM are that the drying, cutting, and metal coating procedures during sample preparation can alter the cell wall morphology and the electron beam can damage the sample [99]. Nevertheless, electron microscopy has been successfully used to visualize cellulose microfibrils and the nanoscale morphological changes during pretreatment and enzymatic hydrolysis [144].

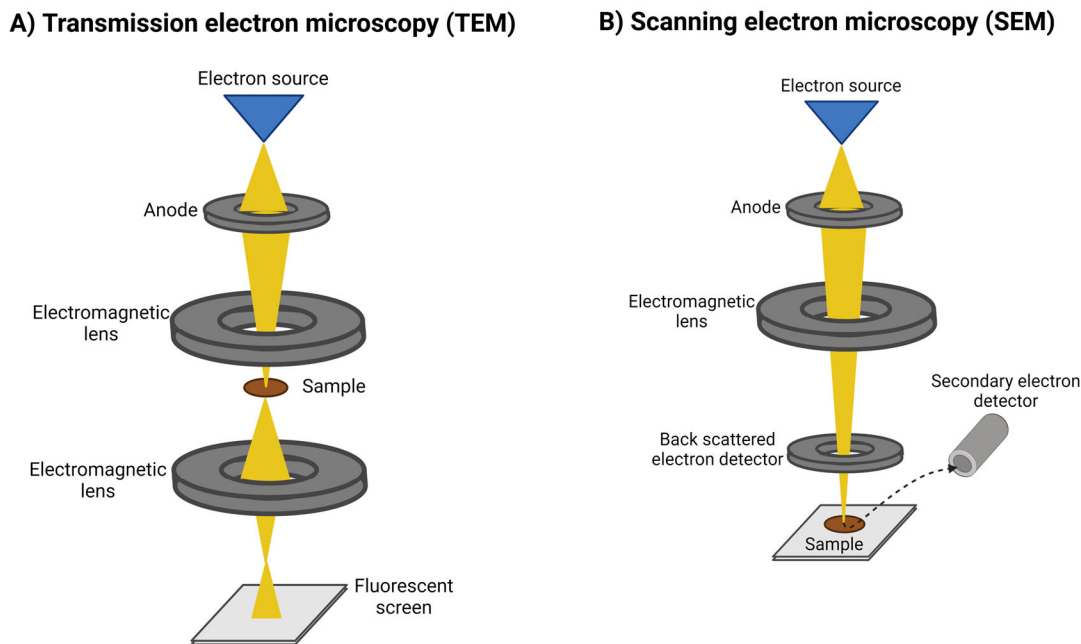


**Figure 2.11. Schematic representation of A) SEM and B) TEM. Reproduced based on [145] and [146] using BioRender.com**

### 2.3.2 Atomic force microscopy

Atomic force microscopy (AFM) measures the attractive and repulsive forces between a scanning probe and the sample to obtain a high resolution, three-dimensional replica of the biomass surface [147]. AFM does not require sample staining or labeling, thus preserving the structural integrity during sample preparation. The surface of the sample is probed using a sharp tip located at the end of a cantilever (**Figure 2.12A**). Information about the sample surface is obtained by reflecting a laser beam off the backside of the cantilever onto a photodiode, [98]. Feedback electronics provides signals to raise or lower the probe tip based on the changes in sample topography. The applied voltage used to move the tip is monitored to generate the image [148-150]. Most scanners have a range of around 100 x 100  $\mu\text{m}$ , and the tip at the end of the cantilever needs to be within approximately 10  $\mu\text{m}$  of the sample [149]. The nanostructural changes of cellulose microfibrils during deconstruction can be visualized using AFM. AFM is most commonly used in combination with other analytical techniques to study the interactions between lignocellulosic feedstocks and enzymes. Lambert et al. tracked the progress of enzymatic hydrolysis of a lignocellulosic film (prepared using poplar extracted lignin and cellulose nanofibrils) to elucidate the lignin-based differences in biomass recalcitrance [144]. Ding et al. used AFM, along with other imaging techniques to determine the difference in hydrolysis of delignified corn stem secondary walls by large multi-enzyme bacterial cellulosomes compared to small fungal cellulases [27]. The difference between lignin-enzyme and cellulose-enzyme interactions were studied AFM tips coated with kraft lignin and hydroxypropyl cellulose for *Trichoderma reesei*, a commercial cellulase system [151]. However, AFM has limitations in terms of scan range and the potential for the formation misleading artifacts. The topographic signals from the biomass surface could overlap with the gap-with controlling mechanism of the AFM, thereby generating artifacts leading to data misinterpretation [152].

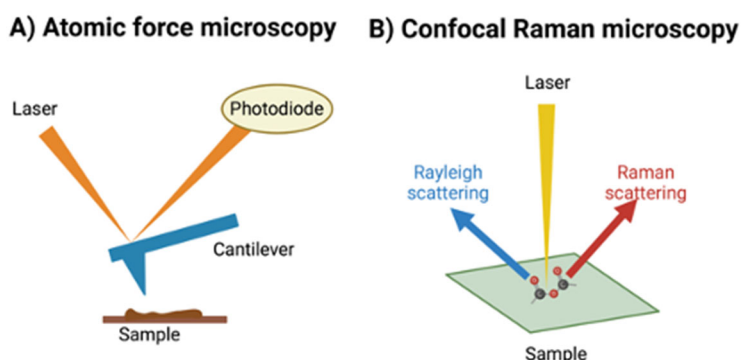


**Figure 2.12.** Schematic representation of A) atomic force microscopy (AFM) and B) confocal Raman microscopy. Created with BioRender.com. Reproduced based on [98].

### 2.3.3 Confocal Raman microscopy

Confocal Raman microscopy (CRM) is a nondestructive imaging method to obtain simultaneous chemical and structural information of the plant cell wall. Raman imaging

is based on the inelastic (Raman) scattering of monochromatic light during the interaction between the source photon laser and the sample (**Figure 2.12B**) [98]. The resolution obtained in Raman microscopy can be of a single cell, or even a single layer of the cell wall. Different cell wall polymers scatter light with different characteristic bands: cellulose: 870-800  $\text{cm}^{-1}$ , hemicellulose: 515-475  $\text{cm}^{-1}$ , lignin: 1602  $\text{cm}^{-1}$  [153, 154] and can be mapped simultaneously. Important bottlenecks while using CRM include long acquisition times, limited specificity due to the complex distribution of the cell wall polymers, and the autofluorescence behavior of the cell wall that interferes with signal acquisition [155, 156]. These limitations can be overcome by using charge coupled devices to reduce acquisition time, obtaining extremely thin samples to improve chemical specificity, and photobleaching to quench the fluorescence signals [156]. CRM has been used for real-time, nondestructive, *in situ* imaging of changes in biomass structure and composition during pretreatment [129, 157]. During alkali pretreatment of miscanthus, CRM revealed the preferential removal of lignin from the primary cell wall without any significant change in the cellulose structure [158], and a clear difference in the distribution of hydroxycinnamates, lignin, and cellulose between the parenchyma cell walls and the sclerenchyma fibers [159]. During ionic liquid pretreatment of poplar, CRM was used to determine that the dissolution and swelling caused by the ionic liquid was more prominent in the amorphous cellulose regions than the crystalline cellulose [160, 161]. Lignin and carbohydrate spatial distribution during  $\gamma$ -valerolactone/sulfuric acid/water pretreatment of *Eucalyptus* was evaluated using CRM to determine the optimum acid concentration for effective pretreatment. At 100 mM of sulfuric acid, the lignin solubility increased drastically in all cell wall regions except for a few traces in the compound middle lamella [162].

### 2.3.4 Fluorescence microscopy

Due to its versatility, fluorescence microscopy can be used to visualize a wide variety of lignocellulosic feedstocks. The ability to fluorescently tag proteins, glycans, and enzymes allows for selective observation of individual moieties [163]. Fluorescence microscope configurations can be divided into epifluorescence or confocal laser scanning microscopy (CLSM). Epifluorescence uses a broad-spectrum excitation light source to illuminate the entire field of view (wide field mode) (**Figure 2.13**). Epifluorescence microscopy is effective for thin samples ( $<10 \mu\text{m}$ ). The sample is usually mounted on a coverslip, which is in contact with the objective lens. Commonly used lens magnification varies between 10x and 100x. An excitation filter is combined with the light source to select the appropriate wavelength for sample excitation [98, 164]. A dichroic mirror separates the excitation and emission spectra, while an emission filter determines the transmission wavelength band. An imaging device, such as an electron multiplication charge-coupled device (EMCCD) camera, captures the emitted photons, which translates them into an image. The pixel intensity is proportional to the fluorescence emitted. Through proper calibration, it is possible to quantify the concentration of fluorescence from biochemicals or fluorescently labeled glycans [98]. On the other hand, confocal laser scanning microscopy (CLSM) utilizes a laser as the excitation source for point illumination and a photomultiplier detector (**Figure 2.13**). CLSM is similar to epifluorescence microscopy but offers improved axial resolution through optical sectioning. It is particularly useful



for imaging thick samples (approximately 100  $\mu\text{m}$ ) by capturing multiple individual sections of the sample [165]. The cell wall structure before and after digestion can be obtained through fluorescence microscopy, which is useful to determine pretreatment or enzymatic degradation mechanisms [131]. During biomass deconstruction, CLSM has been used to investigate the changes in lignin using lignin autofluorescence (2.3.4.1) and hemicellulose and pectin using immunofluorescence labeling (2.3.4.2) [132, 166]. Time lapse evaluation of lignin autofluorescence using CLSM of poplar samples during ionic liquid pretreatment at room temperature showed a clear reversible swelling of the cell wall towards the lumen and not the middle lamella [160]. During CLSM imaging of ionic liquid pretreatment of switchgrass at higher temperatures, the swelling effect of the ionic liquid was followed by rapid dissolution of cell wall structure [167]. CLSM imaging has also been used to evaluate differential effects of pretreatment on cell types. During ionic liquid pretreatment of rice straw, the sclerenchyma cell walls near the vascular bundles showed more swelling and reduced autofluorescence than the epidermal sclerenchyma cell walls [168].

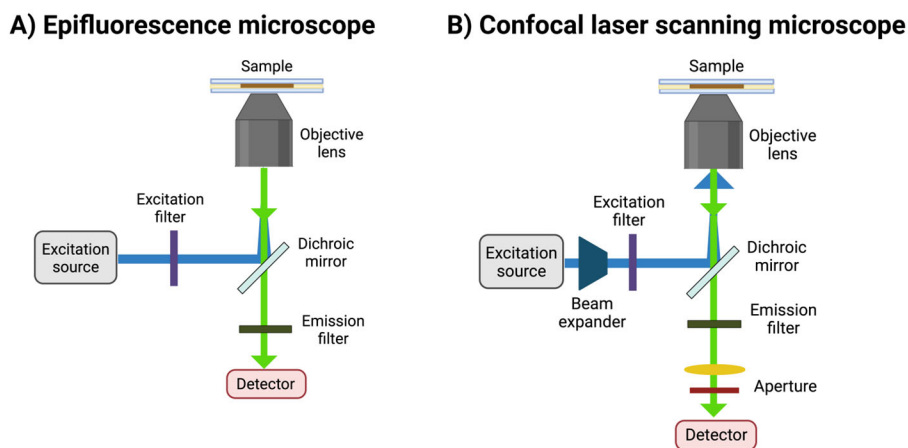


Figure 2.13. Schematic representation of A) Epifluorescence microscope and B) Confocal laser scanning microscope. Created with BioRender.com. Reproduced based on [169].

### 2.3.4.1 Lignin autofluorescence

Plant cell walls exhibit fluorescence under UV or visible light excitation due to the presence of lignin, which has multiple fluorophores responsible for autofluorescence (**Figure 2.14**). Phenylcoumarans, stilbenes, coniferyl alcohol, biphenyls, and dibenzodioxocins have been identified as lignin chromophores [133]. In contrast, cell wall polymers like cellulose and hemicellulose are nonfluorescent. Mapping lignin autofluorescence through CLSM has been used to investigate lignin distribution in wood, photodegradation of wood, and structural characterization of different lignocellulosic feedstocks [170]. Lignin autofluorescence has been used to show reduced and variable lignification due to the downregulation of 4-coumarate CoA ligase (4CL) in Monterey pine [171], and a distinctly high lignin content in the secondary cell wall of pine compression wood compared to the middle lamella [172].

Lignin autofluorescence undergoes modification based on pH, chemical infiltration, and temperature [133]. In the biomass deconstruction process, several studies have used this to determine the effect of various pretreatment methods on lignin including hot water, chlorite, steam explosion, alkali, maleic acid, and sulfuric acid-catalyzed  $\gamma$ -valerolactone pretreatment [133, 173-176]. The high temperatures and acidic or alkaline conditions of several chemical pretreatments cause the breakage of  $\beta$ -aryl-ether bonds in lignin, which leads to a decrease in lignin autofluorescence after pretreatment [170, 177, 178]. Also, based on previous studies using fluorescence lifetime imaging microscopy (FLIM) of poplar during maleic acid, hot water and chlorite pretreatment, it was found that the lignin remaining in the pretreated residual biomass had shorter fluorescence lifetime than in the untreated biomass [174, 179]. Hence, relative quantitation of lignin autofluorescence through fluorescence microscopy can be used to characterize lignin changes during pretreatment.

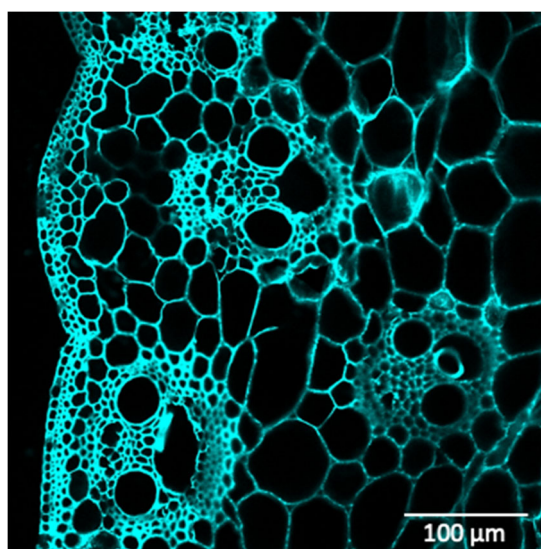


Figure 2.14. CLSM image of a corn stem section showing lignin autofluorescence. The excitation wavelength was 405 nm with a DAPI emission bandpass filter (480-550 nm).

#### **2.3.4.2 Immunolocalization**

Although cell wall polysaccharides are not fluorescent, they can also be visualized using CLSM either by staining or labeling with monoclonal antibodies [180, 181]. Understanding the location of specific cell wall polymers, both in their substituted and unsubstituted forms, is crucial for rapidly mapping the composition of lignocellulosic feedstocks [12, 182]. The specificity of monoclonal antibodies depends more on the precise epitope or range of epitopes they recognize rather than the polymer they are intended to identify. A wide selection of over 200 plant cell wall glycan-directed monoclonal antibodies (mAbs) is available in the globally used toolkit developed by Pattathil et al. [183]. These antibodies cover a diverse range of cell wall polymers and are organized hierarchically based on their binding specificities. This labeling approach is most effective when applied to unprocessed samples, where the epitopes remain unaltered [184]. However, imaging can be performed years after sample preparation through

fixation and embedding techniques. Embedding enables the production of thin sections thinner than 2  $\mu\text{m}$ , minimizing fluorescence interference [184]. Immunolabeling typically involves the use of a secondary antibody that can be visualized. Secondary antibodies are conjugated with fluorophores. In the 1980s, commonly used fluorophores for immunolabeling included fluorescein isothiocyanate and tetramethyl rhodamine isothiocyanate. These have since been replaced by more advanced options such as Alexa Fluor® Dyes (Invitrogen, Carlsbad, USA). It is important to note that immunolabeling has certain limitations, including its destructive nature, the high cost of antibodies, and limited permeability into the sample [98].

Immunolabeling has been used in a number of studies to evaluate the distribution of hemicellulosic sugars in plant cell walls and identify how this distribution changes following pretreatment. Using a combination of immunolabeling and autofluorescence imaging, pine compression wood was found to have higher lignin and  $\beta$ -(1,4)-galactan content compared to normal wood [172]. Detailed glycome profiling of miscanthus using a suite of monoclonal antibodies and immunolabeling were useful to differentiate the distribution of lignin and hemicellulose among organs, genotypes and found that lignin had the greatest effect on recalcitrance in stems [185]. The changes in the cell wall structure and composition during pretreatment can be accurately visualized using immunolabeling of the cell wall components [132]. The ultrastructural effects of extractive ammonia pretreatment of corn stover cell walls were evaluated using glycome profiling and immunohistochemistry with several xylan and arabinoxylan specific CCRC antibodies. They found that the hemicellulose was severely distorted after extracted ammonia pretreatment in addition to lignin removal [186]. Through immunolabeling using different cellulose specific CBM antibodies, a dramatic increase in cellulose accessibility was observed after delignification during ionic liquid pretreatment of rice straw samples [27]. Costa et al. evaluated the variability of hemicellulose content between the rind and the pith regions for six sugarcane variants through labeling mixed linkage glucans (MLG) and xylan. High xylan and low MLG content in the rind region was attributed to the high recalcitrance in the rind tissues [181]. Increased xylan accessibility due to the loss of hemicellulose during dilute acid pretreatment of corn stover from sclerenchymatous tissues have been studied using immunolabeling with LM10 and LM11 [187].

## 2.4 Microfluidics

The field of microfluidics involves the manipulation of small volumes of fluids within and around microstructures at a scale from 10 to a few 100  $\mu\text{m}$ . The large surface-area-to-volume ratio associated with microfluidic systems offers a great advantage in scaling down laboratory processes [188]. Microfluidic systems utilize different methods for fluid manipulation. These include pressure-driven flow, where external pressure sources or pumps are used to drive the fluid through the channels, and electrokinetic flow, where electric fields are applied to control the movement of charged particles or ions within the fluid [189]. Pressure-driven flow is regulated using micromixers, micropumps, and

microvalves within the system. Microfluidics enables high-throughput analysis by incorporating parallel channels or chambers [190]. Multiple experiments can be performed simultaneously within a single device, reducing the time and resources required [191].

Lab-on-a-chip (LOC) is an application of microfluidics used to carry out high throughput screening of samples. It is a compact platform that integrates various laboratory functions onto a single chip, enabling the manipulation and analysis of minute quantities of fluids, cells, and molecules [191, 192]. The construction of microfluidic devices encompasses multiple stages, including chip design, fabrication, fluid handling, and detection. Software tools like AutoCAD, SolidWorks, or specialized microfluidic design software aid in drafting of microfluidic channels, chambers, valves, and other components on the chip [193]. Fabrication is carried out through one or more of the following techniques: photolithography, soft lithography, injection molding, micromachining, and 3D-printing [190, 194, 195]. Techniques like electrokinetic, pressure-driven (pneumatic or hydraulic), or capillary-driven flow are employed to drive the movement of fluids through microchannels and perform various operations like mixing, splitting, and metering. Lab-on-a-chip devices often integrate sensors or detection mechanisms for real-time analysis. This can include optical detection using fluorescence, absorbance, or scattering and electrical detection methods like impedance sensing or electrochemical detection [196]. Miniaturized detectors and imaging systems are commonly used to capture and analyze the signals generated by the analytes. Glass, silicon, ceramic, metal, and polymers are some common materials of construction used as a substrate for LOC devices. Deformable materials such as polydimethylsiloxane (PDMS), fluorocarbon, and cyclic olefin polymers are used to make micropumps and microvalves required for reagent addition [197].

### **2.4.1 Important applications of microfluidics**

Microfluidic devices play a crucial role in the field of biology and medical research. They have many applications, including gene manipulation, microscale genetic analysis, cell culture, biosensors, drug screening, point-of-care diagnostics, and biomaterial synthesis [198]. Specific applications of microfluidic devices include gene sequencing, protein manipulation, cell culture, microfluidic enzyme assays, and drug development. Microdevices offer the advantage of creating a precisely regulated and controllable environment for the cell culture and analysis [199]. Chip-scale enzymatic reactions have been developed to quantify analyte species, evaluate reaction kinetics, and assess inhibitors [200]. The utilization of microfluidics in drug discovery has proven beneficial in reducing time and costs at every process stage [201]. Because many microdevices are constructed from optically transparent materials, they are highly compatible with a variety of optical microscope techniques. A PDMS/glass hybrid microfluidic device has been used to perform high resolution fluorescence microscopy of a photonic crystal substrate. The PDMS layer provided the optical transparency required for the imaging.

The glass coverslip was used to facilitate high resolution oil immersive imaging, which is not feasible when only PDMS is used [190].

## 2.4.2 Photolithography

Photolithography is a widely used technique to create patterns on a suitable substrate, such as glass, silicon, or quartz, using a series of chemical processes [202]. The photolithography process consists of some basic steps: photoresist deposition on a substrate, a soft bake to evaporate the solvent, UV exposure with pattern alignment to initiate the polymerization of the photoresist on the substrate, a post-exposure bake to complete the polymerization, and developing to obtain the microstructures (**Figure 2.15**) [203, 204]. Two types of photoresists are available: positive and negative. In a positive photoresist, the UV-exposed areas are dissolved in the development stage while in a negative photoresist, the UV-exposed areas remain intact after development. SU-8, an epoxy-based negative photoresist, is extensively used in photolithography due to its low UV absorption and a high degree of crosslinking, enabling the design of thick structures with a good definition [205]. The spin coating speed and the viscosity of the photoresist determine the thickness of the photoresist on the substrate. The solvent in the photoresist evaporates during the soft bake step [204]. A photolithography mask is used to pattern specific features using the photoresist by enabling selective UV passage onto the substrate. The exposure time, energy, and post-exposure hard bake time are crucial to obtain the required features on the substrate. Minute features are enhanced through low exposure time and longer post-exposure bake. A shorter post-exposure bake is recommended for wider features because it could result in feature lifting off in the developer solution [206]. Some limitations of the photolithography process include high cost and limited control of surface properties [193].

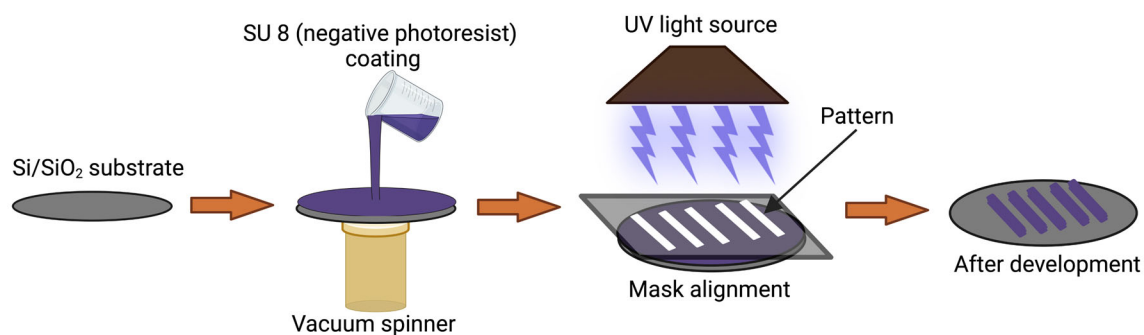


Figure 2.15. Photolithography process for SU-8 photoresist on a Si/SiO<sub>2</sub> substrate. Created with BioRender.com.

## 2.4.3 PDMS microdevices in bioenergy

Polydimethylsiloxane (PDMS) has many desirable properties, such as flexibility, biocompatibility, water impermeability, and optical transparency. Various microdevices have been created for use in bioenergy research. Transesterification of vegetable oils during biodiesel synthesis was carried out in PDMS microdevices with thermally stable

microchannels [207, 208]. Hybrid PDMS/glass microchambers, which are compatible with commercial microplate readers, have been used to screen the cultivation parameters and culture microalgae for biofuel production processes [209, 210]. Hydrothermal liquefaction of microalgae has also been carried out in PDMS microfluidic reactors [211]. PDMS chambers have also been used in miniature microbial fuel cells, artificial photosynthesis, and monitoring the performance of multiple fermentation microbes during bioethanol production [212-215].

# 3 DESIGN AND CONSTRUCTION OF A MICROFLUIDIC REACTOR FOR TIME-LAPSED IMAGING OF PRETREATMENT AND ENZYMATIC HYDROLYSIS OF LIGNOCELLULOSIC BIOMASS.

## 3.1 Introduction

Lignocellulosic biomass is a promising alternative to fossil fuels because of its abundance, high carbohydrate content, and potential to alleviate greenhouse gas emissions [75]. Among several conversion technologies, bioconversion using enzymes is attractive due to its ability to sustainably produce specific bioproducts [216]. However, the recalcitrance of lignocellulosic biomass is a major impediment to its enzymatic conversion [167]. Biomass recalcitrance is influenced greatly by the spatial distribution of lignin and hemicellulose within the cell wall however, there are also differences in lignin and hemicellulose distribution between plant tissues [11]. Thick-walled cell types in the vascular bundles, like the sclerenchyma, xylem, and phloem, have higher deposition of lignin and hemicellulose when compared to the thin-walled parenchyma cells [11, 12]. For example, in monocots like miscanthus, sugarcane, and maize, the pith, which is the central region of the stem, is abundant in parenchyma cells with higher cellulose content. The rind, which is the outer layer, has a high density of vascular bundles and a thick epidermis with higher lignin and hemicellulose content. [18, 70]. The variability in biomass recalcitrance due to the spatial heterogeneity of tissue types has been found to influence biomass degradability [14, 15]. Such tissue-specific evaluation of recalcitrance is crucial to design sustainable pretreatment methods or engineer crop cultivars for efficient biomass conversion [14]. However, these studies are extremely challenging to conduct given the complexity of the biomass structure [143, 181]. Despite several studies on the bulk characterization of fractionated tissues, which included compositional analysis and imaging of the pretreated samples, interpretation of tissue-level recalcitrance remains a challenge [14, 217].

Microscopy is a powerful tool for investigating biochemical spatial heterogeneity based on tissue and cell types and identifying the limiting factors of biomass deconstruction [164]. The most widely used imaging methods are confocal laser scanning microscopy (CLSM), fluorescence microscopy (FM), transmission electron microscopy (TEM), scanning electron microscopy (SEM), atomic force microscopy (AFM), coherent Anti-Stokes Raman scattering microscopy (CARS), X-ray computed tomography (CT), and confocal Raman microscopy (CRM) [12, 18, 164, 218]. CLSM has been particularly useful in elucidating cell wall modifications during biomass deconstruction [133]. Several researchers have utilized CLSM to visualize changes in biomass at different stages of pretreatment and/or enzymatic hydrolysis [187, 219, 220]. More specifically, spatial mapping of lignin autofluorescence and other cell wall components in the cell wall during pretreatment of lignocellulosic biomass has been utilized in previous studies [167, 176]. However, there are bottlenecks in conducting such imaging studies such as (i) the fragility of the pretreated biomass, which makes it extremely difficult to obtain sections thin enough for microscopy without extensive chemical infiltration for embedding, (ii)

the inability to observe the exact same sample at regular intervals when the deconstruction is carried out on bulk biomass, and (iii) the inability to obtain biochemical spatial information from ground biomass. Pretreatment and enzymatic hydrolysis of thin sections of whole biomass within the same device would enable time-lapsed imaging studies on biomass deconstruction and overcome these issues. For such microscale experiments, microfluidic devices developed using photolithographic techniques have been extremely useful in evaluating bioconversion processes [221].

The goal of this project was to design and construct a microfluidic reactor to demonstrate time-lapsed imaging of pretreatment and enzymatic hydrolysis of lignocellulosic biomass and localize specific glycans using monoclonal antibodies without the need to remove the samples from the device at any point in the process. The device was also designed to allow for sampling of the liquid during the process for analysis. In this study, we constructed this reactor and used it to compare the effect of dilute acid and dilute alkali pretreatment on corn stems using 1 M sulfuric acid and 62.5 mM sodium hydroxide, respectively, at 100 °C. The progress of the pretreatment reactions over time was monitored using confocal fluorescence microscopy by observing changes in cell wall lignin autofluorescence and arabinoxylan using immunolabelling with the LM11 antibody. Enzymatic deconstruction of the cell walls was also monitored using brightfield imaging and related to the composition of the liquid phase removed from the reactor. The device was used successfully to track changes in the same maize stem tissues throughout the experiments.

## **3.2 Materials and Methods**

### **3.2.1 SU-8 mold preparation using soft photolithography**

A 5-inch diameter silicon wafer (5" diameter and 375 μm, University Wafer, Inc) was cleaned with acetone and isopropyl alcohol, followed by dehydration on a hot plate at 160 °C for 5 min. Once cooled to room temperature, a 250 μm thick layer of MicroChem SU-8 100, a negative photoresist [204], was spin-coated on the silicon wafer at 1200 rpm using an H6-23 Laurell Spin Processor. The SU-8 coated wafer was hard-baked at 65 °C for 25 min and at 95 °C for 70 min. A mask was prepared by printing the reactor design on a plain paper transparency film. The wafer was exposed to UV light on an EVG 260 Mask Aligner with the mask. The exposed wafer was soft-baked at 65 °C for 1 min and at 95 °C for 16 min. Once cooled to room temperature, the wafer was immersed in the SU-8 developer solution (Kayaku Advanced Materials, Inc.) until it was developed completely. It took about 25-27 min to complete development.

### **3.2.2 Polydimethylsiloxane (PDMS) reactor prepared using the SU-8 100 mold**

The silicon wafer with the SU-8 100 mold was placed inside a plastic box. The PDMS was prepared by mixing 25 g of Sylgard 184 silicone elastomer base and 2.5 g of curing agent (10:1 ratio by weight) in a 50 mL disposable centrifuge tube. The mixture was then



poured onto the SU-8 100 mold and placed inside a desiccator for 24 hours. The edges of the cured PDMS reactor chamber were cut using a carbon surgical blade (Medblades Catalog No. 4-112). The PDMS reactor chamber was then peeled off the SU-8 100 mold. A 3 mm and 1 mm diameter opening were made in the PDMS chamber using suitable biopsy punches (Ted Pella Catalog No. 15110-30, 15110-10). In a separate 50 mL disposable centrifuge tube, PDMS was prepared by mixing 35 g of Sylgard 184 silicone elastomer base and 3.5 g of curing agent (10:1 ratio by weight). This mixture was poured into a 47 mm diameter polystyrene weighing dish (Fisherbrand Catalog No.02-202-101) and placed inside a desiccator for 24 hours. The thickness of this PDMS layer was about 5 mm. This PDMS layer was peeled off the polystyrene weighing dish. This layer was cut into multiple 25 mm square pieces using a carbon surgical blade (Medblades Catalog No. 4-112). A 20 mm diameter hole was cut out from each of the 25 mm square PDMS piece using a carbon surgical blade (Medblades Catalog No. 4-112). The PDMS layer with the 20 mm diameter hole was adhered to the PDMS reactor chamber using super glue (Gorilla Catalog No. 7501201) and allowed to dry for 2 min. The volume of the PDMS reactor set up was approximately 1571  $\mu\text{L}$ .

### **3.2.3 Sectioning samples using a cryomicrotome**

Corn stems used in these studies were harvested in October 2016 in Houghton, Michigan, and dried at room temperature. Stem cross sections were prepared using a Thermo Scientific Microm HM550 P cryomicrotome set to  $-30\text{ }^{\circ}\text{C}$ . Once the desired temperature was reached, a 1 cm long section of corn stem internode was embedded in an OCT compound (Tissue Tek Product Code. 4583) by placing the sample on a suitable sample holding chuck inside the cryomicrotome and adding the OCT compound onto the sample until the sample was completely covered. When the sample and the OCT compound were frozen, the chuck was placed on the holder and 60  $\mu\text{m}$  thick sections were made using a 0.25 mm microtome blade (CellEdge Catalog No. 27266). The sectioned corn stem samples (approximately 0.23 mg each) were mounted individually on a 25 mm diameter cover glass (Electron Microscopy Sciences Catalog No. 721195). The glass coverslip containing the 60  $\mu\text{m}$  thick corn stem sample was adhered to the PDMS reactor chamber using super glue (Gorilla Catalog No. 7501201) and allowed to dry for 2 min. To remove the water soluble TissueTek OCT compound, the samples and the coverslip were rinsed with 200  $\mu\text{L}$  deionized water using a pipette and allowed to dry before pretreatment. The outer side of the coverslip was wiped with 90% ethanol to remove any dust particles.

### **3.2.4 Pretreatment experiments with time-lapsed imaging**

Dilute acid and alkali pretreatment was carried out on samples at  $100\text{ }^{\circ}\text{C}$  in a gravity oven (Fisherbrand Catalog No.151030521) using 400  $\mu\text{L}$  of 1 M sulfuric acid or 62.5 mM sodium hydroxide ( $\sim 0.05\%$  solids loading), respectively. The pretreatment experiments were carried out for 45 min while performing confocal laser scanning microscopy (CLSM) at 15 min intervals. Aliquots of the pretreatment supernatant (150  $\mu\text{L}$ ) were removed every 15 min using a 1 cc insulin syringe with a detachable needle (Fisher Scientific Catalog No. 14-820-28). The remaining pretreatment supernatant was discarded. The samples were then washed three times with 200  $\mu\text{L}$  of deionized water to stop the reaction before conducting confocal laser scanning microscopy (CLSM)

imaging. After CLSM imaging, fresh reagents were added to the reactor for the next stage in the pretreatment.

### **3.2.5 Enzymatic hydrolysis with time-lapsed imaging**

Following imaging, enzymatic hydrolysis (final working volume of 400  $\mu$ L) was carried out on the pretreated samples at 50 °C in a static incubator for 72 hours. Novozymes 22257 cellulase and Novozymes 22244 hemicellulase (Novozymes, Franklinton, NC, USA) were loaded at 1 mg protein/g solids, at a ratio of 70% cellulase and 30% hemicellulase. The protein content of the enzymes was previously determined by first desalting using a disposable desalting column (Disposable PD-10 Desalting columns, Cytiva, VWR Catalog. No. 95017-001) and analyzing the protein content using the Pierce™ BCA Protein Assay Kit (Thermo Fisher Scientific Catalog No. 23227). CLSM imaging was carried out on the hydrolyzed samples after 15 and 30 min, and 4, 8, 12, 24, 48 and 72 hours. The hydrolysate was removed at each interval and saved for analysis (as described in “End-product analysis for pretreatment supernatant and hydrolysates”). The biomass was then washed three times with ~200  $\mu$ L deionized water before conducting CLSM. After CLSM imaging, fresh reagents were added to the reactor for the next stage in enzymatic hydrolysis.

### **3.2.6 Immunolocalization of xylan**

Immunolocalization of arabinoxylan was carried out on four different 60  $\mu$ m thick corn stem sections that were untreated and dilute acid pretreated for 15, 30, and 45 min at 100 °C. While still inside the imaging reactor, the samples were washed three times with phosphate-buffered saline (PBS, pH 7.4) and blocked with PBS containing 1% bovine serum albumin (BSA) for 2 hours to avoid nonspecific binding. Then samples were incubated overnight at 4 °C with an arabinoxylan-specific monoclonal antibody LM11 diluted 1:10 in PBS [222]. After antibody binding, the samples were washed three times with PBS and incubated with Alexa Fluor™ 568, Goat anti-Rat IgG Cross-Adsorbed Secondary Antibody diluted 1:100 in PBS (Invitrogen Catalog No. A11077) for 1 hr. Then, the samples were washed three times with PBS.

### **3.2.7 Sample preparation for pretreated biomass composition analysis**

Due to the extremely low biomass weight (0.23 mg), to obtain sufficient pretreated biomass for composition analysis, ~100-150 corn stem sections (60  $\mu$ m thickness) were prepared on the cryomicrotome (as described in “Sectioning samples using a cryomicrotome”). These biomass sections were pretreated for 45 minutes at 100 °C in a gravity oven (Fisherbrand Catalog No.151030521) in separate 20 mL scintillation vials using either 5 mL of 1 M sulfuric acid or 62.5 mM NaOH (~0.05% solids loading). The pretreated solids and slurry were transferred to 50 mL centrifuge tubes and centrifuged at 4000 rpm for 30 min at 4 °C in a bench-top laboratory scale centrifuge (Eppendorf 5804R). The pretreatment supernatant was discarded, and the remaining solids were washed three times with deionized water and dried overnight in an aluminum weighing dish at room temperature. The dried solids were roughly ground using a mortar and

pestle. The untreated and pretreated biomass were stored at room temperature in Ziploc bags until they were shipped for composition analysis.

### **3.2.8 Acetyl bromide soluble lignin (ABSL) analysis**

The untreated and pretreated biomass were separately extracted to leave the alcohol insoluble residue and then evaluated for acetyl bromide soluble lignin (ABSL) content according to the method described previously [223].

### **3.2.9 Matrix polysaccharide analysis**

About 2 mg of AIR was hydrolyzed with 2 M trifluoroacetic acid for 1.5 hours at 121 °C. The samples were evaporated to remove the trifluoroacetic acid and rinsed four times with isopropyl alcohol and resuspended in deionized water. The liquid was evaluated for hemicellulosic and pectic sugar content using HPLC and the solid residue was analyzed for crystalline cellulose using the previously described method (Anthrone colorimetric assay) [224].

### **3.2.10 End-product analysis for pretreatment supernatant and hydrolysates**

Pretreatment supernatant and hydrolysates (~150 µL) were collected at each time point of imaging for end-product analysis. The pretreatment supernatant and the hydrolysates were diluted with 1350 µL deionized water (10x dilution) and then filtered using a 0.2 µm PES syringe filter (Agilent Catalog No. 5191-5922). Glucose, xylose, and other end-products were evaluated using high-performance liquid chromatography (HPLC) through an Aminex HPX-87H column (BioRad) and quantified using refractive index detection (RID) as described previously [65].

### **3.2.11 Confocal microscopy, image processing, and data analysis**

Confocal laser scanning microscopy (CLSM) of pretreated and enzymatically hydrolyzed samples was carried out on an Olympus FV1000 confocal microscope, using an excitation wavelength of 405 nm with a DAPI bandpass filter (480-550 nm) at 23% laser power and 1024 x1024 pixel resolution. CLSM imaging of the antibody-labeled samples was conducted using a 559 nm laser with emission at 580-620 nm. A vascular bundle in the rind region and the pith region were imaged for each time interval. For each run of CLSM imaging, 60 slices were obtained. Brightfield images were also recorded for samples following enzymatic hydrolysis, as the autofluorescence signals were very low following pretreatment. Images were processed with Fiji (ImageJ) software [176, 187]. The image stacks comprising 60 slices were converted to average-intensity Z-projection images. The fluorescence intensity data were obtained for parenchyma, sclerenchyma, metaxylem, and protoxylem regions by adding a line ROI (region of interest) across the respective cell walls.

### 3.2.12 Calculations

Enzymatic hydrolysis conversions of glucose and xylose were calculated as described previously [216]

$$\begin{aligned} & \text{Glucose conversion (\% of theoretical)} \\ &= \frac{\text{glucose concentration } \left(\frac{g}{L}\right) * \text{hydrolysate volume (L)} * 0.9}{\text{polysaccharides in the untreated dry biomass (g)}} \\ & * 100\% \end{aligned}$$

$$\begin{aligned} & \text{Xylose conversion (\% of theoretical)} \\ &= \frac{\text{xylose concentration } \left(\frac{g}{L}\right) * \text{hydrolysate volume (L)} * 0.88}{\text{polysaccharides in the untreated dry biomass (g)}} \\ & * 100\% \end{aligned}$$

Where 0.9 and 0.88 are the conversion factors for glucose and xylose, respectively.

## 3.3 Results and Discussion

The microimaging reactor consisted of a PDMS reaction chamber containing a 60  $\mu\text{m}$  thick corn stem section on a glass coverslip, which was adhered to the PDMS chamber using super glue (**Figure 3.1A**). The microimaging reactor was designed with openings for reagent addition/removal and a vent to prevent pressure buildup (**Figure 3.1A**). The arrangement was designed to work with an inverted fluorescence microscope. The reactor operating conditions are constrained to ambient pressure and a maximum temperature of 100  $^{\circ}\text{C}$ , and once contained in the reactor, the solid biomass is inaccessible for further characterization.

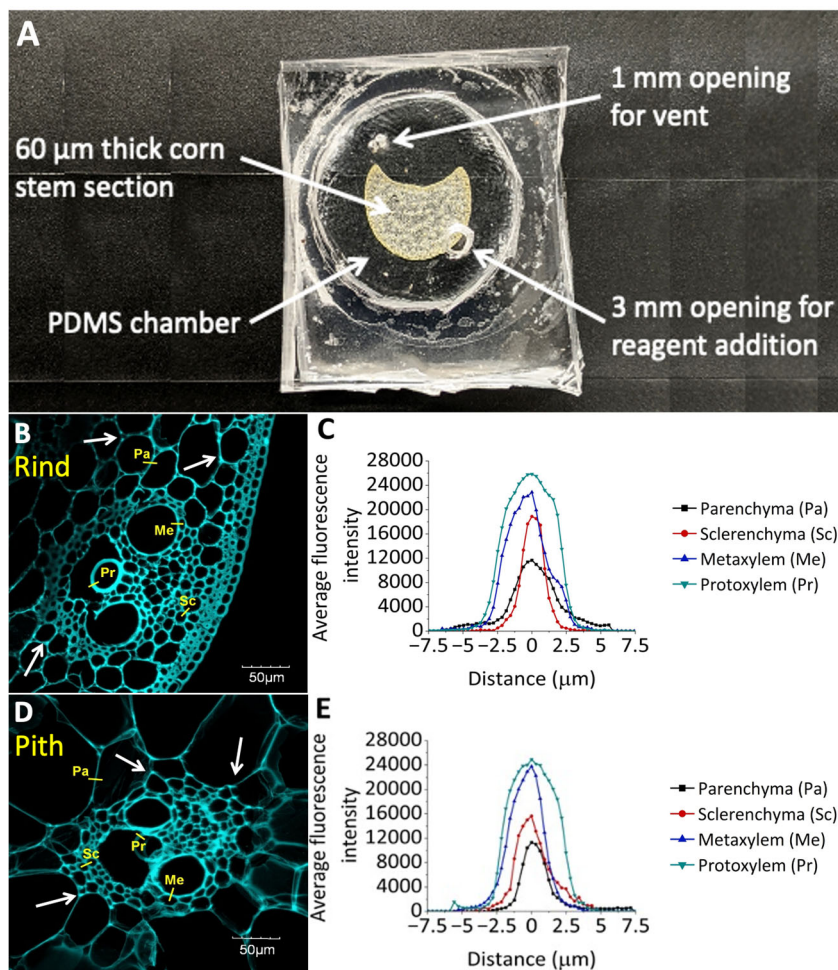


Figure 3.1. A) Microfluidic imaging reactor containing an untreated corn stem sample. Vascular bundles in the B) rind and D) pith region of a 60  $\mu\text{m}$  thick untreated corn stem show strong lignin autofluorescence, with greatest intensity near the cell corners throughout the cross section (white arrows). The initial fluorescence intensities increased gradually for parenchyma (Pa), sclerenchyma (Sc), metaxylem (Me), and protoxylem (Pr) cell walls in the C) rind and E) pith regions. The excitation wavelength was 405 nm with a DAPI emission bandpass filter (480-550 nm).

### 3.3.1 Initial autofluorescence signals were higher for the cell types near the vascular bundles than the parenchyma cells

In this study, we compared the effect of dilute acid and dilute alkali pretreatment on 60  $\mu\text{m}$  thick corn stem sections using 1 M sulfuric acid or 62.5 mM sodium hydroxide, respectively, at 100  $^{\circ}\text{C}$  by analyzing the changes in lignin autohydrolysis using CLSM. The pretreatment was carried out at a relatively low severity to prevent complete degradation prior to enzymatic hydrolysis, as stem sections were comparatively thin. Lignin is a complex polymer that exhibits autofluorescence in the UV and visible regions [133]. The relative changes in autofluorescence signals during pretreatment of the biomass sections were used to map lignin modifications in the cell wall. Although it is not extremely accurate to quantify the absolute lignin using autofluorescence signals,

imaging the same sample under the same conditions gave us a comparison of the relative changes in lignin during the pretreatment [174]. The CLSM images of the untreated corn stem sections showed noticeably higher fluorescence signals in the cell corners (**Figure 3.1B, 3.1D**), which is expected as higher fluorescence intensities in the middle lamella and cell corners compared to the secondary cell wall have previously been inferred to indicate greater lignification in those areas [133]. Of the four cell types evaluated, the fluorescence intensity was the lowest for parenchyma cells and gradually increased for sclerenchyma, metaxylem, and protoxylem cells (**Figure 3.1C, 3.1E**). Previous studies have found that lignin content varies between tissue types based on their functionality during plant growth and development [46, 54]. The cell types in and around the vascular bundles, such as the sclerenchyma, metaxylem, and protoxylem, possess highly lignified secondary cell walls [54, 177], which would be a plausible explanation for the higher fluorescence intensities for these cell types in our results. Of the cell types, only the sclerenchyma showed a large difference in fluorescence intensity between the rind and pith regions, with greater fluorescence in the rind (**Figure 3.1C, 3.1E**). Based on a previous study, the rind region typically has a higher lignin content compared to the pith region [54]. The sclerenchyma cell walls have also been reported to be thicker in the rind region, with higher lignin content when compared to the same in the pith region, which is similar to our fluorescence intensity results [225].

### **3.3.2 Dilute acid pretreatment resulted in a greater decline in fluorescence in the parenchyma cells than in the vascular bundles**

A gradual loss of fluorescence signals during dilute acid pretreatment was observed after 15 min, 30 min, and 45 min of pretreatment in both the rind and the pith region. Based on the CLSM images, the fluorescence intensities were lower for the parenchyma cells than the cell types around the vascular bundle for both the rind and pith regions (**Figure 3.2**). However, the brightfield images confirm that there is no significant alteration in the cell structure for all the cell types in both the rind and the pith regions (**Figure 9.1**). The autofluorescence seems to be distributed uniformly in the pretreated samples (**Figure 3.2B-2D, 3.2F-2G**) as opposed to a higher intensity at the cell corners in the untreated sample (**Figure 3.2A, 3.2E**). Based on the fluorescence intensity profiles of the cell types in the rind and the pith region, the overall loss of fluorescence signals was greater for all the cell types in the rind region than the pith region, except for the protoxylem, for which it was greater in the pith region (**Figure 3.3D, 3.3H**). Although the different cell types initially showed a range in autofluorescence, with the protoxylem having the greatest intensity, the fluorescence intensity was rapidly lost during the first 15 min of dilute acid pretreatment, even in the highly lignified middle lamella, with a slower loss of fluorescence signals over subsequent intervals (**Figure 3.3**). The loss of lignin autofluorescence signals for all the cell types in the CLSM images (**Figure 3.2**) could result from the redistribution of lignin during the dilute acid pretreatment [72]. Previous studies on miscanthus have reported a similar change in lignin autofluorescence, in addition to a structural loosening and separation of individual cells after 15 and 30 min of dilute acid pretreatment at 160 °C [70, 71]. In contrast, we did not observe any major structural modification (**Figure 3.2E, 3.2J**), which is likely because our pretreatment

temperature (100 °C) is below the glass transition temperature of lignin (120 - 200 °C) [70]. The uniform autofluorescence distribution in the pretreated samples is likely due to the modification of the lignin post-pretreatment [226]. A previous study on dilute acid pretreatment of poplar, miscanthus, and wheat straw reported a similar uniform autofluorescence distribution compared to a higher intensity at the cell corners before the pretreatment [218]. The greater loss of fluorescence signals in the protoxylem cell walls could be because these are the most lignified tissue types compared to the sclerenchyma and parenchyma cell walls [15, 225]. Previous studies have demonstrated that, for grass-based biomass, the xylem vessels are the first tissues to be lignified during the developmental stages and are likely the most resistant to degradation [227, 228]. The lower residual fluorescence after 45 min pretreatment for the parenchyma cells than the other tissue types could be attributed to the lower lignin content in the thin-walled parenchyma cells, in which the lignin-hemicellulose linkages are easier to hydrolyze [46]. Several studies have reported lignin coalescence on the cell wall surface after dilute acid pretreatment at temperatures higher than the glass transition temperature of lignin (120 - 200 °C), when observed using scanning electron microscopy [139, 218, 229]. A few studies have shown a similar lignin globule formation on the cell wall after lignin autohydrolysis using CLSM [139]. Such lignin droplet formation was not evident in our results, which is likely because the pretreatment temperature was below the glass transition temperature of lignin (120 - 200 °C), at which the lignin was only modified but not redistributed. The origin of lignin autofluorescence has been attributed to the agglomeration of carbonyl groups, the composition of various monolignols, and the cross-linkages between lignin and hemicellulose [173]. The changes in autofluorescence during the dilute acid pretreatment could be due to several reasons like modification of bonds between the monolignols, alteration of linkages between hemicellulose and lignin, and redistribution of lignin around cellulose microfibrils [230].

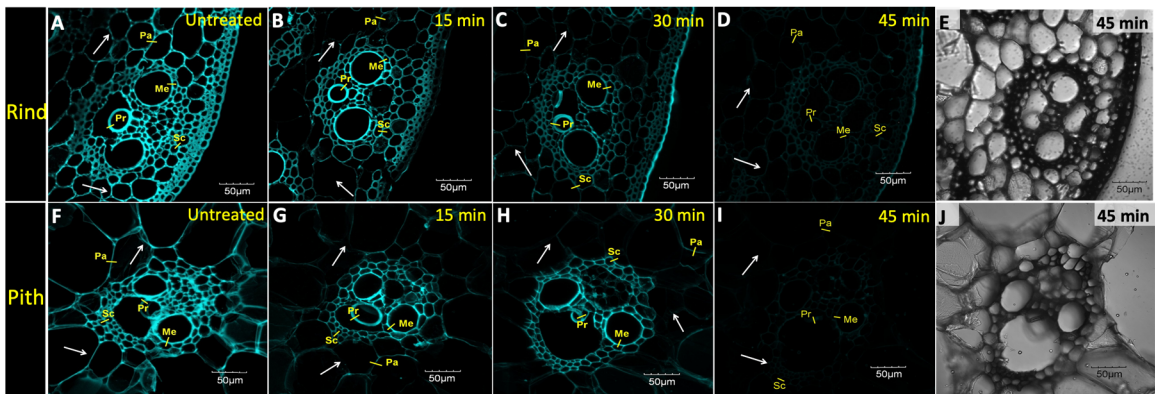


**Figure 3.2.** Vascular bundles in the rind (A-D) and pith (F-I) regions exhibited a gradual loss of fluorescence intensity after dilute acid pretreatment for 15 min (B, G), 30 min (C, H), and 45 min (D, I). The different cell types, including parenchyma (Pa), sclerenchyma (Sc), metaxylem (Me), and protoxylem (Pr) were selected as regions of interest (ROI) to quantify changes in lignin autofluorescence. Parenchyma cell walls have lower lignin autofluorescence fluorescence than the other cell types at all pretreatment stages (white arrows). (E, J) No significant structural changes occurred for all the cell types in both the rind and the pith regions after 45 min (brightfield images).

Dilute acid pretreatment was carried out on a 60  $\mu\text{m}$  thick corn stem section using 1 M sulfuric acid at 100  $^{\circ}\text{C}$ . The excitation wavelength was 405 nm with a DAPI emission bandpass filter (480-550 nm).

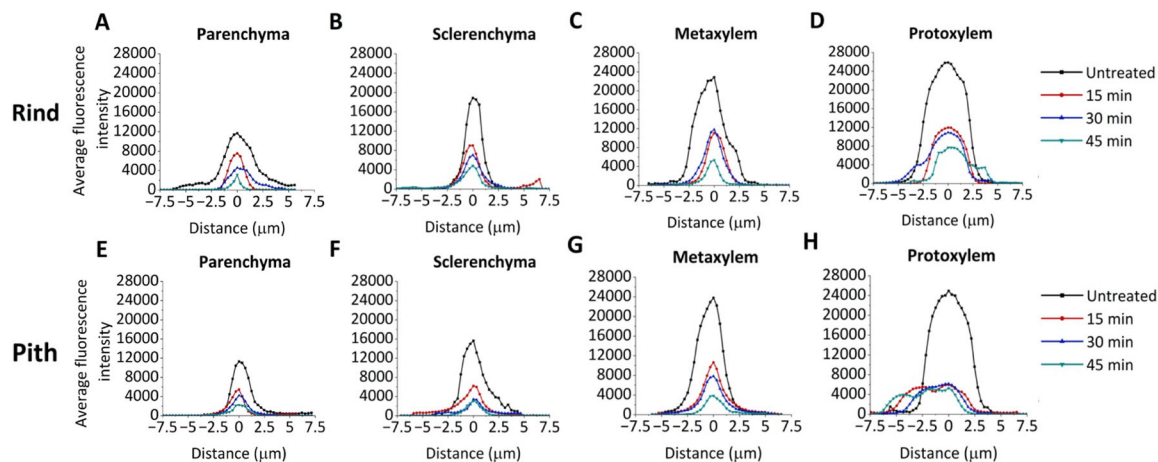


**Figure 3.3.** Different cell types in the rind (A-D) and pith (E-H) showed variation in initial fluorescence followed by rapid loss of fluorescence signals during the first 15 min of dilute acid pretreatment. Dilute acid pretreatment was carried out on a 60  $\mu\text{m}$  thick corn stem section using 1 M sulfuric acid at 100  $^{\circ}\text{C}$ . The excitation wavelength was 405 nm with a DAPI emission bandpass filter (480-550 nm).

### 3.3.3 Progressive loss of fluorescence signals and swelling occurred during dilute alkali pretreatment

Dilute alkali pretreatment was carried out on 60  $\mu\text{m}$  thick corn stem sections using 62.5 mM sodium hydroxide at 100  $^{\circ}\text{C}$ . Similar to dilute acid pretreatment, there was a gradual loss of fluorescence signal after 15 min, 30 min, and 45 min of dilute alkali pretreatment for all the cell types in the rind and the pith region (**Figure 3.4**). Unlike dilute acid pretreatment, during the first 15 min of dilute alkali pretreatment, the loss of fluorescence signals was lower in the thick cell walls, like the protoxylem, when compared to the parenchyma cells (**Figure 3.4**). In addition to the loss of fluorescence signals, the cell walls showed a swelling effect over time for both the rind and pith regions (**Figure 3.4, 3.4J, Figure 9.2**). All cells increased in thickness by  $\sim 2\text{-}4$   $\mu\text{m}$  following 45 minutes of dilute alkali pretreatment (**Figure 3.4I, 3.4J**). This could be due to the solubilization of lignin under the action of the sodium hydroxide [75, 231]. A previous study on alkali pretreatment of poplar using 2% sodium hydroxide under light microscopy showed a similar increase in cell wall thickness for 30 min, 60 min, and 3 hours of pretreatment at 121  $^{\circ}\text{C}$  [132]. The swelling effect of alkali pretreatment increases the accessible surface area of lignocellulosic biomass, thereby enabling higher sugar release during enzymatic hydrolysis [232].



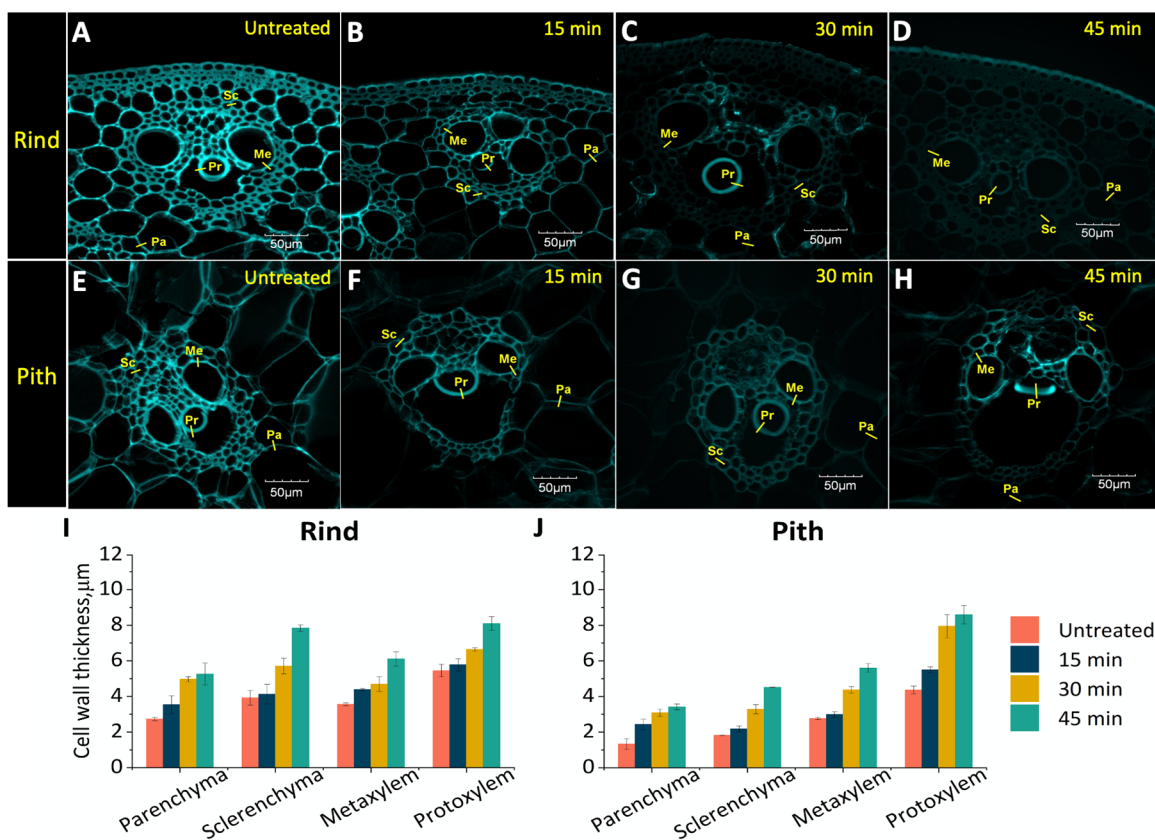


**Figure 3.4.** The rind (A-D) and pith (E-H) regions showed a gradual loss of fluorescence signals after 15 min (B, F), 30 min (C, G) and 45 min (D, H) of dilute alkali pretreatment with 62.5 mM sodium hydroxide at 100°C. The different cell types, including parenchyma (Pa), sclerenchyma (Sc), metaxylem (Me), and protoxylem (Pr) were selected as regions of interest (ROI) to quantify changes in lignin autofluorescence. The excitation wavelength was 405 nm with a DAPI emission bandpass filter (480-550 nm). Cell wall thickness (I, J) increased for all cell types in both the rind and the pith region following alkaline pretreatment. Values for all subfigures are reported as mean  $\pm$  S.D,  $n=3$ .

### 3.3.4 Composition of the residual biomass and the pretreatment supernatant conform to the CLSM results

Composition analysis was performed on the untreated and the residual biomass after 45 min of dilute acid and dilute alkali pretreatment to determine the acetyl bromide soluble lignin (ABSL) and other polysaccharides (Table 9.1-1). Acetyl bromide soluble lignin (ABSL) estimation has been reported to be influenced by the heterogeneity of lignin and by the xylan degradation. Nevertheless, ABSL is a widely used proxy for lignin content to evaluate pretreatment methods [233]. The ABSL composition decreased from 21% to 16% for the dilute alkali pretreated sample, while the dilute acid pretreated sample showed no significant change (Figure 3.5I). The xylose and arabinose content was reduced to a greater extent during dilute acid pretreatment compared to alkali pretreatment (Figure 3.5J, 3.5K). There was almost no change in xylose or arabinose composition following dilute alkali pretreatment, from 32% (untreated) to 31%, and 4% (untreated) to 5%, respectively (Figure 3.5J, 3.5K).

The pretreatment supernatant aliquots from dilute acid and dilute alkali pretreatment at different stages were analyzed using HPLC for xylose and glucose release during pretreatment. The total glucose and cellobiose released during the pretreatment were negligible (**Table 9.1-2**). Although the total xylose conversion was greater during dilute acid pretreatment compared to alkali pretreatment, xylose began and continued to be released later in the pretreatment (30 min and 45 min) compared to alkali, where all the xylose was released in the first 15 min of pretreatment (**Figure 3.5L**). During dilute acid pretreatment, hemicellulose is hydrolyzed to arabinose and xylose, which could explain the decrease in xylose and arabinose in the residual biomass and higher xylose release in the pretreatment supernatant in our results [234]. A comparison of dilute acid pretreatment of sorghum at different temperatures and acid concentrations showed a xylose conversion of approximately 30% of theoretical for 100 °C and 1 M sulfuric acid [69]. In dilute alkali pretreatment, the disruption of ester linkages between lignin and xylan results in lignin removal, which is consistent with our results [75]. A previous study on alkali pretreatment with sodium hydroxide for wheat straw reported that at temperatures higher than 90 °C, dilute alkali pretreatment showed very low xylose release, which agrees with our result [235].

### **3.3.5 Antibody labeling with arabinoxylan specific LM11 indicated changes in xylan during dilute acid pretreatment.**

Immunolabelling and imaging of biomass sections in previous studies have been carried out on very thin biomass sections, < 2 µm, which are generally obtained through a series of chemical infiltration steps followed by embedding in suitable resin or wax and then sectioned on an ultramicrotome [181, 182, 187, 236]. To avoid handling and damaging fragile pretreated and hydrolyzed samples, we wanted to determine whether it was possible to immunolabel our comparatively thick (60 µm) corn stem sections within the imaging reactor without performing any chemical infiltrations or subsequent sectioning. Similar to lignin autofluorescence, changes in xylan distribution during dilute acid pretreatment were evaluated using immunofluorescence localization of the arabinoxylan-specific antibody LM11. Unlike pretreatment and enzymatic hydrolysis, it is not feasible to conduct time-lapsed analyses of labeled materials. Antibody labeling was carried out on four different pretreated corn stem sections (untreated and pretreated with 1M sulfuric acid at 100 °C for 15 min, 30 min, and 45 min) using LM11 conjugated with an Alexa Fluor 568 labeled secondary antibody, chosen so as not to overlap with lignin autofluorescence.

Based on the CLSM results, the untreated corn stem section showed that LM11 bonded with all the cell types (parenchyma and vascular cells) (**Figure 3.5A, 3.5E**). For the pretreated corn stem sections, the fluorescence intensities decline gradually with time for the 15 min, 30 min, and 45 min dilute acid pretreated biomass (**Figure 3.5, Figure 9.3, Figure 9.4**). The epitope for LM11 can bind to both substituted and unsubstituted xylan when compared with other antibodies like LM10 and LM28, which bind only to unsubstituted xylans [236]. Due to this reason, LM11 has been used for the broad detection of xylans in grasses [181]. Previous studies have reported a similar LM11 binding to all cell types in both the vascular bundle and the parenchyma cell walls for

sugarcane, hybrid aspen, and corn stalk [181, 182, 236]. Similar studies using LM11 to evaluate dilute acid pretreatment reported a similar loss of fluorescence signals, which is due to the acid hydrolysis of xylan during the dilute acid pretreatment [229, 236]. These results demonstrate that the imaging reactor can be utilized for monoclonal antibody labeling to localize glycan epitopes.

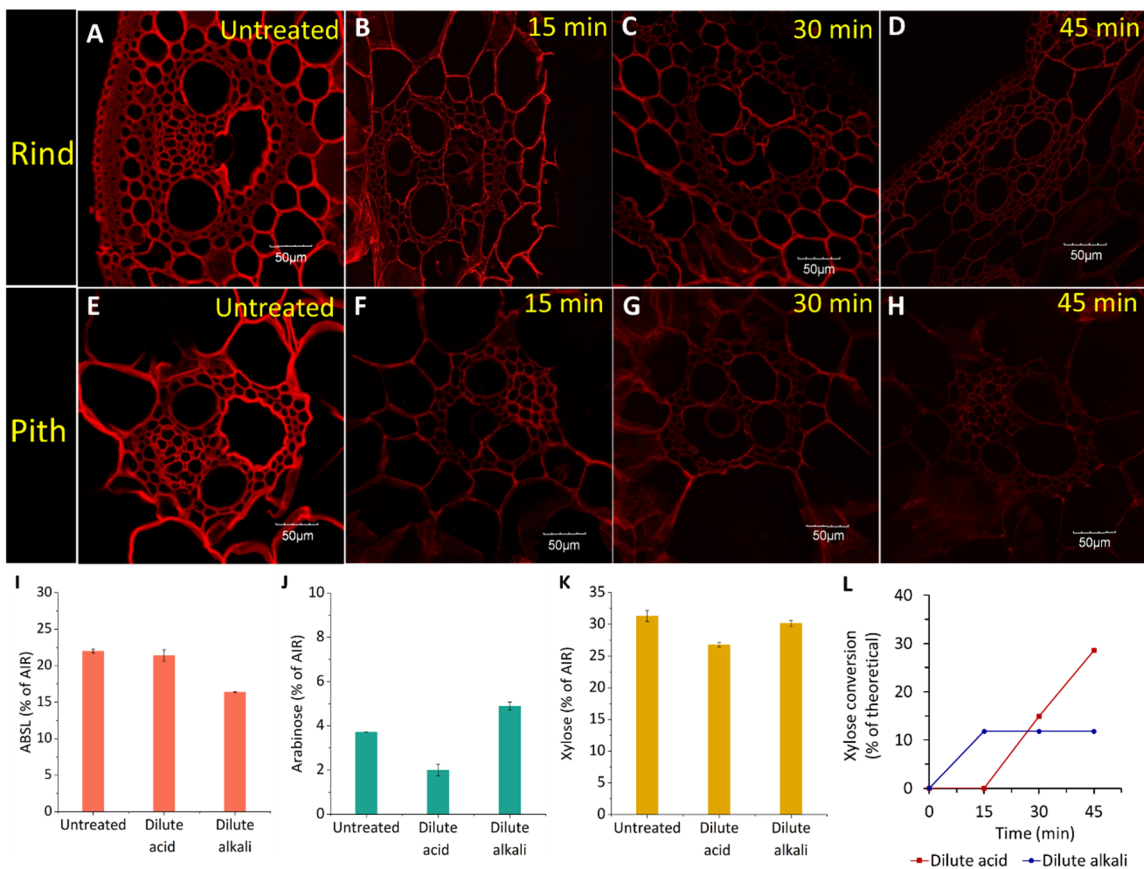


**Figure 3.5. (A-D) CLSM images of a vascular bundle of corn stem in the rind region with immunolabeling for arabinoxylan using LM11 monoclonal antibody and Alexa Fluor 568 secondary antibody for untreated, 15 min, 30 min, and 45 min dilute acid pretreated samples. (E-F) CLSM images of a vascular bundle in the pith region with immunolabeling for arabinoxylan using LM11 monoclonal antibody and Alexa Fluor 568 secondary antibody for untreated, 15 min, 30 min, and 45 min dilute acid pretreated samples. The samples were excited using a 559 nm laser and with emission at 580-620 nm. (I) Acetyl bromide soluble lignin (ABSL) decreased for the dilute alkali pretreated sample due to lignin solubilization (J&K) Arabinose and xylose composition decreased for the dilute acid pretreated sample due to hemicellulose hydrolysis (L) Cumulative xylose release during dilute acid pretreatment was higher than during dilute alkali pretreatment. Values for all subfigures are reported as mean  $\pm$  S.D, n=2.**

### 3.3.6 Protoxylem cell walls were the slowest to hydrolyze during enzymatic hydrolysis of the acid and alkali pretreated samples

To evaluate the feasibility of conducting enzymatic hydrolysis on samples that had been previously pretreated in the imaging reactor, the same samples used for the evaluation of lignin autofluorescence were subjected to 48-hr enzymatic hydrolysis at an enzyme loading of 1 mg protein/g solids, without being removed from the reactor. During initial trials with 72-hr enzymatic hydrolysis and higher enzyme loadings (10, 18, and 23 mg protein/g solids), biomass deconstruction was too rapid to evaluate, so the low protein loading was chosen to allow for a better comparison of degradation of the different tissue types.

During enzymatic hydrolysis, the alkali-pretreated samples showed that the swelling effect enabled more rapid hydrolysis than the dilute acid-pretreated samples (**Figure 3.6**). For the acid-pretreated sample, the parenchyma cell wall structure remained intact until 12 hours of enzymatic hydrolysis (**Figure 3.6E, 3.6L**), and the vascular tissues hydrolyzed much more slowly (**Figure 3.6**). For the alkali-pretreated sample, however, the thin-walled parenchyma cell walls disintegrated completely after 4 hours of enzymatic hydrolysis (**Figure 3.6P, 3.6W**) while the vascular bundle tissues remained intact after 24 hours (**Figure 3.6S, 3.6Z**). For both samples, the corn stem section was disintegrated completely after 48 hours of enzymatic hydrolysis except for a few protoxylem cell walls that were adhered to the coverslip (**Figure 3.6G, 3.6T**). At this point, there was hardly any difference between the rind and the pith region or between the two pretreatments. The progress of enzymatic hydrolysis appears related to the initial lignin autofluorescence data of the untreated corn stem sections, in which the protoxylem cell walls had the highest fluorescence intensity (**Figure 3.1C, 3.1E**). A previous study on real-time imaging of enzymatic hydrolysis of alkali-pretreated sorghum straw showed a similar trend of faster hydrolysis of the parenchyma cell walls than the cell walls in the vascular bundle [237].

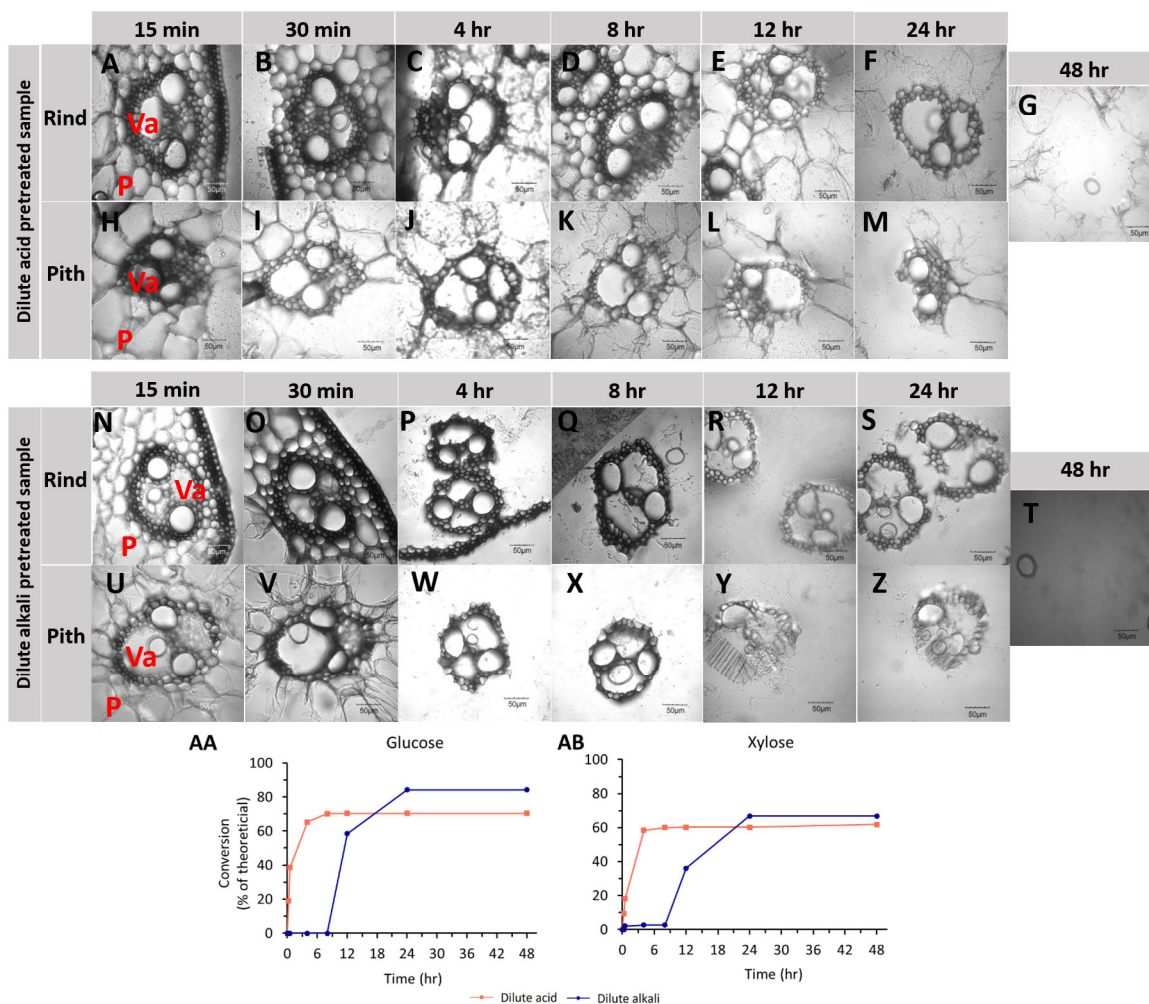


**Figure 3.6.** Brightfield images of corn stem samples during enzymatic hydrolysis after dilute acid (A-M) and alkali (N-Z) pretreatment. The parenchyma (Pa) cell walls hydrolyzed more readily than the cell walls in the vascular bundle (Va). After 48 hr (G, T) it became impossible to distinguish cells derived from the pith and rind. Glucose (AA) and xylose (AB) conversion during enzymatic hydrolysis of acid and alkali pretreated samples. Values for all subfigures are reported as mean  $\pm$  S.D, n=2. The error bars are smaller than the symbols for most of the data points. The conversions were calculated on an untreated, dry biomass basis.

The hydrolysates were also analyzed using an HPLC for sugar release at each time point. The glucose conversion was approximately 14% lower for the acid-pretreated sample than for the alkali-pretreated sample (**Figure 3.6AA**). The xylose conversion was 5% lower for the acid pretreated sample than the alkali-pretreated sample (**Figure 3.6AB**). However, it should be noted that for acid pretreatment, a significant xylose conversion (29%) occurred during the pretreatment (**Figure 3.5L**), which led to an overall higher xylose release. Similarly, previous studies that have compared acid and alkali pretreatment for corn stalk and sugar cane bagasse have reported higher glucose yield during saccharification of alkali pretreated biomass than acid-pretreated biomass [238]. Moreover, a decrease in fluorescence intensity during pretreatment has shown a strong

correlation to glucose release during enzymatic hydrolysis for wheat straw, miscanthus, and poplar samples, which is consistent with our findings [173].

### **3.4 Conclusion**

Pretreatment and enzymatic hydrolysis of a thin corn stem section were visualized through CLSM using the microfluidic imaging reactor. The parenchyma cells were more susceptible to degradation than the vascular bundles during both acid and alkali pretreatment. The protoxylem cell walls were the most resistant, remaining intact after 48 hours of enzymatic hydrolysis. The compatibility of the reactor with antibody labeling was verified through arabinoxylan localization using LM11. It indicated a uniform removal of hemicellulose for all cell types following dilute acid pretreatment. In spite of the pressure, temperature, and biomass accessibility constraints, the reactor is able to provide valuable insights into tissue-specific degradation during bioenergy production.

### **3.5 Funding**

This material is based upon work supported by the Great Lakes Bioenergy Research Center, U.S. Department of Energy, Office of Science, Office of Biological and Environmental Research under Award Numbers DE-SC0018409 and DE-FC02-07ER64494.

### **3.6 Acknowledgments**

We gratefully acknowledge Novozymes for generously providing the enzymes used during enzymatic hydrolysis. We thank R. Johnson and the GLBRC Biomass Analytical Facility for biomass composition analysis; M. McGee and the GLBRC Metabolomics Core Facility for HPLC analysis of pretreatment supernatant and hydrolysates. We thank Michigan Technological University's Applied Chemical and Morphological Analysis Laboratory and Microfabrication Facility for providing the equipment required to complete parts of this work.

## **4 WILL PITH SOLIDNESS IN WHEAT STRAW INCREASE SUGAR YIELDS DURING ENZYMATIC HYDROLYSIS?**

### **4.1 Background**

Biofuels obtained from lignocellulosic feedstocks have enormous potential to replace petroleum-based fuels and mitigate GHG emissions [239]. In particular, grasses like miscanthus, giant reed, switchgrass, corn stover, sugarcane, sorghum, etc., have the potential for high biomass yields with minimal inputs of nutrients and water [68, 240, 241]. However, the inherent biomass recalcitrance, which depends on the biomass structure and composition and varies between species and tissues within the same plant, is the major hindrance to biomass digestibility [242]. In previous tissue-specific evaluations of herbaceous feedstocks like corn stalks, sorghum, and sugarcane, the pith region, with numerous thin-walled parenchyma cells, was more susceptible to enzymatic hydrolysis in contrast to the more resistant rind region with a high density of vascular tissues like sclerenchyma, phloem, and xylem that have thicker secondary cell walls [18, 70, 181, 243]. In addition to being more digestible, the pith parenchyma cells in grass stems act as storage reservoirs for carbohydrates in the form of sugars, such as sucrose, or starch [244-248] that act as a reserve to sustain the plant during the growth phase and extreme weather conditions [249, 250]. These sugars also represent more digestible substrates for bioenergy production.

Modifying the pith parenchyma cells to improve biofuel production has been studied previously through different approaches. Yang et al. identified a transcriptional regulator from poplar, PtrWRKY19, which is responsible for downregulating secondary cell wall formation in the pith parenchyma cells. Overexpression of PtrWRKY19 resulted in a significant increase in pith cross sectional area accompanied by reduced lignin biosynthesis [251]. In switchgrass, targeted overexpression of miR156, a regulatory microRNA involved in the transition from growth phase to flowering phase, has resulted in increased biomass yield through increased number of tillers. It also improved the biomass composition through accumulation of starch in the parenchyma cells at the internodes, resulting in higher sugar release during enzymatic hydrolysis [252, 253]. However, for prominent herbaceous feedstocks like switchgrass, the pith parenchyma cells senesce as the plant matures and the stems become narrow and hollow with a very small proportion of parenchyma cells [254, 255]. The reduced pith parenchyma content in hollow-stemmed grass species thereby restricts their biofuel potential.

Wheat straw has been investigated as a potential feedstock for bioenergy production in numerous studies [121, 235, 256, 257]. Unlike in other grass species, which are either solid-stemmed or hollow, wheat varieties show variability in the stem solidness trait. In wheat, the major quantitative trait locus (QTL) for stem solidness is localized on chromosome 3B [258, 259], and has been identified as solid-stem locus 1 (SSt1) controlled by the Qss.msub-3BL allele [260]. Within the SSt1 locus, TdDof was identified as the key causal gene that is responsible for the stem solidness phenotype [261]. Stem solidness in wheat is important due to its positive impact on resistance to

stem sawfly larval infestation and lodging [262, 263]. However, it is unknown if the increased parenchyma cell content will also have a positive impact on biofuel potential from wheat straw varieties. In addition, engineering the stem solidness trait into hollow-stemmed grass species, such as switchgrass, could be extremely powerful to (i) increase the carbohydrate storage capacity of the biomass, (ii) improve digestibility, (iii) increase lodging resistance, and (iv) reduce biomass transportation costs by increasing the biomass density.

The goal of this study was to evaluate the tissue-specific differences in deconstruction between wheat cultivars with varying stem solidness and determine whether increasing stem solidness has a positive influence on wheat straw digestibility. Stem sections from three greenhouse-grown wheat cultivars with hollow (McNeal), semisolid (Vida), and solid (Choteau) stems were pretreated with 1 M sulfuric acid and 62.5 mM sodium hydroxide, respectively, at 100 °C in a previously constructed microfluidic imaging reactor. The same sections were then enzymatically hydrolyzed for 72 hr. Time lapsed imaging was conducted on all the samples using confocal laser scanning microscopy. The progress in pretreatment was monitored based on the changes in lignin autofluorescence and enzymatic hydrolysis progress was monitored through brightfield imaging.

## **4.2 Materials and Methods**

### **4.2.1 Wheat straw samples**

Three semi-dwarf, hard red spring wheat varieties with divergent pith fill phenotype (McNeal – hollow, Vida – semisolid, and Choteau – solid) were grown in a greenhouse at Michigan State University. All biomass was harvested and dried at 40-50 °C before they were shipped to Michigan Technological University for further experiments.

### **4.2.2 Preparation of PDMS (polydimethyl siloxane) reaction chamber**

A photoresist mold was prepared on a 5” silicon wafer with SU-8 100 using photolithographic techniques as described in our previous paper (Imaging reactor reference) and placed inside a plastic box. The PDMS was prepared by mixing 25 g of Sylgard 184 silicone elastomer base and 2.5 g of curing agent (10:1 ratio by weight) in a 50 mL disposable centrifuge tube. This mixture was poured onto the SU-8 100 mold in the plastic box and allowed to cure in a desiccator for 24 hours. The cured PDMS reactor chamber was removed using a Medblades (#12, Carbon) surgical blade.

### **4.2.3 Sectioning samples using a cryomicrotome**

McNeal, Vida, and Choteau sample cross sections (60 µm thickness) were prepared by embedding in TissueTek OCT compound and sectioned using a Thermo Scientific Microm HM550 P cryomicrotome set to -25 °C, as described previously (Imaging reactor manuscript reference). The sectioned McNeal, Vida, and Choteau samples (approximately 0.1 mg each) were mounted individually on 25 mm diameter cover glasses (Electron Microscopy Sciences circular cover glass #1, 25 mm). The glass coverslips containing the samples were adhered to the PDMS reactor chambers using



Gorilla super glue (Catalog No. 7501201) and allowed to dry for 2 min. To remove the water soluble TissueTek OCT compound, the samples and the coverslip were rinsed three times with 200  $\mu$ L deionized water using a pipette and allowed to dry before pretreatment. The outer side of the coverslip was wiped with 90% ethanol to remove any dust particles prior to imaging.

#### **4.2.4 Pretreatment experiments with time-lapsed imaging**

Dilute acid and alkali pretreatment was carried out on samples at 100 °C in a Fisherbrand gravity oven (Catalog No.151030521) oven using 200  $\mu$ L of 1 M sulfuric acid or 62.5 mM sodium hydroxide (~0.005% solids loading), respectively. The pretreatment experiments were carried out for 45 min. Every 15 minutes, the pretreatment supernatant was removed using a 1 mL BD U-100 syringe with detachable needle (Fisher Scientific Catalog No. 14-820-28) of which a 150  $\mu$ L aliquot was collected for HPLC analysis. The wheat straw samples were then washed three times with 200  $\mu$ L of deionized water to stop the reaction before conducting confocal laser scanning microscopy (CLSM) imaging. After CLSM imaging, fresh reagents were added to the reactor for the next stage in the pretreatment. This process was repeated every 15 minutes until the full 45 minutes was reached.

#### **4.2.5 Enzymatic hydrolysis with time-lapsed imaging**

Following imaging, enzymatic hydrolysis (final working volume of 400  $\mu$ L) was carried out on the pretreated samples at 50 °C in a static incubator for 72 hours. Novozymes 22257 cellulase and Novozymes 22244 hemicellulase (Novozymes, Franklinton, NC, USA) were loaded at 23 mg protein/g solids, at a ratio of 70% cellulase and 30% hemicellulase. The protein content of the enzymes was previously determined by first desalting using a disposable desalting column (Disposable PD-10 Desalting columns, Cytiva, VWR Catalog. No. 95017-001) and analyzing the protein content using the Pierce™ BCA Protein Assay Kit (Pierce Biotechnology). CLSM imaging was carried out on the hydrolyzed samples after 30 min, 4, 8, 12, 24, 48 and 72 hours. After each interval the hydrolysate was removed for HPLC analysis. The residual biomass was washed three times with deionized water before conducting CLSM. After CLSM imaging, fresh reagents were added to the reactor for the next stage of enzymatic hydrolysis.

#### **4.2.6 Biomass pretreatment for composition analysis**

Due to the extremely low biomass weight (0.1 mg), to obtain sufficient pretreated biomass for composition analysis, ~200-250 McNeal, Vida, and Chateau wheat straw sections (60  $\mu$ m thickness) were prepared on the cryomicrotome (method described earlier). These biomass sections were pretreated for 45 minutes at 100 °C in a Fisherbrand gravity oven (Catalog No.151030521) in 20 mL scintillation vials using either 5 mL of 1 M sulfuric acid or 62.5 mM NaOH (~0.02% solids loading). The pretreated solids and slurry were transferred to 50 mL centrifuge tubes and centrifuged at 4000 rpm for 30 min at 4 °C in a bench-top laboratory scale centrifuge (Eppendorf 5804R). The pretreatment supernatant was discarded, and the remaining solids were

washed three times with deionized water and dried overnight at room temperature in an aluminum weighing dish. The dried pretreated and untreated samples were roughly ground using a mortar and pestle and stored at room temperature in Ziploc bags until they were shipped for composition analysis.

#### **4.2.7 Acetyl bromide soluble lignin (ABSL) analysis**

The untreated and pretreated biomass were separately extracted to leave the alcohol insoluble residue and then evaluated for acetyl bromide soluble lignin (ABSL) content according to the method described previously (Barnes & Anderson, 2017). The ABSL values were obtained as % of AIR. About 250  $\mu\text{L}$  of 25% acetyl bromide (v/v) in glacial acetic acid was added to  $\sim 65$  mg of the destarched AIR of the samples. The samples were incubated at 50  $^{\circ}\text{C}$  for 3 hours. After digestion, the samples were cooled on ice for 5 min. They were then centrifuged at 1000 rpm (10,600  $\times$  g) for 5 min in an Eppendorf 5417R bench top centrifuge. About 100  $\mu\text{L}$  of the reaction supernatant and 75  $\mu\text{L}$  of 0.5 M hydroxyl amine were added to a glass culture tube. After mixing the contents of the culture tube manually, 400  $\mu\text{L}$  of 2 M sodium hydroxide 1.5 mL of glacial acetic acid and were vortex mixed. Following this, 200  $\mu\text{L}$  of the sample solution from the culture tubes was added to a UV-specific 96-well plate using filtered pipette tips. The absorbance of the sample solutions was measured by scanning the plate at 280 nm on a Spectra Max Plus 384 plate reader. The ABSL values were obtained as % of AIR.

#### **4.2.8 Matrix polysaccharide analysis**

About 2 mg of AIR was hydrolyzed with 2 M trifluoroacetic acid for 1.5 hours at 121  $^{\circ}\text{C}$ . The samples were evaporated to remove the trifluoroacetic acid, rinsed four times with isopropyl alcohol and resuspended in deionized water. The liquid was evaluated for hemicellulosic and pectic sugar monomers using HPLC and the solid residue was analyzed for crystalline cellulose using the previously described method [224].

#### **4.2.9 End-product analysis for pretreatment supernatant and hydrolysates**

The pretreatment supernatant and hydrolysates ( $\sim 150$   $\mu\text{L}$ ) were collected at each time point of imaging for end-product analysis. The pretreatment supernatant and the hydrolysates were diluted with 1350  $\mu\text{L}$  deionized water (10x dilution) and then filtered using a 0.2  $\mu\text{m}$  PES syringe filter (Agilent Catalog No. 5191-5922). Glucose, xylose, and other end-products were evaluated using high-performance liquid chromatography (HPLC) through an Aminex HPX-87H column (BioRad) and quantified using refractive index detection (RID) as described previously [65].

#### **4.2.10 Confocal microscopy, image processing, and data analysis**

Confocal laser scanning microscopy (CLSM) of pretreated and enzymatically hydrolyzed samples was carried out on an Olympus FV1000 confocal microscope, using an excitation wavelength of 405 nm with a DAPI bandpass filter (480-550 nm) at 23% laser

power and 1024 x1024 pixel resolution. For each run of CLSM imaging, 60 slices were obtained. Brightfield images were also recorded for samples following enzymatic hydrolysis, as the autofluorescence signals were very low following pretreatment. Images were processed with Fiji (ImageJ) software [176, 187, 264]. The image stacks comprising 60 slices were converted to average-intensity Z-projection images. The changes in cell wall thickness were recorded for all the stages of pretreatment. The fluorescence intensity data were obtained for parenchyma, sclerenchyma, metaxylem, and protoxylem regions by adding a line ROI (region of interest) across the respective cell walls. The average fluorescence intensity profile and cell wall thickness was obtained based on three replicates on the image for each cell type.

#### 4.2.11 Calculations

Enzymatic hydrolysis conversions of glucose and xylose were calculated as described previously [265]

*Glucose conversion (% of theoretical)*

$$= \frac{\text{glucose concentration } \left(\frac{g}{L}\right) * \text{hydrolysate volume (L)} * 0.9}{\text{polysaccharides in the untreated dry biomass (g)}} * 100\%$$

*Xylose conversion (% of theoretical)*

$$= \frac{\text{xylose concentration } \left(\frac{g}{L}\right) * \text{hydrolysate volume (L)} * 0.88}{\text{polysaccharides in the untreated dry biomass (g)}} * 100\%$$

### 4.3 Results

In order to investigate the effect of pith fill phenotype on biomass deconstruction, three wheat cultivars were selected with varying stem solidness: McNeal (hollow), Vida (semisolid), and Choteau (solid) cultivars were obtained (**Figure 4.1A**). Approximately 37% and 17.4% of the stem cross sectional area was hollow for McNeal and Vida, respectively. The CLSM images show lignin autofluorescence in these samples (**Figure 4.1B, 1C, 1D**).

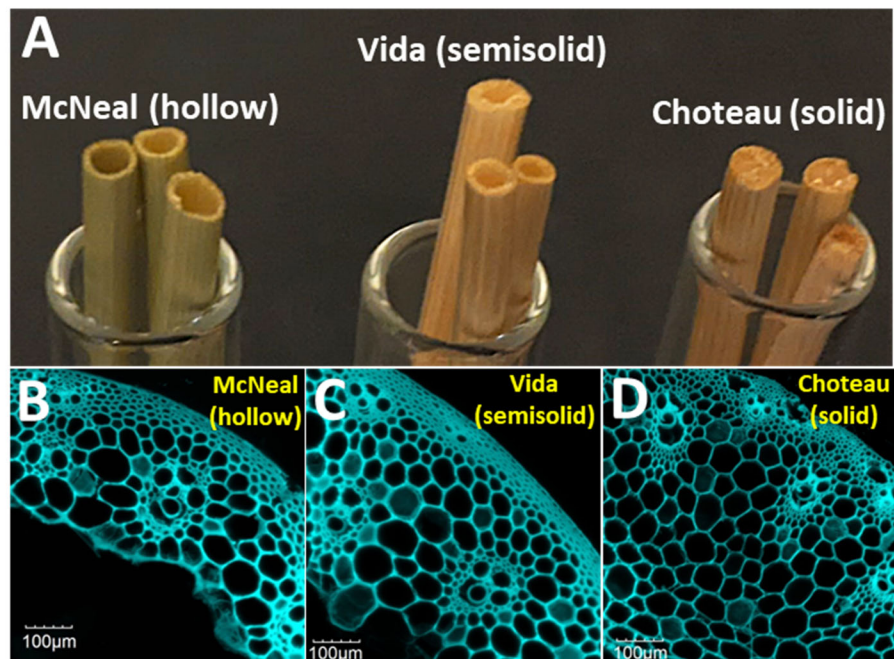


Figure 4.1. A) Images of McNeal (hollow), Vida (semisolid), and Choteau (solid) samples. B, C and D) CLSM images of untreated McNeal, Vida, and Choteau samples showing lignin autofluorescence. The excitation wavelength was 405 nm with a DAPI emission bandpass filter (480-550 nm).

#### 4.3.1 Lignin autofluorescence decrease was greatest for the protoxylem cells in the Choteau samples during dilute acid and alkali pretreatments

There was a gradual loss of lignin autofluorescence signal for all the samples (McNeal, Vida, and Choteau) after 15, 30 and 45 min of dilute acid pretreatment. However, for all the samples, autofluorescence signals were not completely eliminated, even after 45 min pretreatment (**Figure 4.2**). The cell corners (red arrows) in the McNeal samples, particularly around the vascular bundles, appear to have higher autofluorescence intensity for all the stages of pretreatment (**Figure 4.2A-D**). However, for Vida (**Figure 4.2G, 2H**) and Choteau (**Figure 4.2K, 2L**) samples, the fluorescence intensities did not vary between the cell corners (red arrows) and other regions after 30 min pretreatment.

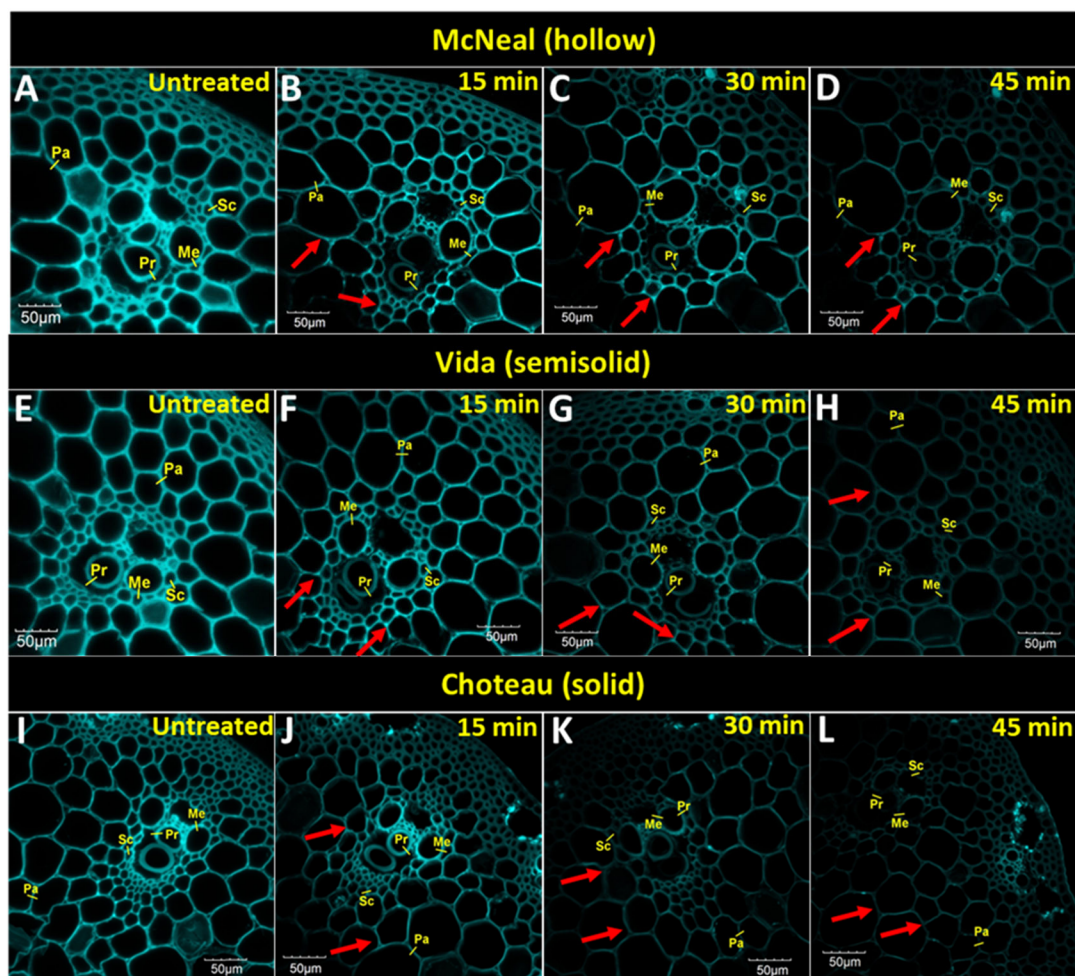
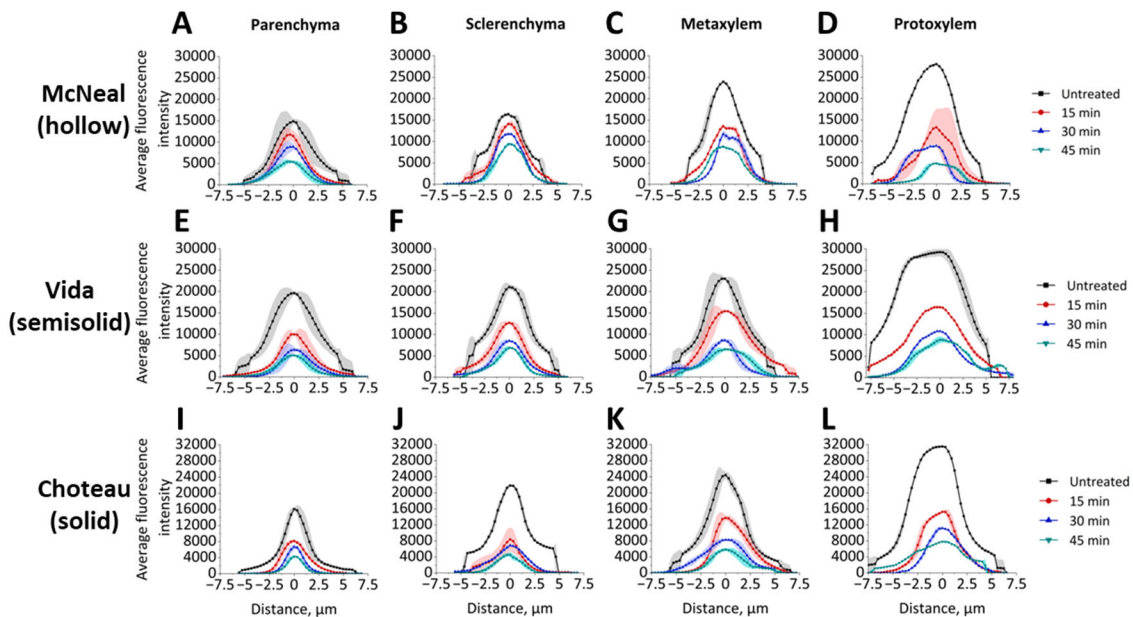


Figure 4.2. A gradual loss of lignin autofluorescence signals was observed for McNeal (A-D), Vida (E-H), and Choteau (I-L) samples after 15 min (B, F, J), 30 min (C, G, K), and 45 min (D, H, L). Dilute acid pretreatment was carried out on 60  $\mu\text{m}$  thick McNeal, Vida, and Choteau sections using 1 M sulfuric acid at 100  $^{\circ}\text{C}$ . The excitation wavelength was 405 nm with a DAPI emission bandpass filter (480-550 nm).

The initial fluorescence intensity was the highest for the protoxylem cell wall of Choteau sample (Figure 4.3L) and lowest initial fluorescence was from the Choteau parenchyma cell wall (Figure 4.3I). When the parenchyma (Figure 4.3A, 3E, 3I) cell walls are compared between McNeal, Vida and Choteau, the Vida (Figure 4.3A) sample had the highest initial fluorescence intensity and Choteau had the lowest (Figure 4.3I). During the different stages of pretreatment, the parenchyma cells of Choteau sample had the lowest residual fluorescence, and the McNeal had the highest residual fluorescence after 45 min dilute acid pretreatment (Figure 4.3A, 3I). Similarly, for the sclerenchyma cells, the Choteau samples lost approximately 82% of the initial lignin autofluorescence after 45 min pretreatment (Figure 4.3J). However, the sclerenchyma cell walls in the McNeal and Vida samples experienced about 45% and 53% decrease in lignin autofluorescence, respectively. The loss of fluorescence in the metaxylem (Figure 4.3C, 3G, 3K) cell walls were similar for the McNeal, Vida and the Choteau samples, McNeal exhibiting the

highest residual fluorescence after 45 min pretreatment (**Figure 4.3C**). But, for the protoxylem cell walls, the McNeal sample lost about 85% of its initial fluorescence intensity after 45 min pretreatment (**Figure 4.3D**). However, the protoxylem cell walls in the Vida and Choteau samples only lost 64% and 67% of the initial fluorescence intensities (**Figure 4.3H, 3L**). Overall, the lignin autofluorescence of the Choteau parenchyma (**Figure 4.3I**) cells seem to be altered the most during dilute acid pretreatment than all the other cell types, confirmed by the low residual fluorescence intensity after 45 min pretreatment.



**Figure 4.3.** Different cell types in the McNeal (A-D), Vida (E-H) and Choteau (I-L) samples showed variations in their lignin autofluorescence intensities during dilute acid pretreatment with 1M sulfuric acid at 100 °C. Values for all subfigures are reported as mean  $\pm$  S.D., n=3.

The loss of lignin autofluorescence at the different stages of dilute alkali pretreatment (15, 30, and 45 min) (Figure 4.4) was similar to the dilute acid pretreatment. However, the higher fluorescence intensity near the cell corners was not observed beyond 15 min pretreatment for all the three samples, McNeal (**Figure 4.4C, 4D**), Vida (**Figure 4.4G, 4H**) and Choteau (**Figure 4.4I, 4L**). Interestingly, after 30-45 min of alkali pretreatment, the Choteau vascular bundles retained significant autofluorescence in the sclerenchyma cells located inside the vascular bundles, between the xylem vessels compared to the other cell types (**Figure 4.4K, 4L**). This pattern was not observed in the McNeal or Vida stems.

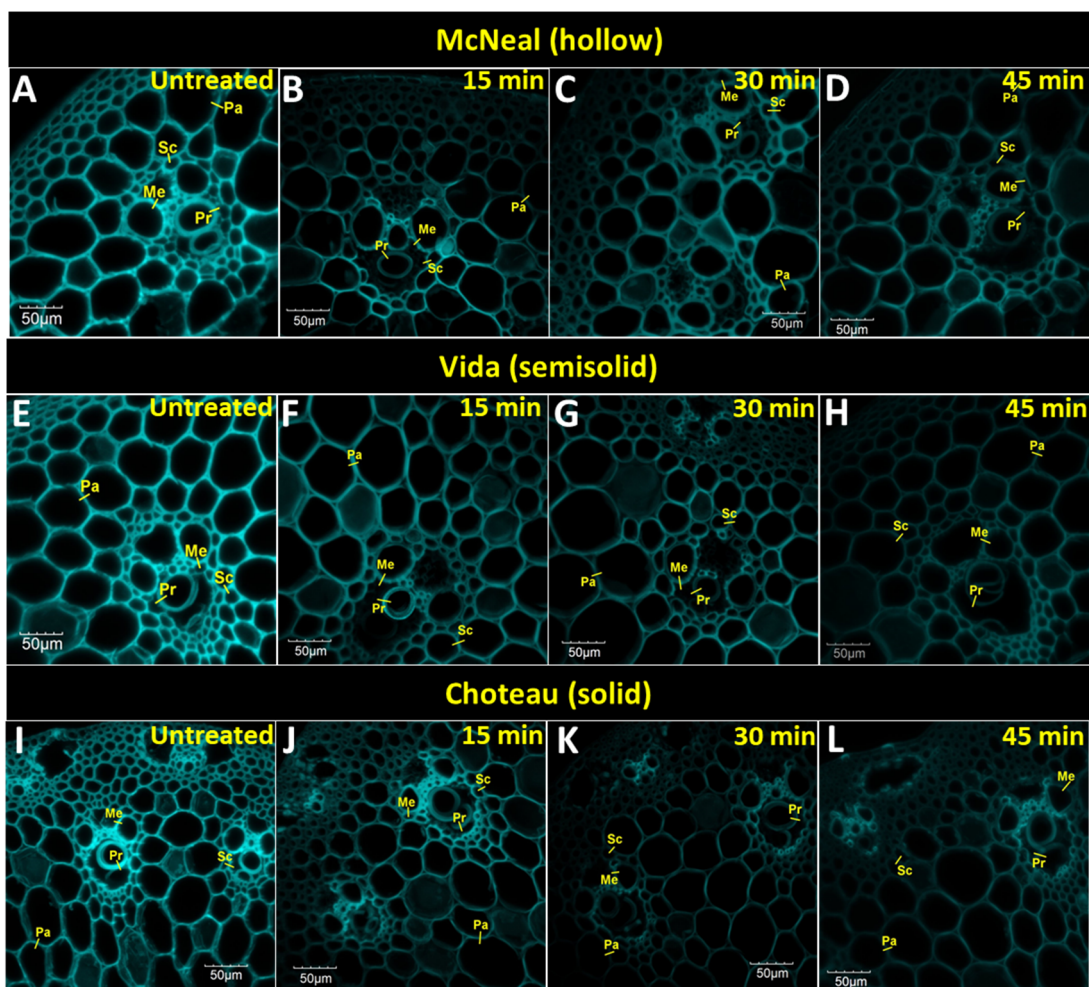
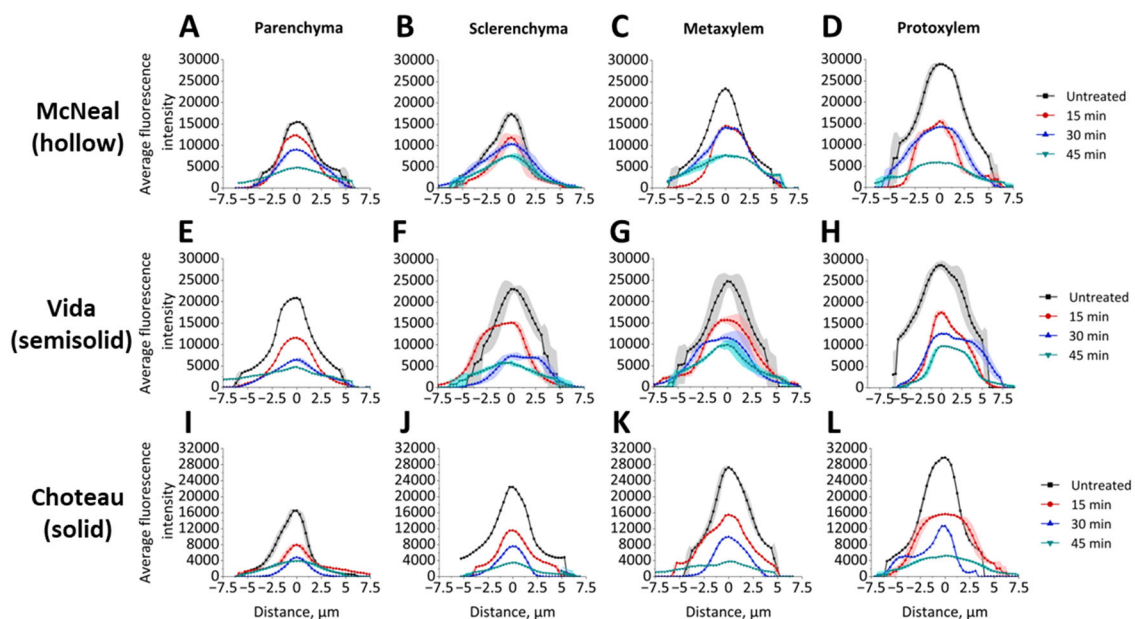


Figure 4.4. A gradual loss of lignin autofluorescence signals was observed for McNeal (A-D), Vida (E-H), and Choteau (I-L) samples after 15 min (B, F, J), 30 min (C, G, K), and 45 min (D, H, L). Dilute alkali pretreatment was carried out on 60 μm thick McNeal, Vida, and Choteau sections using 62.5 mM sodium hydroxide at 100 °C. The excitation wavelength was 405 nm with a DAPI emission bandpass filter (480-550 nm).



**Figure 4.5.** Different cell types in the McNeal (A-D), Vida (E-H) and Choteau (I-L) samples showed variations in their lignin autofluorescence intensities during dilute alkali pretreatment with 62.5 mM sulfuric acid at 100 °C. Values for all subfigures are reported as mean  $\pm$  S.D., n=3. Three regions of interest were selected for each cell type to obtain the fluorescence intensity profile.

### 4.3.2 The epidermis cell wall thickness varied the most for the Choteau (solid) samples

As cell wall polymers are removed during pretreatment, the wall can loosen, leading to a measurable expansion or swelling effect. The cell wall thicknesses of the parenchyma, epidermis, metaxylem, protoxylem, and sclerenchyma were measured for McNeal (hollow), Vida (semisolid), and Choteau (solid) cultivars after different stages of dilute acid and dilute alkali pretreatment. The overall increase in thickness was higher for all the alkali-pretreated samples (Figure 4.6D-F) than the acid-pretreated samples (Figure 4.6A-C). For the epidermis cell wall, the initial thickness was the highest for McNeal (hollow) when compared to Vida (semisolid) and Choteau (solid). The parenchyma cell walls of the Choteau samples had the lowest initial cell wall thickness (**Figure 4.6C, 6F**).



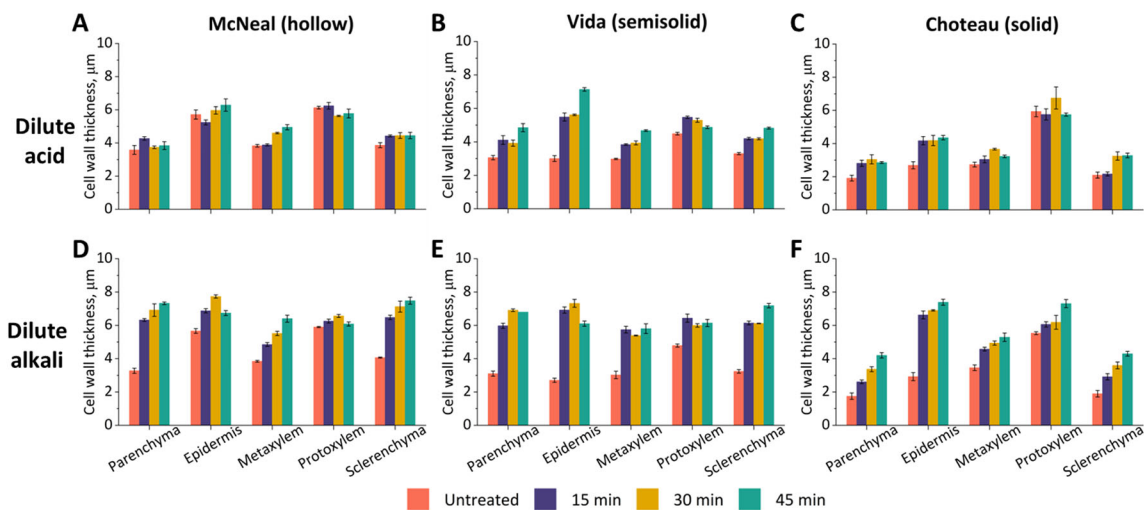


**Figure 4.6.** The cell wall thickness increased more following dilute alkali pretreatment than dilute acid pretreatment. Dilute acid pretreatment was carried out on a 60 µm thick wheat straw samples using 1 M sulfuric acid and dilute alkali pretreatment with 62.5 mM sodium hydroxide at 100°C. Values for all subfigures are reported as mean ± S.D., n=3. Three regions of interest were selected for each cell type to obtain the cell wall thickness.

### 4.3.3 Lignin removal and hemicellulose hydrolysis during pretreatment were evaluated through composition analysis

Arabinose and xylose were hydrolyzed completely during the dilute acid pretreatment for all the samples (Figure 4.7B, 7C). There was a drastic decrease in ABSL (acetyl bromide soluble lignin) for the dilute alkali pretreated samples (Figure 4.7A). The xylose conversion was the highest for Choteau (~41%) sample during dilute acid pretreatment, followed by McNeal (~24%) and Vida (~17%) (Figure 4.7D). For the dilute alkali pretreated samples, the xylose conversion was <1% for all the three cultivars (Figure 4.7D). The glucose conversion was <1% for all the three cultivars, during both acid and alkali pretreatment.

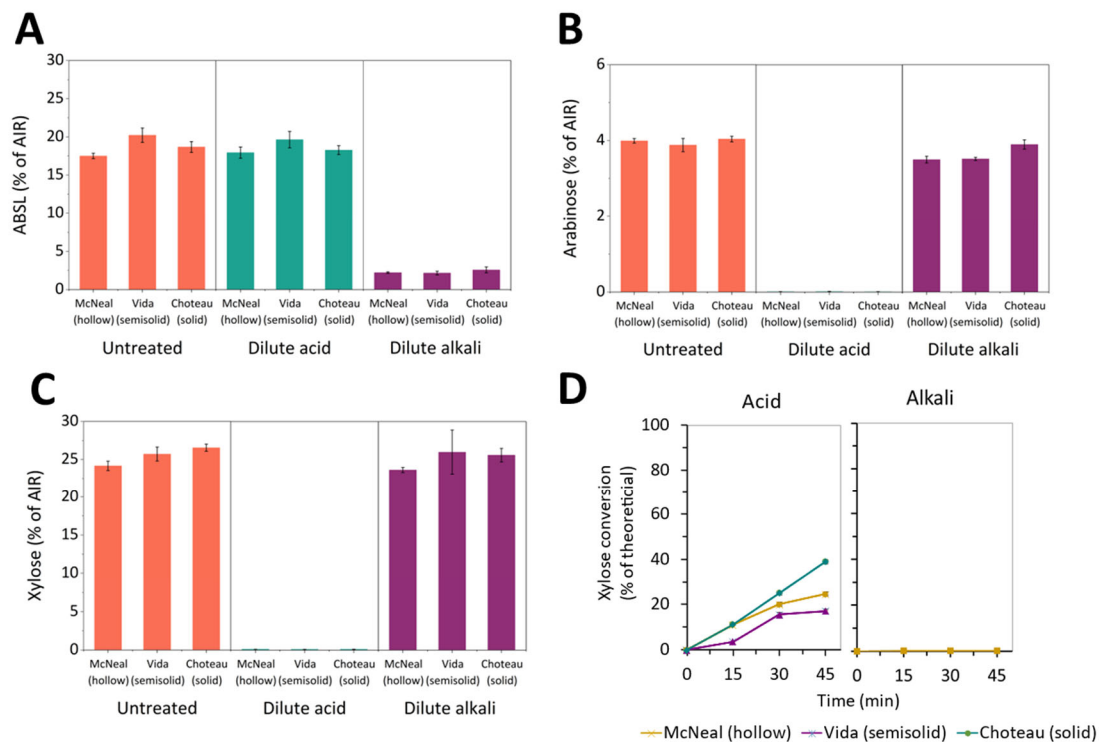


**Figure 4.7. A) Acetyl bromide soluble lignin (ABSL) decreased for the dilute alkali pretreated McNeal, Vida, and Choteau samples due to lignin solubilization. B) Arabinose and C) xylose composition decreased for the dilute acid pretreated McNeal, Vida, and Choteau samples due to hemicellulose hydrolysis. Values are reported as percentage of acid insoluble residue (AIR). D) Cumulative xylose release during dilute acid pretreatment was higher for the Choteau sample than the McNeal and Vida samples. There was <1% xylose release than during dilute alkali pretreatment for all the three samples. Values for all subfigures are reported as mean  $\pm$  S.D, n=2 composition analysis replicates (A, B, C) and pretreatment supernatant (D) replicates.**

#### 4.3.4 Glucose and xylose conversion following enzymatic hydrolysis was positively affected by stem solidness

The acid- and alkali-pretreated McNeal, Vida and Choteau samples were subjected to enzymatic hydrolysis at 23 mg protein/g solids. During the initial trials, enzymatic hydrolysis was carried out at 1 mg, 5 mg, and 10 mg protein/g solids. There was no biomass deconstruction even after 96 hours. The glucose and xylose conversions during enzymatic hydrolysis were the highest for the Choteau, for both acid- and alkali-pretreated samples (Figure 4.8). The glucose conversion for acid-pretreated Choteau sample was approximately 26% and 30% higher than the McNeal and Vida samples, respectively (Figure 4.8A). The glucose conversion for the alkali-pretreated Choteau sample was approximately 690% and 120% higher than the McNeal and Vida samples, respectively (Figure 4.8C). These drastic differences in glucose conversion for the alkali pretreated samples were due to the very low glucose conversions of the McNeal (7.8%) and Vida (27.5%) samples. Between McNeal and Vida, the glucose conversion was slightly higher for McNeal (~3%) for the acid pretreated samples (**Figure 4.8A**).

However, for the alkali pretreated samples, Vida had about 250% higher glucose conversion than the McNeal sample (Figure 4.8C). Between the alkali and acid pretreated samples, the acid pretreated samples showed approximately 650%, 109% and 20% higher glucose conversion for McNeal, Vida, and Choteau samples, respectively (Figure 4.8). The xylose conversion for acid pretreated Choteau sample during enzymatic hydrolysis was approximately 396% and 134% higher than McNeal and Vida samples, respectively (Figure 4.8B). The xylose conversion for the alkali-pretreated Choteau sample was 494% and 105% higher than the McNeal and Vida samples, respectively (Figure 4.8D). The xylose conversions during enzymatic hydrolysis of the alkali pretreated samples were approximately 23%, 67%, and 47% higher than the acid pretreated samples for McNeal, Vida, and Choteau, respectively (Figure 4.8B, 7D). This is because there is a significant xylose conversion during acid pretreatment for all the three cultivars (Figure 4.8D).

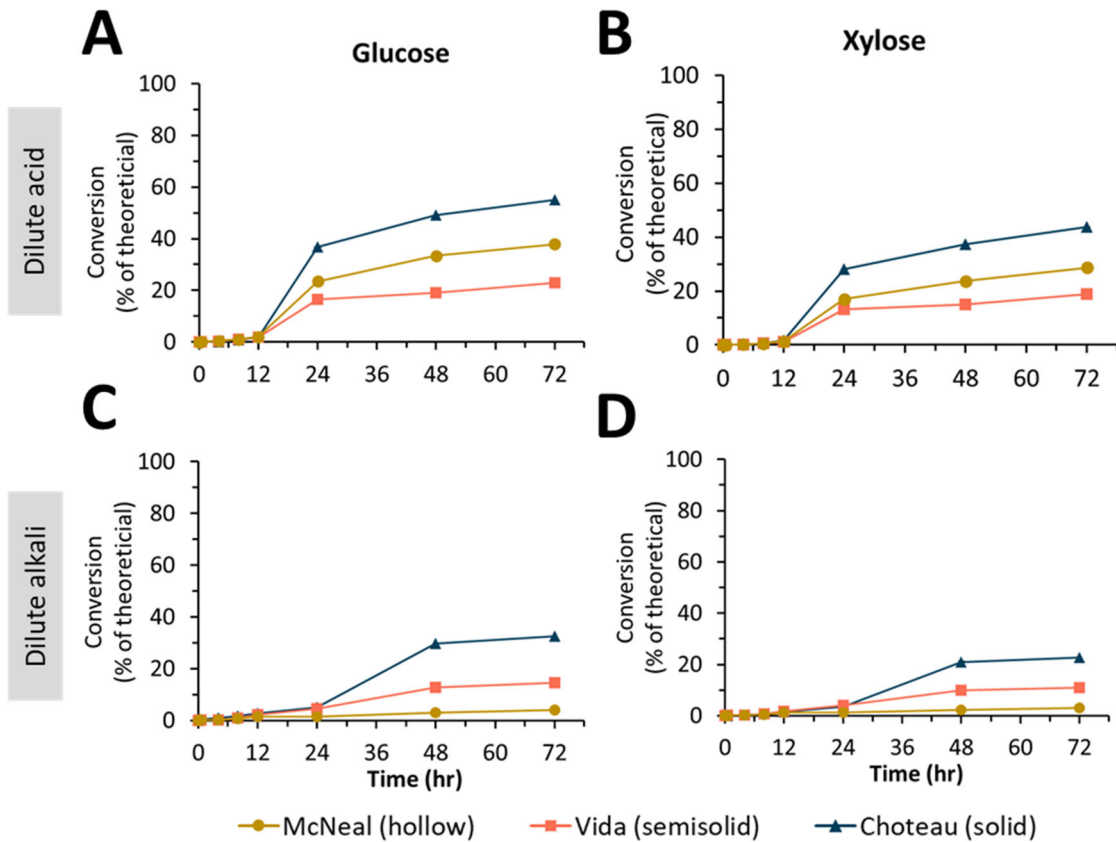


**Figure 4.8.** Glucose and xylose conversion for Choteau, Vida and McNeal samples after dilute acid and dilute alkali pretreatment. Values for all subfigures are reported as mean  $\pm$  S.D., n=2 hydrolysate replicates.

### 4.3.5 Enzymatic hydrolysis images

For the acid pretreated samples (Figure 4.9), McNeal samples did not show any significant structural change in the vascular bundle and the parenchyma cells until 48 hours (Figure 4.9A-G). After 72 hours (Figure 4.9H), very few parenchyma cells had degraded inside the culm. Acid-pretreated Vida showed a similar pattern, with a minor loss of parenchyma cells between the hollow and the start of the vascular bundles between 4-8 hr, but very little obvious degradation after this point (Figure 4.9 I-P). In contrast, the Choteau stem remained largely intact for the first 24 hours (Figure 4.9 Q-V) after which the pith parenchyma disintegrated completely by 48 hours of enzymatic hydrolysis (Figure 4.9W), the pith parenchyma cells had disintegrated completely, leaving the outer rind region largely intact for the remainder of hydrolysis, similar to the other wheat varieties (Figure 4.9X).

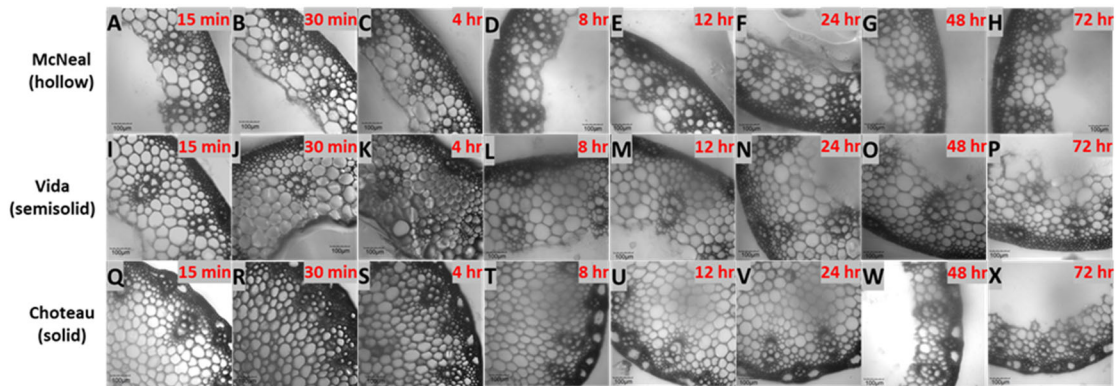
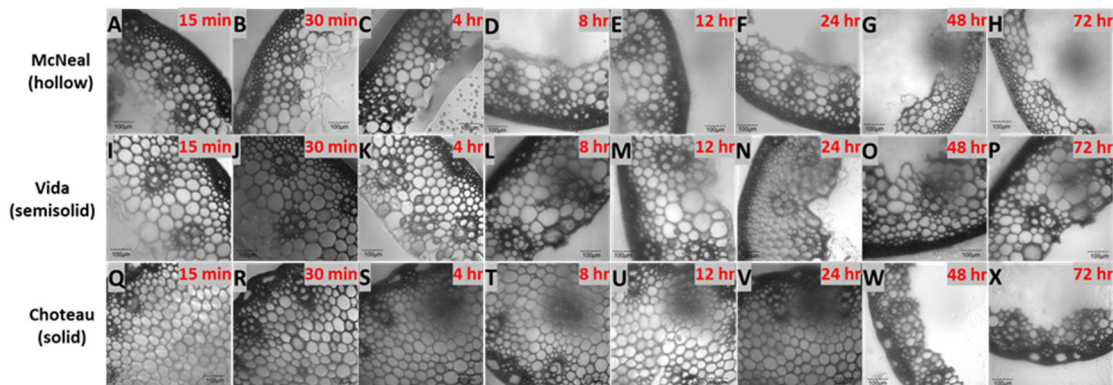


Figure 4.9. Brightfield images of dilute acid-pretreated McNeal (A-H), Vida (I-P), and Choteau (Q-X) samples during enzymatic hydrolysis.

Structural observations during enzymatic hydrolysis for the alkali pretreated samples (Figure 4.10) were nearly identical to those observed for the acid pretreated wheat stem sections. McNeal samples did not show any significant structural change in the vascular bundle and the parenchyma cells until 24 hours (Figure 4.10 A-F). After 48 hours (Figure 4.10G), some of the parenchyma and sclerenchyma cells degraded inside the culm. Despite more structural changes than the dilute acid pretreated samples, the glucose conversion of the alkali pretreated sample was extremely low, approximately 7.8%, for the alkali pretreated McNeal samples (Figure 4.8C). Alkali pretreated Vida showed a slightly different pattern of enzymatic hydrolysis than McNeal, with no significant structural degradation of parenchyma cells even at 72 hours (Figure 4.10I-P). Alkali pretreated Choteau exhibited a similar trend of enzymatic hydrolysis like the acid pretreated sample. Most of the cell wall structure remained intact till 24 hours of enzymatic hydrolysis (Figure 4.10Q-V) whereas after 48 hours (Figure 4.10W), the pith parenchyma cells had disintegrated completely. However, a few parenchyma cells in the rind region seem to have hydrolyzed for the alkali pretreated sample after 72 hours (Figure 4.10X).



**Figure 4.10. Brightfield images of dilute alkali pretreated McNeal (A-H), Vida (I-P), and Choteau (Q-X) samples during enzymatic hydrolysis.**

## 4.4 Discussion

The gradual loss of lignin autofluorescence during acid and alkali pretreatment (**Figure 4.2, Figure 4.4**) is similar to the loss of lignin autofluorescence intensity reported for dilute acid, NaOH/urea, NaOH and CaO pretreatment of wheat straw, sorghum and miscanthus [218, 266, 267]. Previous studies have reported severely deformed and disjoint parenchyma cell walls during the dilute acid pretreatment of grasses like wheat straw and miscanthus [70, 71, 218]. In contrast, we did not observe any severe deformations or disjoining in the entire biomass section during the pretreatment for all three of our samples, McNeal, Vida, and Choteau (**Figure 4.2**). This is likely because our pretreatment temperature was low (100 °C), whereas the previous studies conducted the dilute acid pretreatment at temperatures >120 °C, which is the glass transition temperature of lignin [70, 71, 218]. After dilute acid pretreatment, the lowest residual fluorescence occurred in the pith parenchyma cells of the Choteau sample (**Figure 4.3I**) and could be due to a lower lignin content in the pith region than the rind region in grasses [14, 268-270]. A previous study on dilute acid pretreatment of miscanthus using CLSM, SEM, and TEM has reported that the pith region was more susceptible to dilute acid pretreatment than the rind region, especially the pith parenchyma cells [70]. The lower fluorescence intensities in the parenchyma cells of the untreated and pretreated McNeal and Vida samples (**Figure 4.3A, 3E, 3I, Figure 4.5A, 5E, 5I**) than the vascular bundles are in agreement with previous studies that tracked lignin autofluorescence changes for hollow wheat straw samples during alkali and steam explosion pretreatment [173, 266]. Previous studies on solid-stemmed herbaceous feedstocks like corn stem and sugarcane have also reported a higher loss of lignin autofluorescence in the parenchymatous cell walls in the pith region than the rind region [271, 272].

In hollow wheat straw stems, the inner layer of modified parenchyma cells is known as the pith cavity lining (PCL) [273]. Hansen et al. reported that this layer of parenchyma cells had undergone a higher disruption than the rind after hydrothermal pretreatment at 185 °C [274, 275]. They reported a 16% glucan conversion during enzymatic hydrolysis [274]. This is similar to our results, in which the alkali pretreated McNeal (hollow) and

Vida (semisolid) samples show 7.8% and 27.5% glucose conversion (**Figure 4.8C**). The cellular structure of the rind region for all acid- and alkali-pretreated wheat straw varieties appeared largely intact, even after 72 hours of enzymatic hydrolysis. This could be due to the higher lignin and hemicellulose content in the rind region of grasses [154, 181, 225, 268]. This also indicates that the higher glucose and xylose conversions for the Choteau samples was likely due to the stem solidness trait, resulting in an abundance of pith parenchyma cells that were completely digested within 48 hr (**Figure 4.9, Figure 4.10**). A previous study on alkali-pretreated sorghum, which is a solid-stemmed feedstock, showed that the parenchyma cells had a faster hydrolysis rate when compared to the vascular bundles [237]. Li et al. conducted alkali pretreatment and enzymatic hydrolysis on physically fractionated pith and rind of sorghum samples. They found that the isolated pith parenchyma were the least recalcitrant to enzymatic hydrolysis [270]. Similarly, Ji et al. reported a drastically high cellulose conversion for the pith region of dilute acid-pretreated miscanthus than the corresponding rind region [70]. A previous study on untreated sugarcane has reported 20% glucose conversion for the rind region, whereas the pith parenchyma cells showed a 60% glucose conversion, which the authors attributed to the 40% higher lignin content in the rind region [14]. Several studies have reported that the pith region of corn stover readily hydrolyzed by cellulases after liquid hot water, dilute acid, and ionic liquid pretreatments [15, 276-278]. Based on our findings and the previous evidence on the high sugar yields from the pith parenchyma cells, stem solidness is a valuable trait in grasses to improve sugar yields.

## 4.5 Conclusion

The difference in digestibility based on the stem solidness trait was evaluated for three wheat straw cultivars with hollow (McNeal), semisolid (Vida), and solid (Choteau) stems. Changes in lignin autofluorescence during dilute acid and dilute alkali pretreatment indicated that the McNeal and Vida samples were more resistant to pretreatment than the pith region of Choteau samples. The pith-parenchyma cells of the Choteau (solid) sample were the most susceptible to enzymatic hydrolysis after both acid and alkali pretreatment, degrading completely within 48 hours, which led to significantly higher 72-hr glucose and xylose conversions compared to the hollow-stemmed varieties, McNeal and Vida. Given their greater digestibility, solid-stemmed wheat straw cultivars would have greater value as biorefinery feedstocks compared to hollow-stemmed cultivars. In addition, engineering hollow-stemmed grass species, such as switchgrass, to express a solid-stemmed phenotype at maturity may be a valuable approach to developing improved feedstocks for biofuel production.

## 4.6 Funding

This material is based upon work supported by the Great Lakes Bioenergy Research Center, U.S. Department of Energy, Office of Science, Office of Biological and Environmental Research under Award Number DE-SC0018409.

## **4.7 Acknowledgments**

We gratefully acknowledge Novozymes for generously providing the enzymes used during enzymatic hydrolysis. We thank R. Johnson and the GLBRC Biomass Analytical Facility for biomass composition analysis; M. McGee and the GLBRC Metabolomics Core Facility for HPLC analysis of pretreatment supernatant and hydrolysates. We thank Michigan Technological University's Applied Chemical and Morphological Analysis Laboratory and Microfabrication Facility for providing the equipment required to complete parts of this work.

## **5 A HIGH SOLIDS FIELD TO FUEL RESEARCH PIPELINE TO IDENTIFY INTERACTIONS BETWEEN FEEDSTOCKS AND BIOFUEL PRODUCTION**

### **5.1 Background**

Liquid transportation fuels from lignocellulosic biomass can play a vital role in reducing greenhouse gas emissions and mitigating climate change [279]. Environmental factors experienced during plant growth, such as weather extremes, have the potential to cause adverse effects on biomass quality and quantity [280, 281]. Decreased yield due to drought is a serious challenge to uninterrupted supply of feedstock for biofuel production [282-284]. Several studies have focused on the effects of abiotic stressors, such as drought, extreme temperatures, and heavy metal and salt concentrations on feedstock yield and composition to identify ecosystems suitable for their cultivation and develop sustainable bioconversion processes [21, 285, 286]. Although environmental factors can also affect the deconstruction of feedstocks into biofuel and resulting fuel yields, only a few studies have evaluated these effects [20, 23, 24]. There are a number of challenges in conducting these field-to-fuel experiments that span the entire biofuel production chain. First, a thorough analysis of the environmental effect on feedstocks and subsequent correlation to biofuel production requires samples from multiple plots and locations, which needs a higher level of throughput for the process than can be achieved in bioreactors. Second, there is a limit on minimum scale for reliable (useful or interpretable) fermentation experiments in order to be comparable to experiments performed in bioreactors. This requires a minimum hydrolysate volume and moderately sized pretreatment and hydrolysis vessels. Thus, there is a need for a platform that is able to accommodate a larger number of samples, while generating sufficient volumes of hydrolysate in a reasonable time frame.

Laboratory scale enzymatic hydrolysis for screening numerous lignocellulosic materials is usually performed at a substrate solid loading of 1 wt.% in a vial or up to 5 wt.% in a shake flask [105]. However, high solids loading hydrolysis (18 wt.% or higher) is needed to more accurately represent industrial conditions. Enzymatic hydrolysis at high solids loading increases the economic feasibility of the bioconversion process as it reduces the operating cost for hydrolysis and fermentation and minimizes energy requirements for other downstream processes, such as distillation [20, 100, 109]. However, as solids loading increases, the water available to facilitate the diffusion of enzymes into the biomass and the diffusion of sugars out into solution decreases [104, 108, 287]. Water availability is also important to reduce the viscosity of the slurry, thereby reducing the energy required for mixing. Poor mixing due to low water availability is a significant bottleneck for high solids loading operating conditions [101, 288, 289]. Shake flasks are commonly used lab equipment for enzymatic depolymerization of biomass, but they do not provide sufficient shear rates to reduce viscosity at high-solids concentrations. Inadequate mixing results in hydrolysis product build up in specific areas of the flask and improper enzyme distribution. In a shake flask, the highly viscous biomass and water mixture accumulates near the walls of the flask, which is the low shear zone of the



reaction vessel [290, 291]. In contrast to orbital shaking, gravitational tumbling has been found to be effective in mixing under high solids conditions [102, 292, 293]. Fed-batch, high solids loading enzyme hydrolysis has also been studied extensively as a means to overcome mixing issues [78, 115, 294]. In this method, the experiment is started with a moderate amount of the biomass, and a small dose of biomass is added at regular intervals. Fed batch optimizes the inherent pseudoplastic behavior of the high solids slurry by improving the water availability for enzymatic hydrolysis [295, 296]. However, fed batch loading also increases the likelihood of contamination if not conducted in a controlled manner.

The objective of this project was to develop a laboratory-scale high solids field-to-fuel platform to evaluate fermentation performance of diverse feedstocks. Custom pretreatment reactors were designed to process sufficient AFEX-treated biomass to generate the volume of high solids hydrolysate required for fermentation [77]. Enzymatic hydrolysis was conducted using gravitational tumbling in a static incubator to ensure proper mixing under high solids loading conditions and compared to the conventional method using shake flasks. Enzymatic hydrolysis parameters including solids loading, buffer concentration, and pH were optimized to achieve the highest volumes of hydrolysate and sugar conversion. The hydrolysates were fermented using *Saccharomyces cerevisiae* or *Zymomonas mobilis* with a system that measures real time CO<sub>2</sub> production in order to determine fermentation rate without extensive manual sampling and culture depletion. The fermentation performance of the platform was validated using two switchgrass samples that previously have shown divergent fermentation performance when processed at a larger scale for all steps - pretreatment, hydrolysis, and fermentation. This field-to-fuel platform can be used to rapidly identify the effects of environmental conditions, genetic background, or other parameters that influence feedstock quality, on microbial fuel production under industrially relevant enzymatic hydrolysis and fermentation conditions.

## **5.2 Materials and Methods**

### **5.2.1 Biomass Growth, Harvest and Processing**

The biomass samples used for the experiments in this study (corn stover, switchgrass, sorghum, restored prairie, and miscanthus) were cultivated at the DOE-Great Lakes Bioenergy Research Center's (GLBRC) Biofuel Cropping Systems Experiments (BCSE) located at the Arlington Agricultural Research Station in southcentral Wisconsin, USA (ARL, 43° 17' 45" N, 89°22' 48" W, 315 m a.s.l) and the W.K. Kellogg Biological Station in southwest Michigan, USA (KBS, 42° 23' 47" N, 85° 22' 26" W, 288 m a.s.l) [297, 298]. The mean annual temperature and precipitation were 6.9 °C and 869 mm, respectively. The soil type is Plano silt-loam, which is fine-silty, mixed, super active, mesic Typic Argiudoll; well-drained. Mollisol developed over glacial till and formed under tallgrass prairie. Switchgrass (SG) was sourced from ARL-346 in both 2010 and 2012. Sorghum (SOR), Miscanthus (MSC) and Restored Prairie (RP) were sourced from ARL-AUX TRIAL, ARLG6R5 and ARLG5R4 in 2014. Corn stover (CS) was sourced from ARL570 in 2008. Field plots (28 m x 40 m) were harvested and chopped into a

wagon. When the wagons were unloaded, a representative 25 kg sample was collected. The harvested plant materials were dried in a 60 °C oven, milled using a Christy Turner mill (Christy Turner Ltd. Suffolk, UK) and then milled materials mixed by hand to ensure homogeneity before being packaged in sealed plastic bags until use. The composition testing conducted previously across multiple bags and feedstocks have not shown significant difference in biomass composition, the data for which have not been published. We used corn stover samples for the optimization of the high solids loading roller bottle enzymatic hydrolysis method. The switchgrass (SG), sorghum (SOR), miscanthus (MSC) and restored prairie (RP) samples, which are mentioned above, were used to confirm the effectiveness of the method on a variety of grass feedstocks.

### 5.2.2 Cell Wall and Bulk Chemical Composition of Biomass

The samples were milled before the analysis using a Cyclotec™ mill (Foss, Denmark), equipped with a 2 mm screen. The composition of the bulk biomass (Table 9.2-1) was determined using the standard method described by the NREL laboratory analytical procedures for composition analysis of biomass [299]. All composition experiments were performed in triplicate.

### 5.2.3 Ammonia Fiber Expansion (AFEX) Pretreatment

The corn stover, switchgrass, sorghum, restored prairie, and miscanthus samples were pretreated using ammonia fiber expansion (AFEX) pretreatment. The pretreatment experiments were carried out in a 3.8 L high-pressure Parr reactor (Parr Instrument Co. Moline, IL, USA), which was placed inside a walk-in fume hood. Dry biomass mixed with water (0.6 g H<sub>2</sub>O/g dry biomass) was loaded into the Parr reactor and sealed. The sealed reactor was charged with nitrogen to 60 psi. The reactor was then preheated to suitable temperatures according to the type of biomass. Liquid ammonia at a loading of 2 g NH<sub>3</sub>/g dry biomass, was added to the biomass using a LEWA EK1 metering pump (Leonberg, Germany) [20]. After ammonia loading, the reactor temperature was increased to the set point within 5 min and then maintained at the set point temperature for the 30 min residence time. At the completion of the reaction, the ammonia was vented out from the reactor inside the walk-in fume hood. The pretreated biomass was then dried in a custom fume-vented drying box. The dried AFEX pretreated biomass (<12 % moisture content on a total weight basis) was packed into sterilized bags and stored at room temperature until it was used [300].

The 2010 and 2012 harvested switchgrass that were used for the field-to-fuel process validation studies were pretreated in custom AFEX reactors, as described previously [77]. In brief, 25 grams of untreated biomass (dry weight basis) was mixed with water (0.6 g H<sub>2</sub>O per g dry biomass) and loaded into the custom pretreatment reactors. The reactor was preheated to 60°C, and then ammonia was added using a high-pressure ammonia syringe pump (Harvard Apparatus 70-3311) equipped with a 100 mL stainless steel syringe to achieve a loading of 2 g NH<sub>3</sub> per g dry biomass. The reactor was heated to 120°C and maintained at the set point until 30 minutes after ammonia addition, at which point the reactor was vented, cooled and unloaded. The pretreated biomass was dried in a custom drying box and stored in plastic bags at room temperature until used.

## 5.2.4 High Solids Roller Bottle Enzymatic Hydrolysis

High solids roller bottle enzymatic hydrolysis experiments were optimized using AFEX pretreated corn stover at 6% and 9% glucan loading (g glucan/mL) by adjusting the following conditions: 1) phosphate buffer pH, 2) phosphate buffer concentration, and 3) centrifugation time. All hydrolysate samples were loaded in 85 mL Nalgene Oak Ridge centrifuge tubes, with a final working volume of 35 mL. The biomass was autoclaved at 121°C for 20 min to prevent microbial contamination. After the autoclave step, a designated volume of phosphate buffer (0.05 M, 0.1 M, 1.5 M or 2.0 M; and pH 3.0 or pH 4.5), consisting of monobasic and dibasic potassium phosphate, enzymes, and makeup water to account for the amount lost during autoclaving, was added to the centrifuge tubes inside a laminar flow hood. The centrifuge tubes were then sealed with caps, which had been sterilized with 10 vol% bleach solution prior to the experiment. Novozyme 22257 cellulase and Novozyme 22244 hemicellulase (Novozymes, Franklinton, NC, USA) were desalted using a disposable desalting column (Disposable PD-10 Desalting Columns, Cytiva, VWR Catalog. No. 95017-001) and analyzed for protein content using the Pierce™ BCA Protein Assay Kit (Pierce Biotechnology). Enzymes were loaded at 28 mg protein/g glucan, consisting of 70% cellulase and 30% hemicellulase (v/v). The sealed centrifuge tubes were placed on a laboratory scale bottle roller (Low Profile Roller, IBI Scientific, Low Profile Roller Lab Start-Up Kit) at 20 rpm inside a static incubator (VWR symphony™, 414004-626, Low temp./BOD Incubator) set at 50 °C. A single static roller can accommodate up to 10 centrifuge tubes. After 72 hours of enzymatic hydrolysis, the samples were centrifuged for various times at 12,000 rpm (18,500 x g) and 4 °C in a benchtop laboratory scale centrifuge (Eppendorf Benchtop 5804R Centrifuge). At a constant rotation speed of 12,000 rpm (18,500 x g), 6% glucan loading hydrolysates (0.1 M phosphate, pH 3.0) were centrifuged for 1 hr, 2 hr, or 5 hr. The 9% glucan loading hydrolysates were centrifuged at 12,000 rpm (18,500 x g) for 2 hr, 3 hr or 5 hr. The final pH of the supernatant was recorded for all the samples and then adjusted to a suitable pH for fermentation by either *Saccharomyces cerevisiae* or *Zymomonas mobilis*, 5.8 +/- 0.1, using 12 M HCl or 10 M NaOH. The pH adjusted hydrolysates were pre-filtered through 0.5 µm glass fiber filter paper (Metrigard®, 47 mm, Pall, VWR Catalog. No. 28150-371) in a 4.7 cm diameter Buchner funnel. This filtrate was then sterile filtered using a 0.22 µm, 50 mL Autofil sterile filtration system. The hydrolysate samples were collected in sterile polypropylene centrifuge tubes and stored at 4 °C until shipped on ice for subsequent fermentation experiments and characterization.

The effectiveness of the method was then tested on 6% glucan loading AFEX treated switchgrass from two different years of harvest (2010 and 2012), and sorghum, miscanthus, and restored prairie harvested in 2014 based on the optimized parameters for phosphate buffer pH (3.0) and phosphate buffer concentration (0.1 M). Centrifugation time of 1 hr. was sufficient for corn stover harvested in 2008, whereas 3 hr. centrifugation was required for the other feedstocks for proper solid-liquid separation. Therefore, the centrifugation time for the final method was 3 hr. For the field-to-fuel validation studies, 2010 and 2012 switchgrass pretreated in the smaller scale custom reactors were processed

using the same method, but at 7% glucan loading to match the conditions used in previous studies [20, 300]. All other hydrolysis conditions were identical.

### 5.2.5 High Solids Loading Enzymatic Hydrolysis-Shake Flask Method

The roller bottle enzymatic hydrolysis method was compared to the conventional shake flask method in batch mode. The experiments were conducted at 6% glucan loading, with 0.1 M phosphate buffer at pH 3.0 for 72 hours on AFEX pretreated corn stover (CS), sorghum (SOR), switchgrass (SG), miscanthus (MSC) and restored prairie (RP). The working volume for the flask method was 50 mL, as opposed to the 35 mL used in the roller bottle system. AFEX pretreated samples were added to previously autoclaved 100 mL Erlenmeyer flasks. The biomass was autoclaved at 121°C for 20 min to prevent microbial contamination and match the roller bottle method. After the autoclave step, a designated volume of 0.1 M phosphate buffer (pH 3.0) consisting of monobasic and dibasic potassium phosphate, enzymes (28 mg protein per g glucan – 70% cellulase and 30% hemicellulase), and makeup water to account for the amount lost during autoclaving, was added to the Erlenmeyer flasks inside a laminar flow hood. The Erlenmeyer flasks were then sealed with 27 mm diameter rubber stoppers, which had been autoclaved prior to the experiment. The sealed Erlenmeyer flasks were placed inside a shaker incubator (New Brunswick™ Excella® E25) at 150 rpm set at 50 °C. After 72 hours of enzymatic hydrolysis, the samples were centrifuged in 85 mL Nalgene Oak Ridge centrifuge tubes for 3 hours at 12,000 rpm (18,500 x g) and 4 °C in a benchtop laboratory scale centrifuge (Eppendorf Benchtop 5804R Centrifuge). The final pH of the supernatant was recorded for all the samples. The pH was then adjusted to the optimum pH for fermentation by either *Saccharomyces cerevisiae* or *Zymomonas mobilis*,  $5.8 \pm 0.1$ , using 12 M HCl or 10 M NaOH to ensure adequate pH for fermentation. The pH adjusted hydrolysates were pre-filtered through 0.5 µm glass fiber filter paper (Metrigard®, 47 mm, Pall, VWR Catalog. No. 28150-371,) in a 4.7 cm diameter Buchner funnel. This filtrate was then sterile filtered using a 0.22 µm, 50 mL Autofil sterile filtration system. The hydrolysate samples were collected in sterile polypropylene centrifuge tubes and stored at 4 °C until shipped on ice for subsequent fermentation experiments and characterization. The composition of glucose, xylose and other hydrolysate end products (Figure S1) were analyzed using HPLC-RID as described previously [65].

### 5.2.6 Fermentation

For the fermentation experiments, 5 mL of each hydrolysate were pipetted into sterile serum bottles and degassed overnight in an anaerobic chamber. A culture of either *Z. mobilis* ZM2032 [301] or *S. cerevisiae* GLBRCY945 [302] was grown overnight and diluted into anaerobic media the day of the experiment. Once the cultures reached logarithmic growth, they were centrifuged, and cell pellets were resuspended with synthetic medium [300], and inoculated into 60 mL Wheaton serum bottles. The serum bottles were capped with airtight Chemglass Life Sciences Blue Butyl, 20mm rubber caps and placed on a 120 rpm shaker in a 30 °C environmental growth chamber. The cultures were attached to respirometer cartridges using BD PrecisionGlide 23GX1 (0.6mm X

25mm) sterile needles inserted into the serum bottle caps. The respirometer (AER-800; Challenge Technology; Springdale, AR, USA) measured the volume of gas produced by the growing culture. Each experiment was run for 48 hr, unless stated otherwise. Supernatants from post-fermentation cultures were analyzed by high performance liquid chromatography (HPLC) and refractive index detection (RID) for sugar and ethanol concentrations [65]. Final cell density (OD600) measurements were made with a Beckman DU720 spectrophotometer.

## 5.2.7 Calculations:

### 5.2.7.1 *Extent of liquefaction:*

Following centrifugation and decantation of the samples, the extent of liquefaction was calculated as:

$$\text{Extent of liquefaction} = \frac{\text{Volume of supernatant following centrifugation and filtration}}{\text{Initial working volume of the sample}}$$

[303].

### 5.2.7.2 *Glucan conversion:*

*Glucan conversion (g glucose released per g glucose in untreated dry biomass)*

$$= \frac{\text{glucose measured by HPLC} \left(\frac{g}{L}\right)}{1000 \times \text{glucan loading \%}} \times \frac{162.14}{180.16}$$

Where  $MW_{\text{glucose}} = (180.16 \text{ g/mol})$  and  $MW_{\text{glucan}} = (162.14 \text{ g/mol})$

### 5.2.7.3 *Glucose yield:*

Glucose yield was calculated as described previously [114]

*Glucose yield (mg glucose released per g glucose in untreated dry biomass)*

$$= \frac{\text{glucose measured by HPLC} \left(\frac{g}{L}\right)}{1000 \times \text{glucan loading \%}} \times \frac{162.14}{180.16} \times V_a$$

Where  $MW_{\text{glucose}} = (180.16 \text{ g/mol})$  and  $MW_{\text{glucan}} = (162.14 \text{ g/mol})$  and  $V_a$  is the available volume of the hydrolysate.

### 5.2.7.4 *Xylan conversion:*

*Xylan conversion (g xylose released per g xylose in untreated dry biomass)*

$$= \frac{\text{xylose measured by HPLC} \left(\frac{g}{L}\right)}{1000 \times \text{glucan loading } \%} \times \frac{\% \text{ glucan content per g untreated biomass}}{\% \text{ xylan content per g untreated biomass}} \times \frac{132}{150}$$

Where  $MW_{xylose} = (150 \text{ g/mol})$  and  $MW_{xylan} = (132 \text{ g/mol})$

#### **5.2.7.5 Xylose yield:**

Xylose yield was calculated as follows:

*Xylose yield (mg xylose released per g xylose in untreated dry biomass)*

$$= \frac{\text{xylose measured by HPLC} \left(\frac{g}{L}\right)}{1000 \times \text{glucan loading } \%} \times \frac{\% \text{ glucan content per g untreated biomass}}{\% \text{ xylan content per g untreated biomass}} \times \frac{132}{150} \times V_a$$

Where  $MW_{xylose} = (150 \text{ g/mol})$  and  $MW_{xylan} = (132 \text{ g/mol})$  and  $V_a$  is the extent of liquefaction.

#### **5.2.7.6 Ethanol yield:**

Ethanol yield was calculated as follows [85]

$$\text{Ethanol yield (\% of theoretical)} = \frac{\text{ethanol measured by HPLC} \left(\frac{g}{L}\right)}{\left(\text{glucose} \left(\frac{g}{L}\right) + \text{xylose} \left(\frac{g}{L}\right)\right) \text{consumed} \times 0.51} \times 100\%$$

Where the theoretical maximum yield of ethanol from both glucose and xylose is 0.51 g ethanol produced per g sugar consumed.

## **5.3 Results**

### **5.3.1 Feedstocks and pretreatment**

Correlating environmental field conditions to effects on feedstock deconstruction and fuel production will require analysis of a large number of samples that control for multiple variables (e.g., local temperature and precipitation, soil type and field location). This study used a variety of potential herbaceous bioenergy feedstocks (corn stover, switchgrass, sorghum, restored prairie, and miscanthus), to demonstrate the broad utility of the platform. The majority of feedstocks in this study were pretreated in a larger Parr reactor, in order to have a consistent supply of feedstock for developing the enzymatic hydrolysis method. However, the actual pipeline makes use of smaller custom AFEX reactors that can pretreat 25 g of lignocellulosic biomass per batch [77]. Once the

hydrolysis method was finalized, the custom reactors were used to process two feedstocks with previously observed divergent fermentations and validate the method.

### 5.3.2 Enzymatic hydrolysis buffer pH and concentration influences sugar release and fermentability of the hydrolysates

Common hydrolysis bottlenecks in shake flasks at high solids loading include insufficient shear rate, improper enzyme distribution, and inadequate mixing due to accumulation of biomass near the walls. A laboratory scale roller bottle hydrolysis method was developed in order to overcome these bottlenecks. Hydrolysate pH significantly affects liquefaction and sugar yields due to its influence on enzyme activity. The enzymes used in our study were from Novozymes Ctec and Htec series, which have cellulase, hemicellulase, xylanase, and betaglucosidase activities [304-306]. The activities of our cellulolytic enzymes have an optimal pH range of 5.0 to 5.5 [307]. However, AFEX pretreated biomass when stored in liquid water (either before or after autoclaving) has a pH of ~7, which means a pH adjustment step is necessary for effective enzymatic activity. We initially tested pH control by adding HCl following autoclaving. However, because of the variability between feedstocks, it was difficult to estimate the amount of HCl required to reach the desired pH, which meant that pH adjustment became a long and laborious process. For a platform that was intended to work on hundreds of feedstocks with unknown native buffering capacity, it was decided that this approach was impractical. Instead, we decided to adjust pH using phosphate buffer, which was chosen based on its use in a previous study on fermentation of AFEX hydrolysates [308].

The effect of buffer pH and concentration on hydrolysate characteristics were evaluated using 6% glucan loading (19% w/w solids loading) AFEX corn stover hydrolysates. The final hydrolysate pH was lower for pH 3.0 buffer compared to 4.5, and for all concentrations except 0.2 M (**Figure 5.1A**). While the pH 4.5 buffer showed an effect of concentration on final hydrolysate pH, this was not observed for the pH 3.0 buffer, which had a consistent final pH of ~5.75 regardless of buffer concentration. All hydrolysates had a pH ranging between 5.75 and 6.0, which was slightly higher than optimal enzyme activity, but in a suitable range for *Z. mobilis* fermentations, which meant that less pH adjustment was required following enzymatic hydrolysis. Although the hydrolysate pH was not strongly affected by buffer concentration and pH, both of these properties affected carbohydrate conversion and the fermentability of the hydrolysates (**Figure 5.1**), with the glucose conversion consistently higher for a buffer pH of 3.0 than 4.5. The highest glucose conversion was attained for the buffer concentration of 0.15 M and pH of 3.0 (**Figure 5.1A**).

Since the addition of phosphate buffer could have downstream effects on the fermentation microbes, we next sought to determine the effect of buffer concentration and pH added during enzymatic hydrolysis on subsequent microbial fermentation. First, the high solids loading hydrolysates were adjusted to pH  $5.8 \pm 0.1$ , which was suitable for fermentation by both *S. cerevisiae* and *Z. mobilis*. Engineered *S. cerevisiae* and *Z. mobilis* strains were then inoculated into sealed serum bottles containing various hydrolysates,

grown at 30 °C for two days and sampled for final ethanol and sugar concentrations. The ethanol concentrations at the end of fermentation were not dependent on buffer concentration, which for the same buffer pH were very similar (**Figure 5.2A**). In contrast, ethanol concentrations were consistently higher for a buffer pH of 3.0 than 4.5 for both *S. cerevisiae* and *Z. mobilis* (**Figure 5.2A**). For *Z. mobilis*, this appears to be entirely related to increased sugar concentrations in the hydrolysates, as the ethanol yields were very similar across all buffers (**Figure 5.2B**). In contrast, the ethanol yields obtained for *S. cerevisiae* were slightly higher for the hydrolysate generated using the pH 4.5 buffer (**Figure 5.2C**) indicating that though less ethanol was produced (**Figure 5.2A**), the yeast was more efficient than *Z. mobilis* at converting sugars to ethanol.



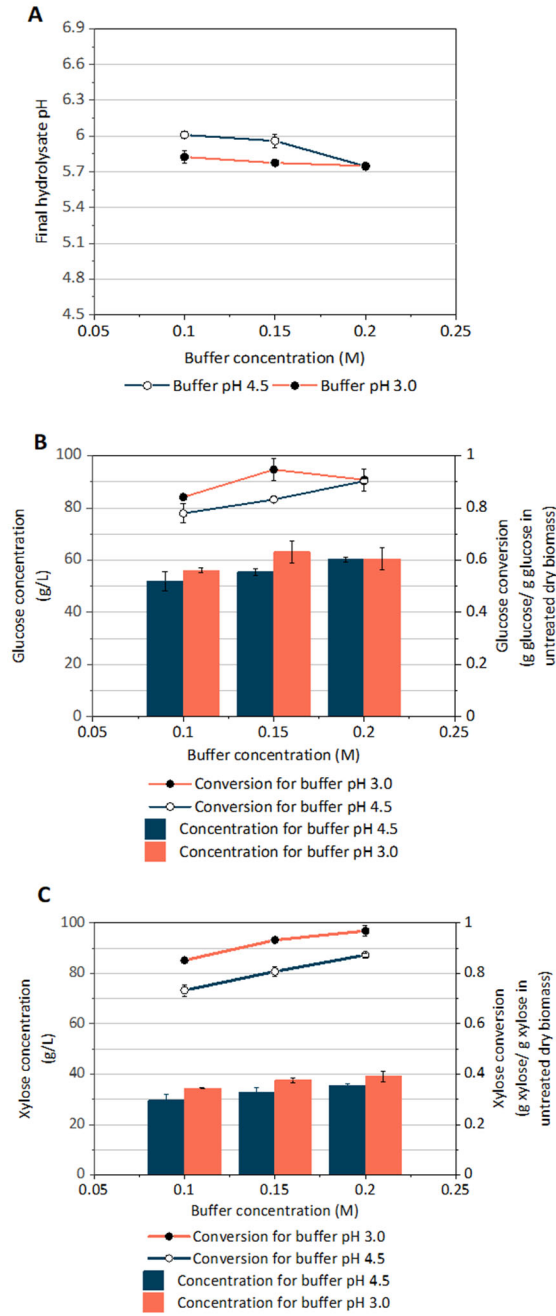


**Figure 5.1. A) Increasing buffer pH and concentration decreased hydrolysate final pH. B) Increasing buffer pH (3.0 to 4.5) and concentration (0.1 to 0.2 M) increased glucose conversion and glucose concentration for AFEX pretreated CS at 6% glucan loading. C) Increasing buffer pH (3.0 to 4.5) and concentration (0.1 to 0.2 M) increased xylose conversion and xylose concentration for AFEX pretreated CS at 6% glucan loading for buffer pH 3.0 and 4.5. Values for all subfigures are reported as the mean  $\pm$  SD, n=2.**

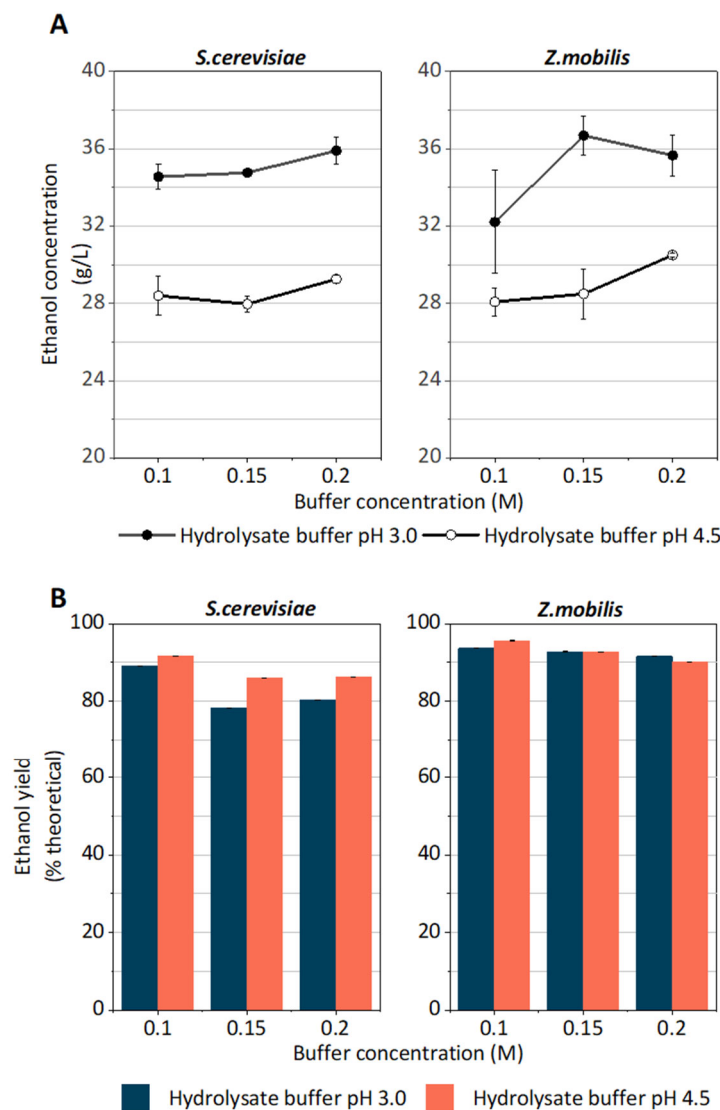


**Figure 5.2.** A) Ethanol concentration was more affected by buffer pH (3.0 > 4.5) than concentration for both *S. cerevisiae* and *Z. mobilis* in 6% glucan loading hydrolysate. B) Ethanol yield was not affected significantly by hydrolysate buffer pH. For both *S. cerevisiae* and *Z. mobilis*, while the yields were higher at a lower buffer concentration for both cases. All hydrolysates were made from AFEX pretreated CS at 6% glucan loading. All fermentations were conducted at a pH of  $5.8 \pm 0.1$ . Values for all subfigures are reported as the mean  $\pm$  SD, n=2.

### 5.3.3 Sugar yields decline with increasing solids loading due to low water availability for liquefaction.

Enzymatic hydrolysis was carried out on AFEX pretreated corn stover at 6% and 9% glucan loading (19% and 28% w/w solids loading, respectively) in roller bottles to evaluate the effect of solids loading on hydrolysate characteristics and optimum processing conditions. For the same buffer concentrations and buffer pH, 6% glucan

loading showed more consistent liquefaction (**Figure 5.3A**), and higher glucose and xylose conversions compared to 9% glucan loading (**Figure 5.3B, 5.3C**). The glucose and xylose conversion were about 36% higher for 6% glucan loading compared to 9% glucan loading. The highest sugar conversions were obtained using the 0.2 M, pH 3.0 buffer for both solids loadings, with the exception of the 6% glucan hydrolysate, where glucose conversion was highest for the 0.15 M, pH 3.0 buffer (**Figure 5.3**). An additional 5 mL was recovered from 6% glucan loading hydrolysates compared to the higher solids loading, though the volume did not vary significantly for the same solid loading across the reported centrifugation times. The 9% glucan loading samples were unable to be fully filtered by the dual stage filtration (0.5  $\mu\text{m}$  pre-filtration followed by 0.22  $\mu\text{m}$  sterile filtration) for centrifugation times less than 2 hr, which is the reason for the difference in centrifugation times between the two solids loadings (**Figure 5.3A**).

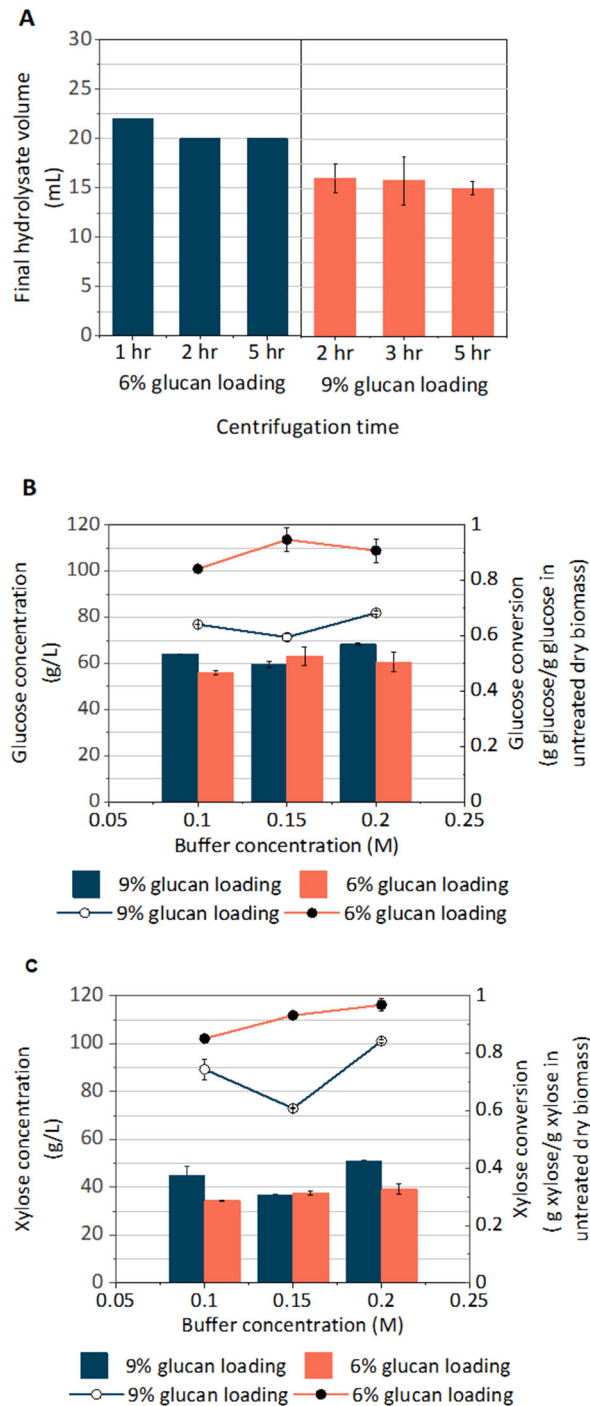


**Figure 5.3.** A) 6% glucan loading produced higher volume of hydrolysate than 9% glucan loading for all centrifugation times. Also, the volume of hydrolysate was not affected by the centrifugation times. B) Although the glucose concentrations were similar for both solids loading conditions, the glucose conversion was higher for 6% glucan loading than 9% glucan loading for all buffer concentrations. C) Xylose conversion was higher for 6% glucan loading than 9% glucan loading for all buffer concentrations. Values for all subfigures are reported as the mean  $\pm$  SD, n=2.

### 5.3.4 Enzymatic hydrolysis in roller bottles led to greater liquefaction and higher sugar yields compared to shake flasks

In order to validate the roller bottle enzymatic hydrolysis method, it was compared to enzymatic hydrolysis in shake flasks for a variety of herbaceous feedstocks (corn stover, switchgrass, sorghum, miscanthus, and native prairie). Roller bottle and shake flask experiments were conducted using the same conditions used previously at 6% glucan loading (15 - 22% w/w solids loading, depending on the feedstock). However, shake flasks had a greater working volume (50 mL in shake flask experiments compared to 35 mL for roller bottle experiments). In spite of this, the final hydrolysate volumes for the shake flask and roller bottle experiments were similar (Error! Reference source not found.**A**) and the extent of liquefaction, which is the ratio of final hydrolysate volume and working volume (Error! Reference source not found.**B**), was 42-47% higher for the roller bottle method for all feedstocks tested. A previously developed scalable roller bottle method for 20% (w/w) solids loading concluded that gravitational tumbling overcame the important bottlenecks of improper mixing and high viscosity when compared to the shake flask method with intermittent hand mixing [102], which agrees with our results.

As expected from the greater extent of liquefaction, the glucose and xylose yield for the hydrolysates from the roller bottle method were ~25-50% higher than the shake flask method for all the AFEX pretreated feedstocks (Error! Reference source not found.**A**, **5.5B**), though the hydrolysate sugar concentrations were similar for both methods (Error! Reference source not found.**C**, **5.5D**). This indicates that although both methods seem to provide hydrolysate of similar quality from the same feedstock for fermentation, the roller bottle system facilitates greater conversion in the same amount of time and because of this generates greater usable hydrolysate volumes.

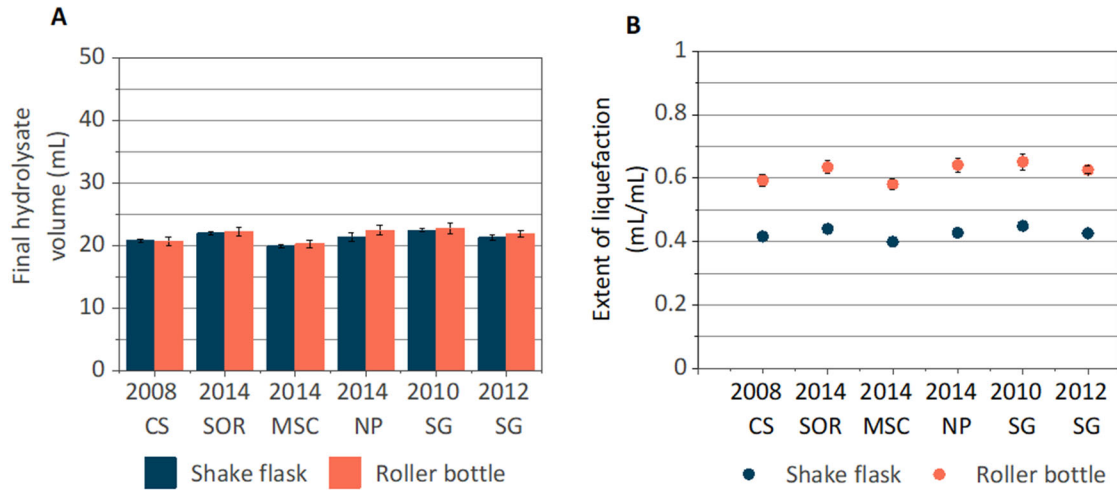


**Figure 5.4. Roller bottle enzymatic hydrolysis achieves better liquefaction than the shake flask method, with equivalent final hydrolysate volumes despite different starting hydrolysis volumes. A) Final hydrolysate volumes are similar for roller bottle and shake flask hydrolysis. B) Extent of liquefaction is greater for roller bottle enzymatic hydrolysis. CS = corn stover, SOR = sorghum, MSC = miscanthus, NP = native prairie, SG = switchgrass. Numbers refer to the biomass harvest year. Values for all subfigures are reported as the mean  $\pm$  SD, n=2. Values for all subfigures are reported as the mean  $\pm$  SD, n=2.**

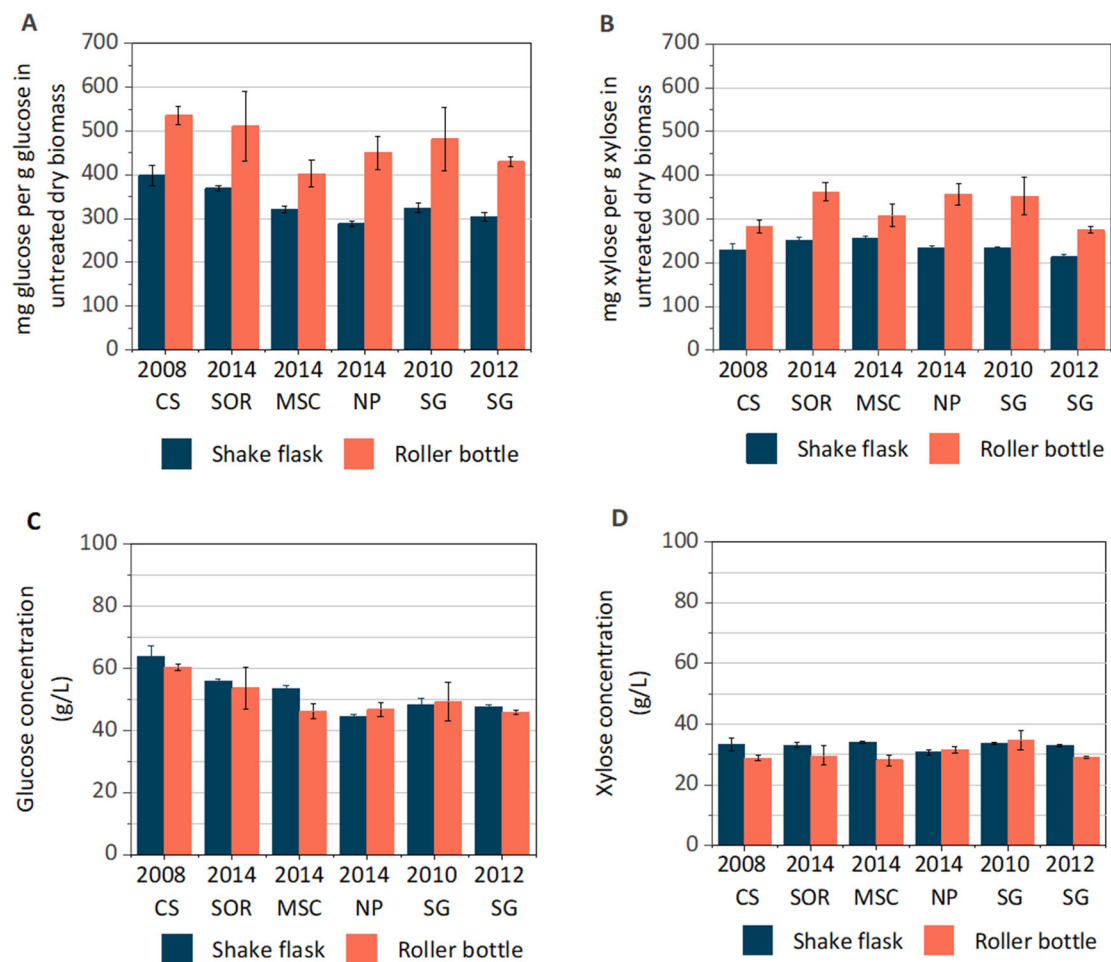


**Figure 5.5.** A) Glucose yield was higher for the roller bottle hydrolysates than the shake flask hydrolysates for all the feedstocks. B) Xylose yield was higher for the roller bottle hydrolysates than the shake flask hydrolysates. C) Hydrolysate glucose concentration was similar for both roller bottle and shake flask samples. D) Hydrolysate xylose concentration was similar for both roller bottle and shake flask samples. CS = corn stover, SOR = sorghum, MSC = miscanthus, NP = native prairie, SG = switchgrass. Numbers refer to the biomass harvest year. Values for all subfigures are reported as the mean  $\pm$  SD, n=2. Values for all subfigures are reported as the mean  $\pm$  SD, n=2.

We next compared the diverse hydrolysates generated by the roller bottle and shake flask hydrolysis in microbial fermentation experiments. Standard flask fermentations with yeast or bacteria typically require 10-20 mL of medium because a significant amount of culture volume is depleted from cell density (e.g., OD600 measurements) and extracellular metabolite (e.g., ethanol titer as determined by HPLC-RID) sampling. Since we obtain only 20-25 mL of hydrolysate from both roller bottle and shake flask protocols, we investigated alternative methods of fermentation that utilize low (5 mL or less) volumes of hydrolysates, which will allow the remaining volume to be used for additional studies. Since CO<sub>2</sub> is formed as a byproduct during the anaerobic fermentation of glucose to ethanol ( $C_6H_{12}O_6 \rightarrow 2 C_2H_5OH + 2CO_2 + 2ATP$ ), others have monitored fermentative CO<sub>2</sub> production from the vessel headspace as a proxy for ethanol production [309, 310].

We developed a protocol that employs a commercial respirometer system that measures and records CO<sub>2</sub> production in real time. Serum bottles containing 5 mL of paired hydrolysates generated from roller bottles or shake flasks were inoculated with yeast *S. cerevisiae* or bacteria *Z. mobilis*. The serum bottles were connected to a commercially available respirometer system that measures CO<sub>2</sub> production by tracking disruption of a laser beam by bubbles released from the flasks. CO<sub>2</sub> production was measured for approximately 48 hours, at the end of which time final cell density and extracellular metabolite samples were taken for analysis. The data from the paired samples were subtracted to give an idea of general trends in fermentation performance between the two experimental methods. Interestingly, only the shake flask experiments had significantly inhibited fermentations that did not achieve maximum CO<sub>2</sub> production by the end of the ~40 hr fermentation period (Error! Reference source not found.). This is indicated by the positive data points for the roller bottle glucose consumption (Error! Reference source not found.). These values were high because the shake flask experiments for these paired samples had incomplete glucose consumption after ~40 hr, while for all other experiments, 100% of the glucose was consumed (Table 9.2-2 and Table 9.2-3).

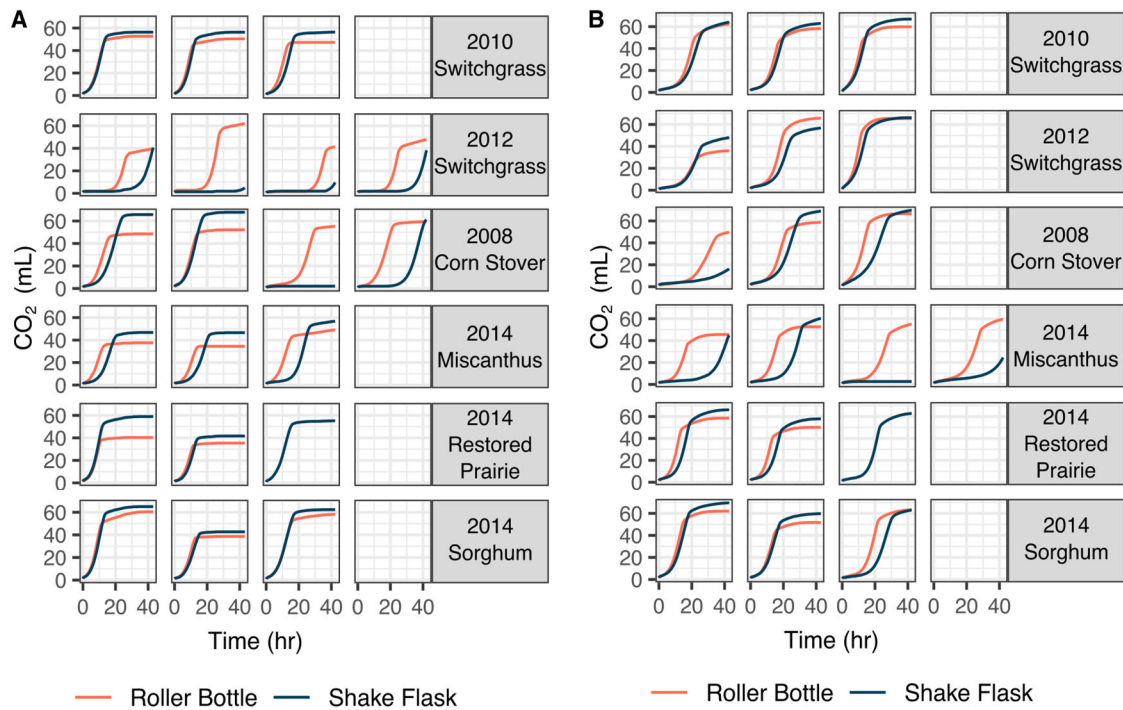


**Figure 5.6. CO<sub>2</sub> production by A) *S. cerevisiae* Y945 and B) *Z. mobilis* 2032 show some feedstock-specific differences during fermentation of hydrolysates generated in roller bottles or shake flasks. For each feedstock, columns represent separate paired replicates, where the two fermentations (shake flask and roller bottle system) were run simultaneously. (Plots in the same column across feedstocks were not necessarily run in the same batch of fermentations.)**



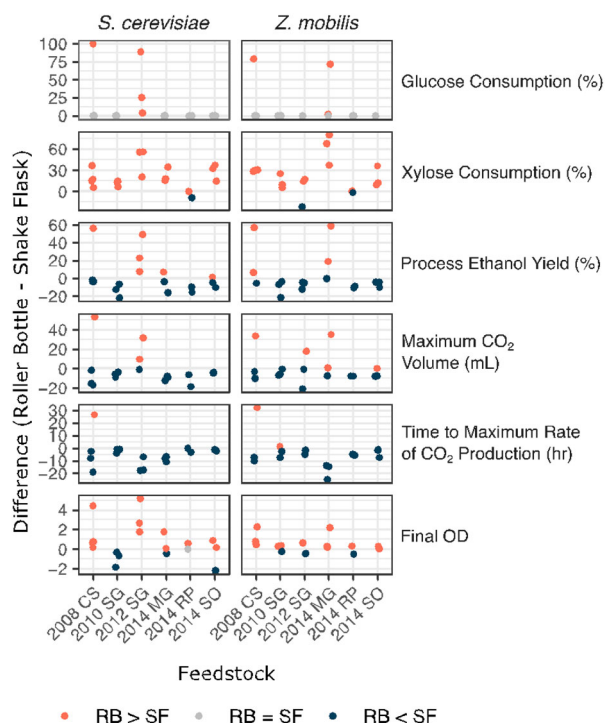


**Figure 5.7. Max CO<sub>2</sub> volume is correlated with the final volume of ethanol produced during fermentation for both *S. cerevisiae* Y945 and *Z. mobilis* ZM2032. Samples are 6% glucan loading hydrolysates produced using the roller bottle and shake flasks from all five grass feedstocks that had been pretreated in the 5-gallon reactor (2008 corn stover, 2010 and 2012 switchgrass, and 2014 miscanthus, native prairie, and sorghum).**

In general, xylose consumption and final OD tended to be higher in fermentations with roller bottle hydrolysates, while process ethanol yield (amount of ethanol produced with respect to the theoretical maximum based on hydrolysate composition), maximum CO<sub>2</sub> volume, and time to maximum rate of CO<sub>2</sub> production were higher for shake flask experiments. The time to maximum rate of CO<sub>2</sub> production gives an indication of delay in fermentation, with longer times for the shake flask experiments indicating slower and more inhibited fermentations. The few samples that did not follow these trends (the positive values in the respective plots in Error! Reference source not found.) were generally for the severely inhibited shake flask fermentations.

### 5.3.5 The Field-to-Fuel Platform successfully replicates fermentation results observed in larger scale experiments

Because hydrolysate composition is related to fermentation performance, we determined correlations between key fermentation results and hydrolysate sugars, alcohols, and organic acids (Error! Reference source not found. and **Figure 9.6**). For the most part, the compounds quantified in the hydrolysates were not correlated with key fermentation metrics, for either *S. cerevisiae* (Error! Reference source not found.) or *Z. mobilis*

(Figure 9.6) fermentations. Fermentation data tended to cluster together, and hydrolysate composition data tended to cluster together in the correlation plots. For the hydrolysate composition data, acetate, glucose, glycerol, and succinate concentrations were positively correlated across all feedstocks. The fermentation data showed strong positive correlations between glucose consumption (titer and percentage basis), process ethanol yield (amount of ethanol generated compared to the theoretical maximum), total ethanol produced, final cell density, maximum CO<sub>2</sub> volume, and maximum rate of CO<sub>2</sub> production.

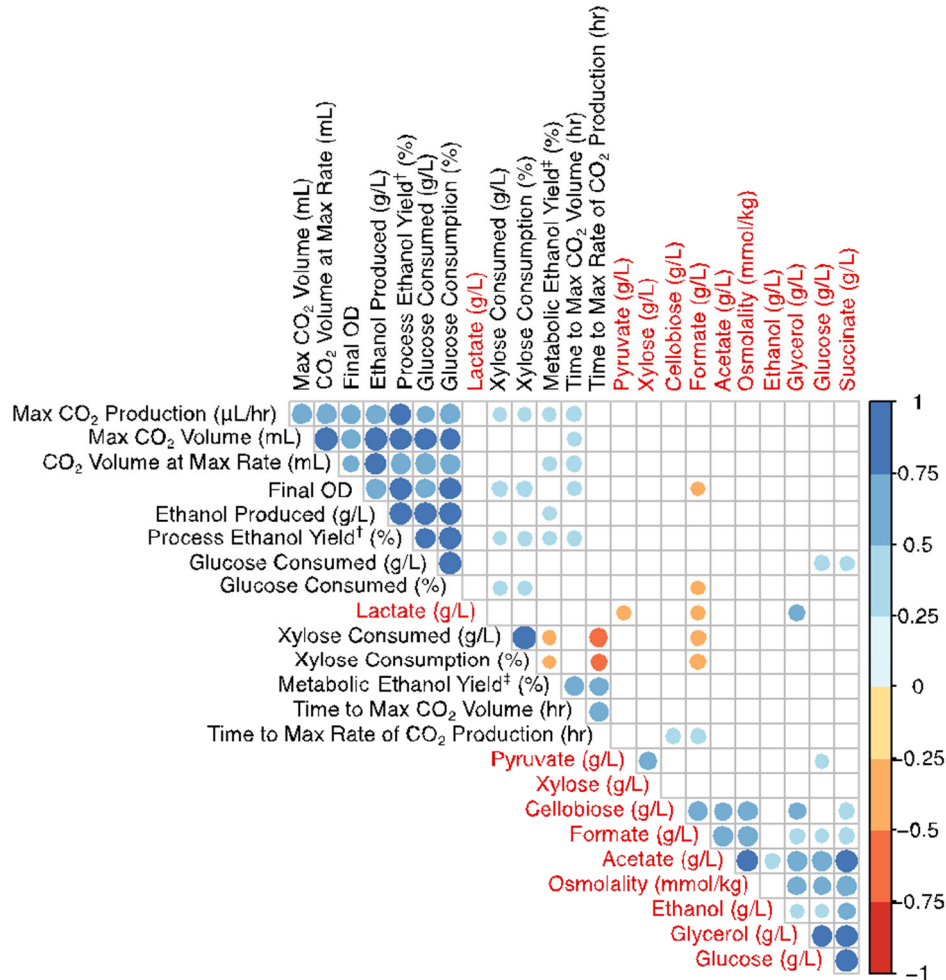
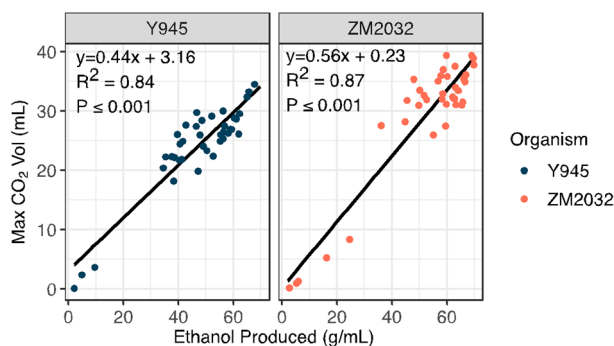


Figure 5.8. Clustered correlation matrix for *S. cerevisiae* Y945 fermentation data (black labels) and hydrolysate composition (red text labels). The plot was generated using the corrplot package in R with hclust (hierarchical clustering order). The size and color correspond to the direction and magnitude of the correlation. Correlations that were insignificant ( $p > 0.05$ ) were not plotted. <sup>†</sup>The process ethanol yield is the ratio of sugars initially present in the hydrolysate (glucose and xylose) to ethanol produced assuming 0.51 g ethanol/g sugars as the theoretical maximum. <sup>‡</sup>The metabolic yield is the ratio of sugars (glucose and xylose) consumed during fermentation to ethanol produced assuming 0.51 g ethanol/g sugars as the theoretical maximum.

Because the respirometer system measures CO<sub>2</sub> volume as a proxy for ethanol yield, the strong correlation between the two values lends support for the utility of the method. When the two values are plotted, there is a strong positive correlation between the maximum CO<sub>2</sub> volume and ethanol yield ( $p \leq 0.01$ ,  $R^2 = 0.84$  or  $0.87$ ), however, for productive fermentations, there is a large amount of scatter for the correlation between max CO<sub>2</sub> volume and ethanol concentration for the 6% glucan loading hydrolysates (Error! Reference source not found.). In spite of this, unusually low final CO<sub>2</sub> volumes corresponded very closely with low ethanol concentrations in the fermentation media (Error! Reference source not found.), indicating that CO<sub>2</sub> is an adequate surrogate for ethanol production when used to identify severely inhibited fermentations.



**Figure 5.9. Max CO<sub>2</sub> volume is correlated with the final volume of ethanol produced during fermentation for both *S. cerevisiae* Y945 and *Z. mobilis* ZM2032. Samples are 6% glucan loading hydrolysates produced using the roller bottle and shake flasks from all five grass feedstocks that had been pretreated in the 5-gallon reactor (2008 corn stover, 2010 and 2012 switchgrass, and 2014 miscanthus, native prairie, and sorghum).**

We also used the pipeline to process two feedstocks, switchgrass grown in a drought year – 2012, and switchgrass grown in a year with normal precipitation – 2010, which had previously shown strongly divergent yeast fermentation performance. These materials were pretreated in the custom AFEX reactors, hydrolyzed in the roller bottle system at 7% glucan loading (the same loading as previously published [20]), and conducted fermentation in the respirometer. Based on these experiments, switchgrass grown in a drought year (2012) was significantly more inhibitory to yeast fermentation compared to switchgrass grown in a normal year (2010) (Error! Reference source not found.). Although not all fermentations showed the complete inhibition of growth in the drought year switchgrass that was previously observed [20], all of the drought year samples had either significantly reduced or delayed CO<sub>2</sub> production compared to their paired fermentation sample from the year with normal precipitation.

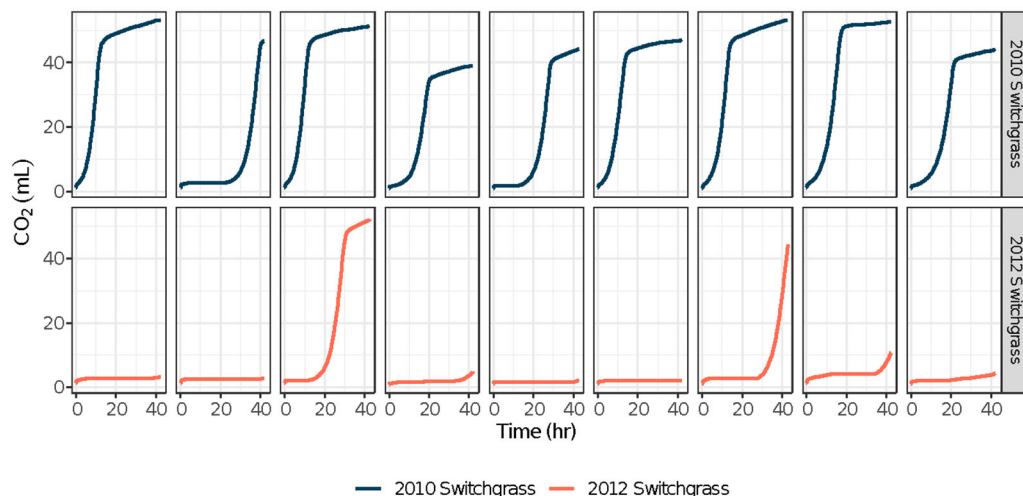


**Figure 5.10. *Saccharomyces cerevisiae* grown in drought year (2012) switchgrass hydrolysates showed significantly reduced or delayed CO<sub>2</sub> production compared to when it was grown in 2010 switchgrass hydrolysates from a year with normal precipitation. Each graph represents a separate batch of hydrolysate and each column represents paired replicates that were fermented in the same respirometer experiment.**

## 5.4 Discussion

Feedstocks across multiple plots and locations need to be studied to correlate the effects of environmental factors on biofuel production. The high throughput required for such studies led to the need for a field-to-fuel research pipeline, combining pretreatment, enzymatic hydrolysis, and fermentation. For biomass pretreatment, we previously designed and constructed a customized system that can AFEX pretreat as little as 25 g of biomass [77]. The ability to process biomass in smaller quantities under process conditions that are similar to the previously used Parr reactor system [20], makes the custom reactor suitable for the field-to-fuel research pipeline. The glucose and xylose concentrations after enzymatic hydrolysis for the AFEX pretreated biomass using the customized system are comparable to the results obtained for the biomass processed in the 5-gallon Parr reactor system [24, 77]. The 2010 and 2012 harvested switchgrass that were used for the final validation (Error! Reference source not found.) were pretreated in these custom AFEX reactors.

While several methods for enzymatic hydrolysis have been developed, they are less amenable for high solids loading with limited biomass quantity. High viscosity, product inhibition, low water availability, accumulation of oligosaccharides and inhibition of enzyme adsorption are some of the most important reasons for low sugar conversion during enzymatic hydrolysis of lignocellulosic biomass at high solids loading, especially in stirred tank reactors and laboratory scale shake flask reactors [290, 291, 311]. Horizontal bioreactors have achieved faster liquefaction through effective mixing of substrate and enzymes, which was evident through the drastic decrease in viscosity at high solids loading when compared to shake flask [117, 312]. A 2L horizontal bioreactor

designed for high solid loadings has shown enhanced biomass liquefaction and glucose yields up to 97.99% for 25% and 30% w/v solids loading, which is comparable to our results 94.6% glucose yield obtained for the roller bottle method at 6% glucan loading [292]. Lower efficiency enzymatic hydrolysis leads to lower volumes of hydrolysate and final products after microbial fermentation [303]. Liquefaction during high solids enzymatic saccharification has been a predominant method to evaluate the deconstruction of lignocellulosic biomass. Horizontal mixing in the roller bottle method has been shown to overcome the liquefaction problem in shake flasks at high solids loading, increasing sugar conversion and liquefaction, while generating hydrolysates with similar sugar composition. A previously studied 1.7 L horizontal rotating reactor at 25% w/w solids loading for steam pretreated corn stover was able to provide 20% higher saccharification when compared to a vertical stirred tank reactor [293]. In our study, liquefaction was about 45% higher for the roller bottle method than the shake flask method, consistently producing higher volumes of fermentable hydrolysates from AFEX pretreated biomass. One alternative route for improved hydrolysis performance in shake flasks is to load samples in fed batch. However, our process follows a strict protocol to maintain aseptic conditions and prevent microbial contamination, as has been observed to be an issue in other studies [300]. Fed batch addition of biomass is incompatible with these methods, and for this reason, we were not able to use a fed batch approach.

The effect of solids loading on enzymatic hydrolysis on the hydrolysate composition were compared for corn stover at 6% and 9% glucan loading (19% and 28% w/w solids loading) during process optimization. Our results (**Figure 5.3A, 5.3B**) are consistent with a previous work on dilute acid pretreated corn stover loaded at 5%, 10% and 15% w/w solids loading, where the highest glucan conversion was observed for 5% solids loading [295]. Similarly, for an increase in solids loading from 2% to 5% for steam pretreated softwood resulted in a 16% decreasing of carbohydrate conversion [313]. Glucose conversions are known to decrease with increasing solids loading [100]. This is attributed to both end product inhibition of enzymes and accumulation of oligosaccharides at high solids loading [115, 311]. We observed that liquefaction and sugar release was higher for 6% glucan loading compared to 9% glucan loading. The availability of initial free liquid at the beginning of the enzymatic hydrolysis could account for the better liquefaction at 6% glucan loading. For 9% glucan loading, the water added to the pretreated biomass was absorbed completely by the biomass and consequently, no initial free liquid was available, which may have caused slower deconstruction of the pretreated biomass, as seen elsewhere [104, 108].

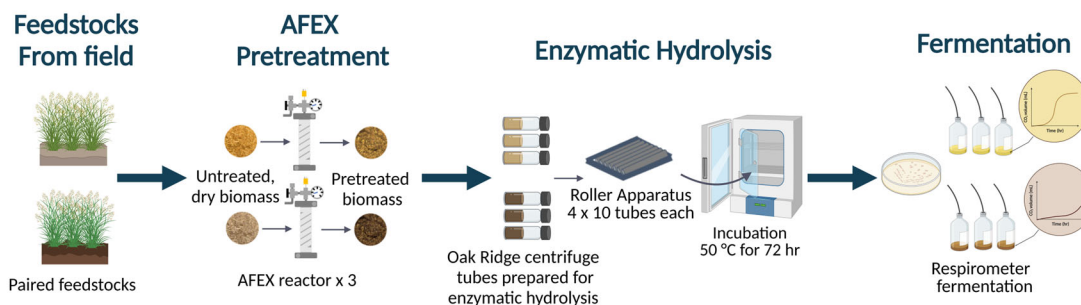


**Figure 5.11. Process flowchart for the field-to-fuel platform including small scale AFEX pretreatment, roller bottle enzymatic hydrolysis and respirometer fermentation using *S. cerevisiae* and *Z. mobilis*. Created with BioRender.com.**

A major goal of our platform (**Figure 5.11**) is to rapidly compare environmentally-challenged feedstock samples to determine the impact on fermentation compared to the general population, and use this to identify contributing biomass environmental, agronomic, or genetic factors. While ethanol is the desired product, it is challenging to monitor ethanol concentrations at informative time resolution from low culture volumes. Using CO<sub>2</sub> production as a surrogate for ethanol production is one way to monitor fermentation progress real-time, while avoiding issues with sampling and disturbing the fermentation process. Our research pipeline showed some correlation between final ethanol titer and maximum CO<sub>2</sub> production in fermentations of multiple feedstocks, and accurately represent differences in growth and fermentation across paired samples, particularly when inhibitory hydrolysates are compared (e.g., 2012 drought versus 2010 normal year switchgrass). When comparing the fermentability of hydrolysates generated using the roller bottle and shake flask methods, in general, the shake flask hydrolysates were more inhibited based on the longer time required to reach exponential CO<sub>2</sub> production and lower final cell density, and some samples were unable to fully utilize all of the glucose by the end of the ~40 hr fermentation period. Though slower, the fermentations using the shake flask hydrolysates tended to have greater CO<sub>2</sub> and ethanol production compared to their paired roller bottle hydrolysates. Interestingly, the xylose consumption was also lower in the shake flask hydrolysates, which is opposite the trend observed for diverse feedstocks, where greater xylose consumption tends to correlate with a higher process ethanol yield [24, 314]. The process ethanol yield for diverse feedstocks were similar with a few exceptions for the roller bottle hydrolysates, which is the same trend as observed in the previous study, in which the hydrolysates were generated in a 3 L Applikon ez-control bioreactor system (Applikon Biotechnology, Foster City, CA, USA) [24]. Ultimately, by using our small-scale pretreatment, roller bottle enzymatic hydrolysis at optimal conditions, and monitoring CO<sub>2</sub> production during fermentation, we were able to replicate the results previously observed [20] showing significant, replicated inhibition of drought year switchgrass with respect to the control switchgrass. Inhibitory hydrolysates could be targeted for more detailed analysis, such as chemical genomics studies [315, 316] or scaled up experiments in bioreactors. Therefore, the field-to-fuel research pipeline can be used to compare multiple samples from across the field for statistical confidence.

## **5.5 Conclusion**

This study has demonstrated that the roller bottle system is able to better overcome the major bottlenecks of poor mixing, inadequate availability of water and viscous nature of pretreated biomass compared to the shake flask method, for a variety of grass-based AFEX-pretreated feedstocks [109]. When the entire field-to-fuel platform was used, combining moderate scale pretreatment, roller bottle enzymatic hydrolysis, and respirometer fermentation, we were able to replicate the fermentation differences from limited volumes of hydrolysates from 2012 switchgrass grown in a drought year compared to 2010 switchgrass grown under normal precipitation. This method can be utilized to compare an array of feedstocks and different process conditions.

## **5.6 Funding**

This work was funded by the DOE Great Lakes Bioenergy Research Center (DOE BER Office of Science DE-FC02-07ER64494).

## **5.7 Acknowledgments**

We gratefully acknowledge Novozymes generous support for providing the enzymes used during enzymatic hydrolysis. We thank J. Sustachek, A. Miller, Z. Andersen, B. Faust, and J. Tesmer for collection and processing of biomass; C. Donald Jr., J. Cassidy, and L. Hooker-Moericke for conducting AFEX pretreatment; M. Kreuger, M. Shabani, and C. Gunawan for biomass composition analysis; M. McGee and Metabolomics Core for HPLC analysis of enzymatic hydrolysis and fermentation products; and Mary Tremaine, Jose Serate, Dan Xie and Yaoping Zhang for technical support with fermentation.

## 6 CONCLUSION

### 6.1 Microfluidic imaging reactor (Chapter Error! Reference source not found.)

Pretreatment and enzymatic hydrolysis of a thin corn stem section were successfully visualized using CLSM at different time points with a custom microfluidic imaging reactor constructed using photolithographic techniques. Sufficient pretreatment supernatants and hydrolysates were obtained to evaluate sugar release during the experiments. The parenchyma cells were more susceptible to degradation than the cell types in the vascular bundles during both acid and alkali pretreatment. The protoxylem cell walls were the most resistant, remaining intact after 48 hours of enzymatic hydrolysis after all the other cell types had disintegrated. Arabinoxylan localization using LM11 monoclonal antibody indicated a uniform removal of hemicellulose for all cell types following dilute acid pretreatment and indicates the compatibility of the imaging reactor with antibody labeling. Some of the limitations of the reactor are that it cannot be pressurized, the temperature is limited to 100 °C, and once contained in the reactor, the solid biomass is inaccessible for further characterization. However, in spite of these limitations, the reactor is able to successfully evaluate the same plant material through all stages of pretreatment and enzymatic hydrolysis and provide valuable insights into tissue-specific degradation during bioenergy production. The PDMS imaging reactor could be used to evaluate a range of feedstocks and process conditions.

### 6.2 Wheat straw (Chapter Error! Reference source not found.)

The microfluidic imaging reactor described in **Chapter 3** was utilized to investigate the difference in digestibility based on the stem solidness trait for three wheat straw cultivars with hollow (McNeal), semisolid (Vida), and solid (Choteau) stems. Changes in lignin autofluorescence during dilute acid and dilute alkali pretreatment indicated that the McNeal and Vida samples were more resistant to pretreatment than the pith region of Choteau samples. The pith parenchyma cells of the Choteau sample had the least residual lignin fluorescence after 45 min pretreatment. Further, during enzymatic hydrolysis, the Choteau (solid) stemmed sample had significantly higher glucose and xylose conversion than the McNeal (hollow) and Vida (semisolid) samples. From the brightfield images during enzymatic hydrolysis, the pith-parenchyma cells of the Choteau (solid) sample were the most susceptible to enzymatic hydrolysis after both acid and alkali pretreatment, degrading completely within 48 hours. Therefore, the imaging reactor approach was successful in evaluating the tissue-specific differences in wheat straw digestibility. Due to their higher digestibility, solid-stemmed wheat straw cultivars would be more valuable as biorefinery feedstocks compared to hollow-stemmed cultivars. Additionally, engineering a solid-stemmed phenotype into hollow-stemmed feedstocks like switchgrass, could be one approach to improve their utility as a bioenergy feedstock.



### **6.3 Roller bottle enzymatic hydrolysis (Chapter 5)**

The roller bottle enzymatic hydrolysis system that utilized horizontal mixing for high solids enzymatic hydrolysis achieved improved mixing and saccharification compared to the conventional shake flask method. The method also achieved a higher sample throughput, enabling simultaneous processing of 36 samples on three laboratory scale roller apparatuses in a smaller equipment footprint. Ultimately, this study demonstrated that the roller bottle system is more effective than the shake flask method in overcoming the major high solids loading bottlenecks of poor mixing, inadequate availability of water and viscous nature of pretreated biomass, for a variety of grass-based feedstocks [109]. When fermentation was evaluated real-time using a respirometer, inhibitory feedstocks could be quickly identified from roller bottle or shake flask experiments based on lag time (time to maximum CO<sub>2</sub> evolution rate) and extent of fermentation (maximum volume of CO<sub>2</sub> released). This method can be utilized to compare an array of feedstocks, pretreatment methods, enzyme combinations and different process conditions.

## 7 FUTURE WORK

### 7.1 Microfluidic imaging reactor (Chapter 3)

Based on the results from Chapter 3, it was evident that lignin autofluorescence intensity decreases during acid and alkali pretreatment. Several studies have reported using fluorescence lifetime of lignin to evaluate pretreatment [170, 173, 175, 317]. Fluorescence lifetime varies among the different cell wall layers. Fluorescence lifetime is independent of fluorescence intensity and fluorophore concentration [318, 319] and is influenced by the structure, composition, and the interactions between the fluorophore and its surrounding molecules [170]. Fluorescence lifetime microscopy (FLIM) is usually performed using a fluorescence microscope equipped with a FLIM detector. Several previous studies have used FLIM to characterize G-type and S-type lignin in poplar, pine, *Arabidopsis thaliana* [174, 320, 321]. It would be beneficial to perform time lapsed imaging of pretreatment with fluorescence lifetime imaging to identify the changes in lignin structure during pretreatment.

The CLSM results of the imaging reactor validates its suitability to perform imaging on thin whole sections of biomass during deconstruction. Confocal Raman microscopy (CRM) has been used to conduct label-free characterization of the various chemicals in the biomass during deconstruction (as described in **Error! Reference source not found.**). We conducted some preliminary experiments at the Idaho National laboratory to test the feasibility of using the imaging reactor for CRM, however, lignin autofluorescence was a major hindrance. CRM has long acquisition times for samples even thin samples ( $\sim 2 \mu\text{m}$ ) [322]. Thicker samples led to an increase in acquisition times. Based on literature, photobleaching and surface enhancement with colloidal gold were attempted to reduce acquisition times [323, 324]. It would be beneficial to develop a surface enhanced confocal Raman microscopy method for biomass characterization with optimized parameters for colloidal gold concentration, sample thickness and the size of the gold particles.

### 7.2 Wheat straw (Chapter 4)

The results from **Chapter 4** indicate a higher digestibility of the pith parenchyma cells in the solid-stemmed Choteau sample. However, the rind region remained unhydrolyzed even after 72 hours. It might be useful to determine the hemicellulose distribution of the Choteau sample for better understanding of the deconstruction in the rind region. We have already established the feasibility of immunolabeling using monoclonal antibodies within the imaging reactor. Wheat straw hemicellulose is predominantly made of arabinose and xylose. Previous studies have used antibodies specific to xyloglucan (LM15), arabinoxylan (LM10, LM11), methylesterified homogalacturonan (LM19), arabinogalactan proteins (LM2), and feruloylated arabinoxylan (LM12) [325, 326]. This could help in understanding hemicellulose changes during different pretreatment methods and could be used to help better understand the mechanisms underlying recalcitrance of the rind region.

### **7.3 Roller bottle enzymatic hydrolysis (Chapter 5)**

Based on the results from Chapter 5, the horizontal mixing method facilitated faster liquefaction and improved saccharification up to 50% higher than the conventional shake flask method. One of the most time-consuming steps in conducting the enzymatic hydrolysis experiments is the pH adjustment of the hydrolysates. Manually adding the sodium hydroxide or phosphoric acid to each sample with regular pH monitoring can take up to 5-10 min per sample, which is almost 2-3 hours for 40 samples. The use of robotic platforms for reagent addition has been used in high throughput pretreatment and enzymatic hydrolysis studies [327, 328]. These techniques could be useful for the roller bottle enzymatic hydrolysis method to reduce the post-processing time of the hydrolysate and also increase the throughput further, if necessary.

## 8 REFERENCE LIST

- [1] Basak, B., et al., Advances in physicochemical pretreatment strategies for lignocellulose biomass and their effectiveness in bioconversion for biofuel production. *Bioresource Technology*, 2023. 369: p. 128413.
- [2] IEA, IEA (2023), CO2 Emissions in 2022, IEA, Paris. 2023.
- [3] Marriott, P.E., L.D. Gómez, and S.J. McQueen-Mason, Unlocking the potential of lignocellulosic biomass through plant science. *New phytologist*, 2016. 209(4): p. 1366-1381.
- [4] Carter, C.A. and H.I. Miller, Corn for food, not fuel. *New York Times*, 2012. 21.
- [5] Farzad, S., et al., Multi-product biorefineries from lignocelluloses: a pathway to revitalisation of the sugar industry? *Biotechnol Biofuels*, 2017. 10: p. 87.
- [6] Langholtz, M.H., B.J. Stokes, and L.M. Eaton, 2016 billion-ton report: advancing domestic resources for a thriving bioeconomy. 2016, EERE Publication and Product Library, Washington, DC (United States).
- [7] Maitan-Alfenas, G.P., E.M. Visser, and V.M. Guimarães, Enzymatic hydrolysis of lignocellulosic biomass: converting food waste in valuable products. *Current Opinion in Food Science*, 2015. 1: p. 44-49.
- [8] Li, M., Y. Pu, and A.J. Ragauskas, Current Understanding of the Correlation of Lignin Structure with Biomass Recalcitrance. *Front Chem*, 2016. 4: p. 45.
- [9] Agbor, V.B., et al., Biomass pretreatment: fundamentals toward application. *Biotechnol Adv*, 2011. 29(6): p. 675-85.
- [10] McCann, M.C. and N.C. Carpita, Biomass recalcitrance: a multi-scale, multi-factor, and conversion-specific property. *J Exp Bot*, 2015. 66(14): p. 4109-18.
- [11] FitzPatrick, M., et al., A biorefinery processing perspective: treatment of lignocellulosic materials for the production of value-added products. *Bioresource technology*, 2010. 101(23): p. 8915-8922.
- [12] Donohoe, B.S., et al., Visualizing lignin coalescence and migration through maize cell walls following thermochemical pretreatment. *Biotechnol Bioeng*, 2008. 101(5): p. 913-25.
- [13] Buranov, A.U. and G. Mazza, Lignin in straw of herbaceous crops. *Industrial Crops and Products*, 2008. 28(3): p. 237-259.
- [14] Siqueira, G., et al., Topochemical distribution of lignin and hydroxycinnamic acids in sugar-cane cell walls and its correlation with the enzymatic hydrolysis of polysaccharides. *Biotechnology for biofuels*, 2011. 4: p. 1-9.
- [15] Jung, H. and M. Casler, Maize stem tissues: impact of development on cell wall degradability. *Crop science*, 2006. 46(4): p. 1801-1809.
- [16] Gu, H., R. An, and J. Bao, Pretreatment refining leads to constant particle size distribution of lignocellulose biomass in enzymatic hydrolysis. *Chemical Engineering Journal*, 2018. 352: p. 198-205.
- [17] Schäfer, J., et al., Characterization of *Miscanthus* cell wall polymers. *Gcb Bioenergy*, 2019. 11(1): p. 191-205.

- [18] Zeng, M., et al., Tissue-specific biomass recalcitrance in corn stover pretreated with liquid hot-water: SEM imaging (part 2). *Biotechnol Bioeng*, 2012. 109(2): p. 398-404.
- [19] Zhao, X., L. Zhang, and D. Liu, Biomass recalcitrance. Part I: the chemical compositions and physical structures affecting the enzymatic hydrolysis of lignocellulose. *Biofuels, Bioproducts and Biorefining*, 2012. 6(4): p. 465-482.
- [20] Ong, R.G., et al., Inhibition of microbial biofuel production in drought-stressed switchgrass hydrolysate. *Biotechnol Biofuels*, 2016. 9: p. 237.
- [21] Chapotin, S.M. and J.D. Wolt, Genetically modified crops for the bioeconomy: meeting public and regulatory expectations. *Transgenic Res*, 2007. 16(6): p. 675-88.
- [22] Lewis, S.M., et al., A fuzzy logic-based spatial suitability model for drought-tolerant switchgrass in the United States. *Computers and Electronics in Agriculture*, 2014. 103: p. 39-47.
- [23] Hoover, A., et al., Impact of Drought on Chemical Composition and Sugar Yields From Dilute-Acid Pretreatment and Enzymatic Hydrolysis of Miscanthus, a Tall Fescue Mixture, and Switchgrass. *Frontiers in Energy Research*, 2018. 6.
- [24] Zhang, Y., et al., Diverse lignocellulosic feedstocks can achieve high field-scale ethanol yields while providing flexibility for the biorefinery and landscape-level environmental benefits. *GCB Bioenergy*, 2018. 10(11): p. 825-840.
- [25] Saini, J.K., R. Saini, and L. Tewari, Lignocellulosic agriculture wastes as biomass feedstocks for second-generation bioethanol production: concepts and recent developments. *3 Biotech*, 2015. 5(4): p. 337-353.
- [26] Hadar, Y., Sources for Lignocellulosic Raw Materials for the Production of Ethanol, in *Lignocellulose Conversion*. 2013. p. 21-38.
- [27] Ding, S.-Y., et al., How does plant cell wall nanoscale architecture correlate with enzymatic digestibility? *Science*, 2012. 338(6110): p. 1055-1060.
- [28] Desvaux, M., *Clostridium cellulolyticum*: model organism of mesophilic cellulolytic clostridia. *FEMS microbiology reviews*, 2005. 29(4): p. 741-764.
- [29] Fengel, D. and G. Wegener, *Wood: chemistry, ultrastructure, reactions*. 2011: Walter de Gruyter.
- [30] Silveira, R.L., et al., Plant biomass recalcitrance: effect of hemicellulose composition on nanoscale forces that control cell wall strength. *J Am Chem Soc*, 2013. 135(51): p. 19048-51.
- [31] Pauly, M. and K. Keegstra, Cell-wall carbohydrates and their modification as a resource for biofuels. *Plant J*, 2008. 54(4): p. 559-68.
- [32] Zhang, L., et al., Comparison of lignin distribution, structure, and morphology in wheat straw and wood. *Industrial Crops and Products*, 2022. 187.
- [33] Fromm, J., et al., Lignin distribution in wood cell walls determined by TEM and backscattered SEM techniques. *Journal of Structural Biology*, 2003. 143(1): p. 77-84.

- [34] Hamelinck, C.N., G.v. Hooijdonk, and A.P.C. Faaij, Ethanol from lignocellulosic biomass: techno-economic performance in short-, middle- and long-term. *Biomass and Bioenergy*, 2005. 28(4): p. 384-410.
- [35] Zhou, Z., et al., Lignocellulosic biomass to biofuels and biochemicals: A comprehensive review with a focus on ethanol organosolv pretreatment technology. *Biotechnol Bioeng*, 2018. 115(11): p. 2683-2702.
- [36] Tocco, D., et al., Recent Developments in the Delignification and Exploitation of Grass Lignocellulosic Biomass. *ACS Sustainable Chemistry & Engineering*, 2021. 9(6): p. 2412-2432.
- [37] Clifton-Brown, J., et al., Breeding progress and preparedness for mass-scale deployment of perennial lignocellulosic biomass crops switchgrass, miscanthus, willow and poplar. *Gcb Bioenergy*, 2019. 11(1): p. 118-151.
- [38] Guretzky, J.A., et al., Switchgrass for forage and bioenergy: harvest and nitrogen rate effects on biomass yields and nutrient composition. *Plant and Soil*, 2010. 339(1-2): p. 69-81.
- [39] Zeng, Y., et al., Lignin plays a negative role in the biochemical process for producing lignocellulosic biofuels. *Current opinion in biotechnology*, 2014. 27: p. 38-45.
- [40] Brandt, A., et al., Deconstruction of lignocellulosic biomass with ionic liquids. *Green chemistry*, 2013. 15(3): p. 550-583.
- [41] Carpita, N., M. McCann, and B. Buchanan, Biochemistry and molecular biology of plants. Buchanan, BB, Gruissem, W., Jones, RL, Eds, 2000: p. 52-108.
- [42] Zhong, R., D. Cui, and Z.H. Ye, Secondary cell wall biosynthesis. *New Phytologist*, 2019. 221(4): p. 1703-1723.
- [43] Burton, R.A., M.J. Gidley, and G.B. Fincher, Heterogeneity in the chemistry, structure and function of plant cell walls. *Nat Chem Biol*, 2010. 6(10): p. 724-32.
- [44] Secchi, F., C. Pagliarani, and M.A. Zwieniecki, The functional role of xylem parenchyma cells and aquaporins during recovery from severe water stress. *Plant, cell & environment*, 2017. 40(6): p. 858-871.
- [45] Crang, R., et al., Parenchyma, collenchyma, and sclerenchyma. *Plant Anatomy: A Concept-Based Approach to the Structure of Seed Plants*, 2018: p. 181-213.
- [46] Evert, R.F., *Esau's plant anatomy: meristems, cells, and tissues of the plant body: their structure, function, and development*. 2006: John Wiley & Sons.
- [47] Sanjuan, R., et al., Morphological and chemical composition of pith and fibers from Mexican sugarcane bagasse. *Holz als Roh-und Werkstoff*, 2001. 59: p. 447-450.
- [48] Cutler, D., T. Botha, and D. Stevenson, *Plant anatomy. An applied approach*. Malden, MA: Blackwell Publishing, 2008.
- [49] Hwang, B.G., J. Ryu, and S.J. Lee, Vulnerability of protoxylem and metaxylem vessels to embolisms and radial refilling in a vascular bundle of maize leaves. *Frontiers in Plant Science*, 2016. 7: p. 941.

- [50] Růžička, K., et al., Xylem development—from the cradle to the grave. *New Phytologist*, 2015. 207(3): p. 519-535.
- [51] Słupianek, A., A. DOŁZBŁASZ, and K. Sokołowska, Xylem parenchyma—Role and relevance in wood functioning in trees. *Plants* 10: 1247. 2021.
- [52] Foston, M. and A.J. Ragauskas, Biomass characterization: recent progress in understanding biomass recalcitrance. *Industrial biotechnology*, 2012. 8(4): p. 191-208.
- [53] Himmel, M.E., et al., Biomass recalcitrance: engineering plants and enzymes for biofuels production. *science*, 2007. 315(5813): p. 804-807.
- [54] Wang, Y., et al., Physical-chemical properties of cell wall interface significantly correlated to the complex recalcitrance of corn straw. *Biotechnol Biofuels*, 2021. 14(1): p. 196.
- [55] Wu, X., et al., Biofuels from lignocellulosic biomass. *Sustainable biotechnology: sources of renewable energy*, 2010: p. 19-41.
- [56] Kan, T., V. Strezov, and T.J. Evans, Lignocellulosic biomass pyrolysis: A review of product properties and effects of pyrolysis parameters. *Renewable and sustainable energy reviews*, 2016. 57: p. 1126-1140.
- [57] Balan, V., Current challenges in commercially producing biofuels from lignocellulosic biomass. *ISRN Biotechnol*, 2014. 2014: p. 463074.
- [58] Chundawat, S.P., et al., Deconstruction of lignocellulosic biomass to fuels and chemicals. *Annu Rev Chem Biomol Eng*, 2011. 2: p. 121-45.
- [59] Keating, D.H., et al., Aromatic inhibitors derived from ammonia-pretreated lignocellulose hinder bacterial ethanogenesis by activating regulatory circuits controlling inhibitor efflux and detoxification. *Front Microbiol*, 2014. 5: p. 402.
- [60] Hsu, T.A., M. Ladisch, and G. Tsao, Alcohol from cellulose. 1980, Laboratory of Renewable Resources Engineering, AA Potter Engineering Centre ....
- [61] Taherzadeh, M.J. and K. Karimi, Pretreatment of lignocellulosic wastes to improve ethanol and biogas production: a review. *Int J Mol Sci*, 2008. 9(9): p. 1621-51.
- [62] Chen, X., et al., A highly efficient dilute alkali deacetylation and mechanical (disc) refining process for the conversion of renewable biomass to lower cost sugars. *Biotechnology for Biofuels*, 2014. 7(1): p. 1-12.
- [63] Anukam, A. and J. Berghel, Biomass pretreatment and characterization: A review. Vol. 1. 2020: IntechOpen London, UK.
- [64] Yoon, L.W., et al., Comparison of ionic liquid, acid and alkali pretreatments for sugarcane bagasse enzymatic saccharification. *Journal of Chemical Technology & Biotechnology*, 2011. 86(10): p. 1342-1348.
- [65] Schwalbach, M.S., et al., Complex physiology and compound stress responses during fermentation of alkali-pretreated corn stover hydrolysate by an *Escherichia coli* ethanologen. *Appl Environ Microbiol*, 2012. 78(9): p. 3442-57.

- [66] Yuan, Y., et al., Developing fast enzyme recycling strategy through elucidating enzyme adsorption kinetics on alkali and acid pretreated corn stover. *Biotechnol Biofuels*, 2018. 11: p. 316.
- [67] Hendriks, A.T. and G. Zeeman, Pretreatments to enhance the digestibility of lignocellulosic biomass. *Bioresour Technol*, 2009. 100(1): p. 10-8.
- [68] Sun, Y. and J.J. Cheng, Dilute acid pretreatment of rye straw and bermudagrass for ethanol production. *Bioresour Technol*, 2005. 96(14): p. 1599-606.
- [69] Deshavath, N.N., et al., Dilute acid pretreatment of sorghum biomass to maximize the hemicellulose hydrolysis with minimized levels of fermentative inhibitors for bioethanol production. *3 Biotech*, 2017. 7: p. 1-12.
- [70] Ji, Z., et al., Tissue specific response of *Miscanthus x giganteus* to dilute acid pretreatment for enhancing cellulose digestibility. *Carbohydr Polym*, 2016. 154: p. 247-56.
- [71] Ji, Z., et al., Visualization of *Miscanthus x giganteus* cell wall deconstruction subjected to dilute acid pretreatment for enhanced enzymatic digestibility. *Biotechnol Biofuels*, 2015. 8: p. 103.
- [72] Sun, Q., et al., Effect of lignin content on changes occurring in poplar cellulose ultrastructure during dilute acid pretreatment. *Biotechnology for Biofuels*, 2014. 7(1): p. 150.
- [73] Karp, E.M., et al., Alkaline Pretreatment of Corn Stover: Bench-Scale Fractionation and Stream Characterization. *ACS Sustainable Chemistry & Engineering*, 2014. 2(6): p. 1481-1491.
- [74] Brodeur, G., et al., Chemical and physicochemical pretreatment of lignocellulosic biomass: a review. *Enzyme Res*, 2011. 2011: p. 787532.
- [75] Kim, J.S., Y.Y. Lee, and T.H. Kim, A review on alkaline pretreatment technology for bioconversion of lignocellulosic biomass. *Bioresour Technol*, 2016. 199: p. 42-48.
- [76] Chundawat, S.P., et al., Multifaceted characterization of cell wall decomposition products formed during ammonia fiber expansion (AFEX) and dilute acid based pretreatments. *Bioresour Technol*, 2010. 101(21): p. 8429-38.
- [77] Chundawat, S.P.S., et al., Ammonia Fiber Expansion (AFEX) Pretreatment of Lignocellulosic Biomass. *J Vis Exp*, 2020(158).
- [78] Bals, B.D., et al., Enzymatic hydrolysis of pelletized AFEX-treated corn stover at high solid loadings. *Biotechnol Bioeng*, 2014. 111(2): p. 264-71.
- [79] Zhang, Y., et al., Production of hydrolysates from unmilled AFEX-pretreated switchgrass and comparative fermentation with *Zymomonas mobilis*. *Bioresource Technology Reports*, 2020. 11: p. 100517.
- [80] Kim, D., Physico-chemical conversion of lignocellulose: inhibitor effects and detoxification strategies: a mini review. *Molecules*, 2018. 23(2): p. 309.
- [81] Humpala, J.F., et al., Probing the nature of AFEX-pretreated corn stover derived decomposition products that inhibit cellulase activity. *Bioresource technology*, 2014. 152: p. 38-45.



- [82] Jørgensen, H., J.B. Kristensen, and C. Felby, Enzymatic conversion of lignocellulose into fermentable sugars: challenges and opportunities. *Biofuels, Bioproducts and Biorefining*, 2007. 1(2): p. 119-134.
- [83] Hodge, D.B., et al., Soluble and insoluble solids contributions to high-solids enzymatic hydrolysis of lignocellulose. *Bioresour Technol*, 2008. 99(18): p. 8940-8.
- [84] Coughlan, M.P., The properties of fungal and bacterial cellulases with comment on their production and application. *Biotechnology and genetic engineering reviews*, 1985. 3(1): p. 39-110.
- [85] Mohagheghi, A., M. Ruth, and D.J. Schell, Conditioning hemicellulose hydrolysates for fermentation: Effects of overliming pH on sugar and ethanol yields. *Process Biochemistry*, 2006. 41(8): p. 1806-1811.
- [86] Wang, M., et al., Cellulolytic enzyme production and enzymatic hydrolysis for second-generation bioethanol production. *Adv Biochem Eng Biotechnol*, 2012. 128: p. 1-24.
- [87] Alvarez, C., F.M. Reyes-Sosa, and B. Diez, Enzymatic hydrolysis of biomass from wood. *Microb Biotechnol*, 2016. 9(2): p. 149-56.
- [88] Öhgren, K., et al., A comparison between simultaneous saccharification and fermentation and separate hydrolysis and fermentation using steam-pretreated corn stover. *Process Biochemistry*, 2007. 42(5): p. 834-839.
- [89] Mcmillan, J.D., et al. Simultaneous saccharification and cofermentation of dilute-acid pretreated yellow poplar hardwood to ethanol using xylose-fermenting *Zymomonas mobilis*. in *Twentieth Symposium on Biotechnology for Fuels and Chemicals*. 1999. Springer.
- [90] Gunasekaran, P. and K.C. Raj, Ethanol fermentation technology–*Zymomonas mobilis*. *Current Science*, 1999: p. 56-68.
- [91] Zhao, N., et al., Flocculating *Zymomonas mobilis* is a promising host to be engineered for fuel ethanol production from lignocellulosic biomass. *Biotechnology journal*, 2014. 9(3): p. 362-371.
- [92] Roca, C. and L. Olsson, Increasing ethanol productivity during xylose fermentation by cell recycling of recombinant *Saccharomyces cerevisiae*. *Appl Microbiol Biotechnol*, 2003. 60(5): p. 560-3.
- [93] Agrawal, M., Y. Wang, and R.R. Chen, Engineering efficient xylose metabolism into an acetic acid-tolerant *Zymomonas mobilis* strain by introducing adaptation-induced mutations. *Biotechnology letters*, 2012. 34: p. 1825-1832.
- [94] Weil, J.R., et al., Removal of fermentation inhibitors formed during pretreatment of biomass by polymeric adsorbents. *Industrial & engineering chemistry research*, 2002. 41(24): p. 6132-6138.
- [95] Huang, H., et al., Identification of crucial yeast inhibitors in bio-ethanol and improvement of fermentation at high pH and high total solids. *Bioresour Technol*, 2011. 102(16): p. 7486-93.

- [96] Dayton, D.C. and T.D. Foust, Analytical methods for biomass characterization and conversion. 2019: Elsevier.
- [97] Meenakshisundaram, S., et al., Chemically and Physically Pretreated Straw in Moderate Conditions: Poor Correlation between Biogas Production and Commonly Used Biomass Characterization. *Energies*, 2023. 16(3): p. 1146.
- [98] Zhao, Y., et al., Advances in Imaging Plant Cell Walls. *Trends Plant Sci*, 2019. 24(9): p. 867-878.
- [99] Karimi, K. and M.J. Taherzadeh, A critical review of analytical methods in pretreatment of lignocelluloses: Composition, imaging, and crystallinity. *Bioresour Technol*, 2016. 200: p. 1008-18.
- [100] Jorgensen, H., et al., Liquefaction of lignocellulose at high-solids concentrations. *Biotechnol Bioeng*, 2007. 96(5): p. 862-70.
- [101] Viamajala, S., et al., Rheology of corn stover slurries at high solids concentrations--effects of saccharification and particle size. *Bioresour Technol*, 2009. 100(2): p. 925-34.
- [102] Roche, C.M., C.J. Dibble, and J.J. Stickel, Laboratory-scale method for enzymatic saccharification of lignocellulosic biomass at high-solids loadings. *Biotechnol Biofuels*, 2009. 2(1): p. 28.
- [103] Lau, M.W. and B.E. Dale, Cellulosic ethanol production from AFEX-treated corn stover using *Saccharomyces cerevisiae* 424A(LNH-ST). *Proc Natl Acad Sci U S A*, 2009. 106(5): p. 1368-73.
- [104] Roberts, K.M., et al., The effects of water interactions in cellulose suspensions on mass transfer and saccharification efficiency at high solids loadings. *Cellulose*, 2011. 18(3): p. 759-773.
- [105] Modenbach, A.A. and S.E. Nokes, Enzymatic hydrolysis of biomass at high-solids loadings – A review. *Biomass and Bioenergy*, 2013. 56: p. 526-544.
- [106] Wang, L., R. Templer, and R.J. Murphy, High-solids loading enzymatic hydrolysis of waste papers for biofuel production. *Applied Energy*, 2012. 99: p. 23-31.
- [107] Kristensen, J.B., C. Felby, and H. Jorgensen, Yield-determining factors in high-solids enzymatic hydrolysis of lignocellulose. *Biotechnol Biofuels*, 2009. 2(1): p. 11.
- [108] Selig, M.J., et al., Considering water availability and the effect of solute concentration on high solids saccharification of lignocellulosic biomass. *Biotechnology progress*, 2012. 28(6): p. 1478-1490.
- [109] Lu, M., et al., High-solids enzymatic hydrolysis of ball-milled corn stover with reduced slurry viscosity and improved sugar yields. *Biotechnol Biofuels*, 2020. 13: p. 77.
- [110] da Silva, A.S., et al., Constraints and advances in high-solids enzymatic hydrolysis of lignocellulosic biomass: a critical review. *Biotechnol Biofuels*, 2020. 13: p. 58.
- [111] Wiman, M., et al., Rheological characterization of dilute acid pretreated softwood. *Biotechnol Bioeng*, 2011. 108(5): p. 1031-41.

- [112] Du, J., et al., Identifying and overcoming the effect of mass transfer limitation on decreased yield in enzymatic hydrolysis of lignocellulose at high solid concentrations. *Bioresour Technol*, 2017. 229: p. 88-95.
- [113] Cardona, M.J., et al., A process for energy-efficient high-solids fed-batch enzymatic liquefaction of cellulosic biomass. *Bioresour Technol*, 2015. 198: p. 488-96.
- [114] Ramachandriya, K.D., et al., Effect of high dry solids loading on enzymatic hydrolysis of acid bisulfite pretreated Eastern redcedar. *Bioresour Technol*, 2013. 147: p. 168-176.
- [115] Hodge, D.B., et al., Model-based fed-batch for high-solids enzymatic cellulose hydrolysis. *Appl Biochem Biotechnol*, 2009. 152(1): p. 88-107.
- [116] Mukasekuru, M.R., et al., Fed-batch high-solids enzymatic saccharification of lignocellulosic substrates with a combination of additives and accessory enzymes. *Industrial Crops and Products*, 2020. 146.
- [117] Ghorbanian, M., D.C. Russ, and R.E. Berson, Mixing analysis of PCS slurries in a horizontal scraped surface bioreactor. *Bioprocess Biosyst Eng*, 2014. 37(10): p. 2113-9.
- [118] Lou, H., et al., Nonionic surfactants enhanced enzymatic hydrolysis of cellulose by reducing cellulase deactivation caused by shear force and air-liquid interface. *Bioresour Technol*, 2018. 249: p. 1-8.
- [119] Lu, Y., et al., Influence of high solid concentration on enzymatic hydrolysis and fermentation of steam-exploded corn stover biomass. *Appl Biochem Biotechnol*, 2010. 160(2): p. 360-9.
- [120] Nilvebrant, N.-O., et al., Detoxification of lignocellulose hydrolysates with ion-exchange resins. *Applied biochemistry and biotechnology*, 2001. 91: p. 35-49.
- [121] Jurado, M., et al., Laccase detoxification of steam-exploded wheat straw for second generation bioethanol. *Bioresource technology*, 2009. 100(24): p. 6378-6384.
- [122] Berson, R.E., et al., Detoxification of actual pretreated corn stover hydrolysate using activated carbon powder. *Applied Biochemistry and Biotechnology*, 2005. 124: p. 923-934.
- [123] Banerjee, G., et al., Scale-up and integration of alkaline hydrogen peroxide pretreatment, enzymatic hydrolysis, and ethanolic fermentation. *Biotechnology and bioengineering*, 2012. 109(4): p. 922-931.
- [124] Cannella, D., P.V. Sveding, and H. Jørgensen, PEI detoxification of pretreated spruce for high solids ethanol fermentation. *Applied energy*, 2014. 132: p. 394-403.
- [125] Von Sivers, M., et al., Cost analysis of ethanol production from willow using recombinant *Escherichia coli*. *Biotechnology Progress*, 1994. 10(5): p. 555-560.
- [126] Lau, M.W., B.E. Dale, and V. Balan, Ethanolic fermentation of hydrolysates from ammonia fiber expansion (AFEX) treated corn stover and distillers grain without

- detoxification and external nutrient supplementation. *Biotechnology and bioengineering*, 2008. 99(3): p. 529-539.
- [127] Casey, E., et al., Effect of acetic acid and pH on the cofermentation of glucose and xylose to ethanol by a genetically engineered strain of *Saccharomyces cerevisiae*. *FEMS yeast research*, 2010. 10(4): p. 385-393.
- [128] Huang, H., et al., Identification of crucial yeast inhibitors in bio-ethanol and improvement of fermentation at high pH and high total solids. *Bioresource technology*, 2011. 102(16): p. 7486-7493.
- [129] Rodrigues, R., et al., Comprehensive approach of methods for microstructural analysis and analytical tools in lignocellulosic biomass assessment - A review. *Bioresour Technol*, 2022. 348: p. 126627.
- [130] Donohoe, B.S., et al., Surface and ultrastructural characterization of raw and pretreated switchgrass. *Bioresour Technol*, 2011. 102(24): p. 11097-104.
- [131] DeVree, B.T., et al., Current and future advances in fluorescence-based visualization of plant cell wall components and cell wall biosynthetic machineries. *Biotechnol Biofuels*, 2021. 14(1): p. 78.
- [132] Ji, Z., et al., In situ microscopic investigation of plant cell walls deconstruction in biorefinery. *Microscopy: Advances in Scientific Research and Education*, Formatex Research Center, Spain, 2014: p. 426-433.
- [133] Donaldson, L., *Autofluorescence in Plants*. *Molecules*, 2020. 25(10).
- [134] Reza, M., et al., Transmission Electron Microscopy for Wood and Fiber Analysis- A Review. *BioResources*, 2015. 10(3).
- [135] Zhang, X., L. Li, and F. Xu, Chemical characteristics of wood cell wall with an emphasis on ultrastructure: A mini-review. *Forests*, 2022. 13(3): p. 439.
- [136] Kaushik, M., et al., Transmission electron microscopy for the characterization of cellulose nanocrystals. *The transmission electron microscope-theory and applications*, 2015: p. 130-163.
- [137] Santoro, F., et al., Revealing the Cell-Material Interface with Nanometer Resolution by Focused Ion Beam/Scanning Electron Microscopy. *ACS Nano*, 2017. 11(8): p. 8320-8328.
- [138] Zhou, W., et al., Fundamentals of scanning electron microscopy (SEM). *Scanning Microscopy for Nanotechnology: Techniques and Applications*, 2007: p. 1-40.
- [139] Araya, F., et al., Condensed lignin structures and re-localization achieved at high severities in autohydrolysis of *Eucalyptus globulus* wood and their relationship with cellulose accessibility. *Biotechnol Bioeng*, 2015. 112(9): p. 1783-91.
- [140] Biermann, C.J., G.D. McGinnis, and T.P. Schultz, Scanning electron microscopy of mixed hardwoods subjected to various pretreatment processes. *Journal of agricultural and food chemistry*, 1987. 35(5): p. 713-716.
- [141] Anglès, M., et al., Suitability of steam exploded residual softwood for the production of binderless panels. Effect of the pre-treatment severity and lignin addition. *Biomass and Bioenergy*, 2001. 21(3): p. 211-224.

- [142] Blanchette, R., L. Otjen, and M. Carlson, Lignin distribution in cell walls of birch wood decayed by white rot basidiomycetes. *Phytopathology*, 1987. 77(5): p. 684-690.
- [143] Chundawat, S.P.S., et al., Multi-scale visualization and characterization of lignocellulosic plant cell wall deconstruction during thermochemical pretreatment. *Energy & Environmental Science*, 2011. 4(3).
- [144] Lambert, E., et al., Real time and quantitative imaging of lignocellulosic films hydrolysis by atomic force microscopy reveals lignin recalcitrance at nanoscale. *Biomacromolecules*, 2018. 20(1): p. 515-527.
- [145] Okano, Y., Scanning Electron Microscopy, in *Compendium of Surface and Interface Analysis*, J. The Surface Science Society of, Editor. 2018, Springer Singapore: Singapore. p. 563-569.
- [146] Marturi, N., Vision and visual servoing for nanomanipulation and nanocharacterization in scanning electron microscope. 2013, Université de Franche-Comté.
- [147] Ding, S.-Y. and M.E. Himmel, The maize primary cell wall microfibril: a new model derived from direct visualization. *Journal of agricultural and food chemistry*, 2006. 54(3): p. 597-606.
- [148] Abud, Y., et al., Revealing the microfibrillar arrangement of the cell wall surface and the macromolecular effects of thermochemical pretreatment in sugarcane by atomic force microscopy. *Industrial Crops and Products*, 2013. 51: p. 62-69.
- [149] Allison, D.P., et al., Atomic force microscopy of biological samples. *Wiley Interdiscip Rev Nanomed Nanobiotechnol*, 2010. 2(6): p. 618-34.
- [150] Davies, L.M. and P.J. Harris, Atomic force microscopy of microfibrils in primary cell walls. *Planta*, 2003. 217(2): p. 283-9.
- [151] Qin, C., K. Clarke, and K. Li, Interactive forces between lignin and cellulase as determined by atomic force microscopy. *Biotechnology for biofuels*, 2014. 7: p. 1-10.
- [152] Yarbrough, J.M., M.E. Himmel, and S.-Y. Ding, Plant cell wall characterization using scanning probe microscopy techniques. *Biotechnology for biofuels*, 2009. 2(1): p. 1-11.
- [153] Gorzsás, A., Chemical imaging of xylem by Raman microspectroscopy. *Xylem: methods and protocols*, 2017: p. 133-178.
- [154] Ma, J., et al., Raman microspectroscopy imaging study on topochemical correlation between lignin and hydroxycinnamic acids in *Miscanthus sinensis*. *Microscopy and Microanalysis*, 2014. 20(3): p. 956-963.
- [155] Gierlinger, N. and M. Schwanninger, Chemical imaging of poplar wood cell walls by confocal Raman microscopy. *Plant Physiol*, 2006. 140(4): p. 1246-54.
- [156] Agarwal, U.P., Raman imaging to investigate ultrastructure and composition of plant cell walls: distribution of lignin and cellulose in black spruce wood (*Picea mariana*). *Planta*, 2006. 224(5): p. 1141-53.

- [157] Toporski, J., T. Dieing, and O. Hollricher, *Confocal Raman Microscopy*. Vol. 66. 2018: Springer.
- [158] Chu, L.-Q., et al., Base-induced delignification of miscanthus x giganteus studied by three-dimensional confocal raman imaging. *Bioresource technology*, 2010. 101(13): p. 4919-4925.
- [159] Jin, Z., et al., Area-Selective Depolymerization of Hydroxycinnamates Visualized by Raman Imaging in Miscanthus sinensis cv. Cell Wall. *Journal of Agricultural and Food Chemistry*, 2023.
- [160] Lucas, M., et al., Reversible swelling of the cell wall of poplar biomass by ionic liquid at room temperature. *Bioresource technology*, 2011. 102(6): p. 4518-4523.
- [161] Zhang, X., et al., Using confocal Raman microscopy to real-time monitor poplar cell wall swelling and dissolution during ionic liquid pretreatment. *Microscopy research and technique*, 2014. 77(8): p. 609-618.
- [162] Li, Y.-J., et al., Evaluating the efficiency of  $\gamma$ -valerolactone/water/acid system on Eucalyptus pretreatment by confocal Raman microscopy and enzymatic hydrolysis for bioethanol production. *Renewable Energy*, 2019. 134: p. 228-234.
- [163] Moran-Mirabal, J.M., The study of cell wall structure and cellulose–cellulase interactions through fluorescence microscopy. *Cellulose*, 2013. 20(5): p. 2291-2309.
- [164] Valdez-Vazquez, I., et al., *Microscopy applied in biomass characterization*, in *Analytical Techniques and Methods for Biomass*. 2016, Springer. p. 173-196.
- [165] Luterbacher, J.S., L.P. Walker, and J.M. Moran-Mirabal, Observing and modeling BMCC degradation by commercial cellulase cocktails with fluorescently labeled *Trichoderma reesei* Cel7A through confocal microscopy. *Biotechnol Bioeng*, 2013. 110(1): p. 108-17.
- [166] Kim, J.E. and J.-W. Lee, Microstructural changes in the cell wall and enzyme adsorption properties of lignocellulosic biomass subjected to thermochemical pretreatment. *Cellulose*, 2018. 26(2): p. 1111-1124.
- [167] Singh, S., B.A. Simmons, and K.P. Vogel, Visualization of biomass solubilization and cellulose regeneration during ionic liquid pretreatment of switchgrass. *Biotechnol Bioeng*, 2009. 104(1): p. 68-75.
- [168] Hou, X.D., N. Li, and M.H. Zong, Renewable bio ionic liquids-water mixtures-mediated selective removal of lignin from rice straw: Visualization of changes in composition and cell wall structure. *Biotechnology and bioengineering*, 2013. 110(7): p. 1895-1902.
- [169] Lavrentovich, O.D., *Confocal fluorescence microscopy. Characterization of materials*, 2002: p. 1-15.
- [170] Donaldson, L.A. and K. Radotic, Fluorescence lifetime imaging of lignin autofluorescence in normal and compression wood. *J Microsc*, 2013. 251(2): p. 178-87.
- [171] Wagner, A., et al., Suppression of 4-coumarate-CoA ligase in the coniferous gymnosperm *Pinus radiata*. *Plant physiology*, 2009. 149(1): p. 370-383.

- [172] Donaldson, L.A. and J.P. Knox, Localization of cell wall polysaccharides in normal and compression wood of radiata pine: relationships with lignification and microfibril orientation. *Plant physiology*, 2012. 158(2): p. 642-653.
- [173] Auxenfans, T., C. Terryn, and G. Paës, Seeing biomass recalcitrance through fluorescence. *Scientific Reports*, 2017. 7(1): p. 8838.
- [174] Chabbert, B., et al., Fluorescence techniques can reveal cell wall organization and predict saccharification in pretreated wood biomass. *Industrial Crops and Products*, 2018. 123: p. 84-92.
- [175] Wightman, R., M. Busse-Wicher, and P. Dupree, Correlative FLIM-confocal-Raman mapping applied to plant lignin composition and autofluorescence. *Micron*, 2019. 126: p. 102733.
- [176] Zhang, J., et al., Visualizing plant cell wall changes proves the superiority of hydrochloric acid over sulfuric acid catalyzed  $\gamma$ -valerolactone pretreatment. *Chemical Engineering Journal*, 2021. 412.
- [177] Devaux, M.F., et al., Synchrotron Time-Lapse Imaging of Lignocellulosic Biomass Hydrolysis: Tracking Enzyme Localization by Protein Autofluorescence and Biochemical Modification of Cell Walls by Microfluidic Infrared Microspectroscopy. *Front Plant Sci*, 2018. 9: p. 200.
- [178] Donaldson, L. and A. Vaidya, Visualising recalcitrance by colocalisation of cellulase, lignin and cellulose in pretreated pine biomass using fluorescence microscopy. *Sci Rep*, 2017. 7: p. 44386.
- [179] Zeng, Y., et al., In situ micro-spectroscopic investigation of lignin in poplar cell walls pretreated by maleic acid. *Biotechnology for Biofuels*, 2015. 8: p. 1-12.
- [180] Avci, U., S. Pattathil, and M.G. Hahn, Immunological Approaches to Plant Cell Wall and Biomass Characterization: Immunolocalization of Glycan Epitopes.
- [181] Costa, T.H., et al., Tissue-specific distribution of hemicelluloses in six different sugarcane hybrids as related to cell wall recalcitrance. *Biotechnol Biofuels*, 2016. 9: p. 99.
- [182] Kim, J.S., et al., Spatial and temporal variability of xylan distribution in differentiating secondary xylem of hybrid aspen. *Planta*, 2012. 235(6): p. 1315-30.
- [183] Pattathil, S., et al., A comprehensive toolkit of plant cell wall glycan-directed monoclonal antibodies. *Plant Physiol*, 2010. 153(2): p. 514-25.
- [184] Sutherland, P., I. Hallett, and M. Jones, Probing cell wall structure and development by the use of antibodies: a personal perspective. *New Zeal J For Sci*, 2009. 39: p. 197-205.
- [185] da Costa, R.M.F., et al., Desirable plant cell wall traits for higher-quality miscanthus lignocellulosic biomass. *Biotechnol Biofuels*, 2019. 12: p. 85.
- [186] Avci, U., et al., Effects of extractive ammonia pretreatment on the ultrastructure and glycan composition of corn stover. *Frontiers in Energy Research*, 2019. 7: p. 85.

- [187] Brunecky, R., et al., Redistribution of xylan in maize cell walls during dilute acid pretreatment. *Biotechnol Bioeng*, 2009. 102(6): p. 1537-43.
- [188] Banerjee, R., et al., Intervention of microfluidics in biofuel and bioenergy sectors: Technological considerations and future prospects. *Renewable and Sustainable Energy Reviews*, 2019. 101: p. 548-558.
- [189] Xuan, X., Recent advances in direct current electrokinetic manipulation of particles for microfluidic applications. *Electrophoresis*, 2019. 40(18-19): p. 2484-2513.
- [190] Tonin, M., N. Descharmes, and R. Houdre, Hybrid PDMS/glass microfluidics for high resolution imaging and application to sub-wavelength particle trapping. *Lab Chip*, 2016. 16(3): p. 465-70.
- [191] Gupta, S., et al., Lab-on-chip technology: A review on design trends and future scope in biomedical applications. *Int. J. Bio-Sci. Bio-Technol*, 2016. 8: p. 311-322.
- [192] Dkhar, D.S., et al., Integrated lab-on-a-chip devices: Fabrication methodologies, transduction system for sensing purposes. *Journal of Pharmaceutical and Biomedical Analysis*, 2023. 223: p. 115120.
- [193] Faustino, V., et al., Biomedical microfluidic devices by using low-cost fabrication techniques: A review. *J Biomech*, 2016. 49(11): p. 2280-92.
- [194] Xiong, L., P. Chen, and Q. Zhou, Adhesion promotion between PDMS and glass by oxygen plasma pre-treatment. *Journal of Adhesion Science and Technology*, 2014. 28(11): p. 1046-1054.
- [195] Ho, C.M., et al., 3D printed microfluidics for biological applications. *Lab Chip*, 2015. 15(18): p. 3627-37.
- [196] Zhu, H., et al., Recent advances in lab-on-a-chip technologies for viral diagnosis. *Biosensors and Bioelectronics*, 2020. 153: p. 112041.
- [197] Waheed, S., et al., Enhanced physicochemical properties of polydimethylsiloxane based microfluidic devices and thin films by incorporating synthetic micro-diamond. *Sci Rep*, 2017. 7(1): p. 15109.
- [198] Yeo, L.Y., et al., Microfluidic devices for bioapplications. *small*, 2011. 7(1): p. 12-48.
- [199] Leclerc, E., Y. Sakai, and T. Fujii, Cell culture in 3-dimensional microfluidic structure of PDMS (polydimethylsiloxane). *Biomedical microdevices*, 2003. 5: p. 109-114.
- [200] Kim, D.N., Y. Lee, and W.-G. Koh, Fabrication of microfluidic devices incorporating bead-based reaction and microarray-based detection system for enzymatic assay. *Sensors and Actuators B: Chemical*, 2009. 137(1): p. 305-312.
- [201] Dittrich, P.S. and A. Manz, Lab-on-a-chip: microfluidics in drug discovery. *Nature reviews Drug discovery*, 2006. 5(3): p. 210-218.
- [202] Székely, L. and A. Guttman, New advances in microchip fabrication for electrochromatography. *Electrophoresis*, 2005. 26(24): p. 4590-4604.



- [203] Anderson, J.R., et al., Fabrication of topologically complex three-dimensional microfluidic systems in PDMS by rapid prototyping. *Analytical chemistry*, 2000. 72(14): p. 3158-3164.
- [204] Kim, J.J.K., H. Al Thuwaini, and M. Almuslem, Photolithography of SU-8 microtowers for a 100-turn, 3-D toroidal microinductor. *Micro and Nano Systems Letters*, 2018. 6(1).
- [205] Martinez-Duarte, R., SU-8 Photolithography as a Toolbox for Carbon MEMS. *Micromachines*, 2014. 5(3): p. 766-782.
- [206] Ginestra, P., M. Madou, and E. Ceretti, Production of carbonized micro-patterns by photolithography and pyrolysis. *Precision Engineering*, 2019. 55: p. 137-143.
- [207] Guan, G., et al., Transesterification of sunflower oil with methanol in a microtube reactor. *Industrial & Engineering Chemistry Research*, 2009. 48(3): p. 1357-1363.
- [208] Richard, R., S. Thiebaud-Roux, and L. Prat, Modelling the kinetics of transesterification reaction of sunflower oil with ethanol in microreactors. *Chemical engineering science*, 2013. 87: p. 258-269.
- [209] Bodénès, P., et al., Microfluidic techniques for enhancing biofuel and biorefinery industry based on microalgae. *Biotechnology for biofuels*, 2019. 12: p. 1-25.
- [210] Holcomb, R.E., et al., Culturing and investigation of stress-induced lipid accumulation in microalgae using a microfluidic device. *Analytical and bioanalytical chemistry*, 2011. 400: p. 245-253.
- [211] Cheng, X., M.D. Ooms, and D. Sinton, Biomass-to-biocrude on a chip via hydrothermal liquefaction of algae. *Lab on a Chip*, 2016. 16(2): p. 256-260.
- [212] Han, A., et al., Microfabricated devices in microbial bioenergy sciences. *Trends in biotechnology*, 2013. 31(4): p. 225-232.
- [213] Qian, F., et al., A 1.5  $\mu$ L microbial fuel cell for on-chip bioelectricity generation. *Lab on a Chip*, 2009. 9(21): p. 3076-3081.
- [214] Huang, Z., et al., A versatile optofluidic microreactor for artificial photosynthesis induced coenzyme regeneration and l-glutamate synthesis. *Lab on a Chip*, 2022. 22(15): p. 2878-2885.
- [215] Szita, N., et al., Development of a multiplexed microbioreactor system for high-throughput bioprocessing. *Lab on a Chip*, 2005. 5(8): p. 819-826.
- [216] Sills, D.L. and J.M. Gossett, Using FTIR spectroscopy to model alkaline pretreatment and enzymatic saccharification of six lignocellulosic biomasses. *Biotechnology and Bioengineering*, 2012. 109(4): p. 894-903.
- [217] Schafer, J., et al., Characterization of Miscanthus cell wall polymers. *Glob Change Biol Bioenergy*, 2019. 11(1): p. 191-205.
- [218] Herbaut, M., et al., Multimodal analysis of pretreated biomass species highlights generic markers of lignocellulose recalcitrance. *Biotechnol Biofuels*, 2018. 11: p. 52.
- [219] Dumitrache, A., et al., Cellulose and lignin colocalization at the plant cell wall surface limits microbial hydrolysis of Populus biomass. *Green Chemistry*, 2017. 19(9): p. 2275-2285.

- [220] Luterbacher, J.S., et al., Modeling Enzymatic Hydrolysis of Lignocellulosic Substrates using Fluorescent Confocal Microscopy II: Pretreated Biomass. *Biotechnology and Bioengineering*, 2015. 112(1): p. 32-42.
- [221] Velvizhi, G., et al., Integrated biorefinery processes for conversion of lignocellulosic biomass to value added materials: Paving a path towards circular economy. *Bioresour Technol*, 2022. 343: p. 126151.
- [222] McCartney, L., S.E. Marcus, and J.P. Knox, Monoclonal antibodies to plant cell wall xylans and arabinoxylans. *J Histochem Cytochem*, 2005. 53(4): p. 543-6.
- [223] Barnes, W.J. and C.T. Anderson, Acetyl bromide soluble lignin (ABSL) assay for total lignin quantification from plant biomass. *Bio-protocol*, 2017. 7(5): p. e2149-e2149.
- [224] Foster, C.E., T.M. Martin, and M. Pauly, Comprehensive compositional analysis of plant cell walls (lignocellulosic biomass) part II: carbohydrates. *J Vis Exp*, 2010(37).
- [225] Jung, H.G. and M.D. Casler, Maize Stem Tissues: Cell Wall Concentration and Composition during Development. *Crop Science*, 2006. 46(4): p. 1793-1800.
- [226] Meng, X., et al., Physicochemical Structural Changes of Poplar and Switchgrass during Biomass Pretreatment and Enzymatic Hydrolysis. *ACS Sustainable Chemistry & Engineering*, 2016. 4(9): p. 4563-4572.
- [227] Jung, H. and F. Engels, Alfalfa stem tissues: cell wall deposition, composition, and degradability. *Crop science*, 2002. 42(2): p. 524-534.
- [228] Chen, L., et al., Lignin deposition and associated changes in anatomy, enzyme activity, gene expression, and ruminal degradability in stems of tall fescue at different developmental stages. *Journal of Agricultural and Food Chemistry*, 2002. 50(20): p. 5558-5565.
- [229] Pu, Y., et al., Assessing the molecular structure basis for biomass recalcitrance during dilute acid and hydrothermal pretreatments. *Biotechnology for biofuels*, 2013. 6(1): p. 1-13.
- [230] Zoghiami, A. and G. Paes, Lignocellulosic Biomass: Understanding Recalcitrance and Predicting Hydrolysis. *Front Chem*, 2019. 7: p. 874.
- [231] Sun, S., et al., The role of pretreatment in improving the enzymatic hydrolysis of lignocellulosic materials. *Bioresour Technol*, 2016. 199: p. 49-58.
- [232] Karimi, K., M. Shafiei, and R. Kumar, Progress in physical and chemical pretreatment of lignocellulosic biomass, in *Biofuel technologies*. 2013, Springer. p. 53-96.
- [233] Gómez, L.D., et al., Side by Side Comparison of Chemical Compounds Generated by Aqueous Pretreatments of Maize Stover, Miscanthus and Sugarcane Bagasse. *BioEnergy Research*, 2014. 7(4): p. 1466-1480.
- [234] Zhao, X., L. Zhang, and D. Liu, Biomass recalcitrance. Part II: Fundamentals of different pre-treatments to increase the enzymatic digestibility of lignocellulose. *Biofuels, Bioproducts and Biorefining*, 2012. 6(5): p. 561-579.

- [235] McIntosh, S. and T. Vancov, Optimisation of dilute alkaline pretreatment for enzymatic saccharification of wheat straw. *Biomass and bioenergy*, 2011. 35(7): p. 3094-3103.
- [236] Mittal, A., et al., Investigation of the role of lignin in biphasic xylan hydrolysis during dilute acid and organosolv pretreatment of corn stover. *Green Chemistry*, 2015. 17(3): p. 1546-1558.
- [237] Dong, M., et al., Pretreatment of sweet sorghum straw and its enzymatic digestion: insight into the structural changes and visualization of hydrolysis process. *Biotechnol Biofuels*, 2019. 12: p. 276.
- [238] Aboagye, D., et al., Glucose recovery from different corn stover fractions using dilute acid and alkaline pretreatment techniques. *Journal of Ecology and Environment*, 2017. 41: p. 1-11.
- [239] Kim, S., et al., Carbon-Negative Biofuel Production. *Environ Sci Technol*, 2020. 54(17): p. 10797-10807.
- [240] van der Weijde, T., et al., The potential of C4 grasses for cellulosic biofuel production. *Frontiers in plant science*, 2013. 4: p. 107.
- [241] Parrish, D.J., M.D. Casler, and A. Monti, The evolution of switchgrass as an energy crop. *Switchgrass: a valuable biomass crop for energy*, 2012: p. 1-28.
- [242] Jung, H.J., D.A. Samac, and G. Sarath, Modifying crops to increase cell wall digestibility. *Plant Sci*, 2012. 185-186: p. 65-77.
- [243] Sun, L., B.A. Simmons, and S. Singh, Understanding tissue specific compositions of bioenergy feedstocks through hyperspectral Raman imaging. *Biotechnol Bioeng*, 2011. 108(2): p. 286-95.
- [244] Calviño, M., R. Bruggmann, and J. Messing, Characterization of the small RNA component of the transcriptome from grain and sweet sorghum stems. *BMC genomics*, 2011. 12(1): p. 1-13.
- [245] Glasziou, K. and K. Gayler, Storage of sugars in stalks of sugar cane. *The Botanical Review*, 1972: p. 471-490.
- [246] Hoffmann-Thoma, G., et al., Sucrose accumulation in sweet sorghum stem internodes in relation to growth. *Physiologia Plantarum*, 1996. 97(2): p. 277-284.
- [247] McCormick, A., D. Watt, and M. Cramer, Supply and demand: sink regulation of sugar accumulation in sugarcane. *Journal of experimental botany*, 2009. 60(2): p. 357-364.
- [248] Scofield, G.N., et al., Starch storage in the stems of wheat plants: localization and temporal changes. *Annals of botany*, 2009. 103(6): p. 859-868.
- [249] Slewinski, T.L., Non-structural carbohydrate partitioning in grass stems: a target to increase yield stability, stress tolerance, and biofuel production. *Journal of Experimental Botany*, 2012. 63(13): p. 4647-4670.
- [250] Crowe, J.D., et al., Identification of developmental stage and anatomical fraction contributions to cell wall recalcitrance in switchgrass. *Biotechnol Biofuels*, 2017. 10: p. 184.

- [251] Yang, L., et al., PtrWRKY19, a novel WRKY transcription factor, contributes to the regulation of pith secondary wall formation in *Populus trichocarpa*. *Scientific reports*, 2016. 6(1): p. 18643.
- [252] Fu, C., et al., Overexpression of miR156 in switchgrass (*Panicum virgatum* L.) results in various morphological alterations and leads to improved biomass production. *Plant biotechnology journal*, 2012. 10(4): p. 443-452.
- [253] Chuck, G.S., et al., Overexpression of the maize *Corngrass1* microRNA prevents flowering, improves digestibility, and increases starch content of switchgrass. *Proceedings of the National Academy of Sciences*, 2011. 108(42): p. 17550-17555.
- [254] Akin, D.E., R.H. Brown, and L.L. Rigsby, Digestion of Stem Tissues in *Panicum* Species 1. *Crop Science*, 1984. 24(4): p. 769-773.
- [255] Sacks, E.J., et al., The gene pool of *Miscanthus* species and its improvement. *Genomics of the Saccharinae*, 2013: p. 73-101.
- [256] Zheng, Q., et al., Pretreatment of wheat straw leads to structural changes and improved enzymatic hydrolysis. *Scientific Reports*, 2018. 8(1).
- [257] Kristensen, J.B., et al., Cell-wall structural changes in wheat straw pretreated for bioethanol production. *Biotechnology for biofuels*, 2008. 1(1): p. 1-9.
- [258] Houshmand, S., et al., Microsatellite markers flanking a stem solidness gene on chromosome 3BL in durum wheat. *Molecular Breeding*, 2007. 20: p. 261-270.
- [259] Cook, J., et al., Identification of microsatellite markers associated with a stem solidness locus in wheat. *Crop Science*, 2004. 44(4): p. 1397-1402.
- [260] Appels, R., et al., International Wheat Genome Sequencing Consortium (IWGSC) Shifting the limits in wheat research and breeding through a fully annotated and anchored reference genome sequence. *Science*, 2018. 361: p. 6403.
- [261] Nilsen, K.T., et al., Copy number variation of *TdDof* controls solid-stemmed architecture in wheat. *Proc Natl Acad Sci U S A*, 2020. 117(46): p. 28708-28718.
- [262] Beres, B., et al., Host plant interactions between wheat germplasm source and wheat stem sawfly *Cephus cinctus* Norton (Hymenoptera: Cephidae) I. Commercial cultivars. *Canadian Journal of Plant Science*, 2013. 93(4): p. 607-617.
- [263] Beres, B., et al., Biology and integrated management of wheat stem sawfly and the need for continuing research. *The Canadian Entomologist*, 2011. 143(2): p. 105-125.
- [264] Schindelin, J., et al., Fiji: an open-source platform for biological-image analysis. *Nat Methods*, 2012. 9(7): p. 676-82.
- [265] García-Aparicio, M.P., et al., Xylanase contribution to the efficiency of cellulose enzymatic hydrolysis of barley straw. *Applied biochemistry and biotechnology*, 2007. 137: p. 353-365.
- [266] Wang, Q., et al., Cell wall disruption in low temperature NaOH/urea solution and its potential application in lignocellulose pretreatment. *Cellulose*, 2015. 22(6): p. 3559-3568.

- [267] Thomas, H.L., et al., Alkaline Pretreatments for Sorghum and Miscanthus Anaerobic Digestion: Impacts at Cell Wall and Tissue Scales. *BioEnergy Research*, 2022. 15(2).
- [268] Costa, T.H., et al., The enzymatic recalcitrance of internodes of sugar cane hybrids with contrasting lignin contents. *Industrial crops and products*, 2013. 51: p. 202-211.
- [269] Hatfield, R.D., J.R. Wilson, and D.R. Mertens, Composition of cell walls isolated from cell types of grain sorghum stems. *Journal of the Science of Food and Agriculture*, 1999. 79(6): p. 891-899.
- [270] Li, M., et al., Physical fractionation of sweet sorghum and forage/energy sorghum for optimal processing in a biorefinery. *Industrial Crops and Products*, 2018. 124: p. 607-616.
- [271] Wang, Q., et al., Comparative study of alkali and acidic cellulose solvent pretreatment of corn stover for fermentable sugar production. *BioResources*, 2016. 11(1): p. 482-491.
- [272] Thite, V.S. and A.S. Nerurkar, Valorization of sugarcane bagasse by chemical pretreatment and enzyme mediated deconstruction. *Scientific reports*, 2019. 9(1): p. 15904.
- [273] Donaldson, L., J. Hague, and R. Snell, Lignin distribution in coppice poplar, linseed and wheat straw. 2001.
- [274] Hansen, M.A., et al., Enzyme affinity to cell types in wheat straw (*Triticum aestivum* L.) before and after hydrothermal pretreatment. *Biotechnology for biofuels*, 2013. 6(1): p. 1-15.
- [275] Hansen, M.A., et al., Pretreatment and enzymatic hydrolysis of wheat straw (*Triticum aestivum* L.)—the impact of lignin relocation and plant tissues on enzymatic accessibility. *Bioresource technology*, 2011. 102(3): p. 2804-2811.
- [276] Zeng, M., et al., Microscopic examination of changes of plant cell structure in corn stover due to hot water pretreatment and enzymatic hydrolysis. *Biotechnology and bioengineering*, 2007. 97(2): p. 265-278.
- [277] Zeng, M., E. Ximenes, and M. Ladisch, Enzyme hydrolysis and imaging of fractionated corn stalk tissues pretreated with liquid hot water—Part I. *Biotechnology and Bioengineering*, 2012. 109: p. 390-397.
- [278] Dos Santos, A.C., et al., Lignin–enzyme interactions in the hydrolysis of lignocellulosic biomass. *Trends in biotechnology*, 2019. 37(5): p. 518-531.
- [279] Liao, J.C., et al., Fuelling the future: microbial engineering for the production of sustainable biofuels. *Nat Rev Microbiol*, 2016. 14(5): p. 288-304.
- [280] Darby, H.M. and J.G. Lauer, Harvest Date and Hybrid Influence on Corn Forage Yield, Quality, and Preservation. *Agronomy Journal*, 2002. 94(3).
- [281] Sanaullah, M., et al., Effects of drought and elevated temperature on biochemical composition of forage plants and their impact on carbon storage in grassland soil. *Plant and Soil*, 2013. 374(1-2): p. 767-778.

- [282] Emerson, R., et al., Drought effects on composition and yield for corn stover, mixed grasses, and Miscanthus as bioenergy feedstocks. *Biofuels*, 2014. 5(3): p. 275-291.
- [283] Stone, K.C., et al., The potential impacts of biomass feedstock production on water resource availability. *Bioresour Technol*, 2010. 101(6): p. 2014-25.
- [284] Langholtz, M., et al., Climate risk management for the U.S. cellulosic biofuels supply chain. *Climate Risk Management*, 2014. 3: p. 96-115.
- [285] Chaves, M.M., J.P. Maroco, and J.S. Pereira, Understanding plant responses to drought—from genes to the whole plant. *Functional plant biology*, 2003. 30(3): p. 239-264.
- [286] Oliver, R.J., J.W. Finch, and G. Taylor, Second generation bioenergy crops and climate change: a review of the effects of elevated atmospheric CO<sub>2</sub> and drought on water use and the implications for yield. *Gcb Bioenergy*, 2009. 1(2): p. 97-114.
- [287] Athmanathan, A., et al., A Demonstration of the Consistency of Maize Stover Pretreatment by Soaking in Aqueous Ammonia from Bench to Pilot-Scale. *BioEnergy Research*, 2018. 12(1): p. 68-80.
- [288] Agrawal, R., et al., Improved Enzymatic Hydrolysis of Pilot Scale Pretreated Rice Straw at High Total Solids Loading. *Frontiers in Energy Research*, 2018. 6.
- [289] Robertson, G.P., et al., Cellulosic biofuel contributions to a sustainable energy future: Choices and outcomes. *Science*, 2017. 356(6345).
- [290] Doran, P.M., *Mixing. Bioprocess Engineering Principles (Second Edition)*, Academic Press, 2013: p. 255-332.
- [291] Zhang, X., et al., High consistency enzymatic hydrolysis of hardwood substrates. *Bioresour Technol*, 2009. 100(23): p. 5890-7.
- [292] Pino, M.S., et al., Enhancement and modeling of enzymatic hydrolysis on cellulose from agave bagasse hydrothermally pretreated in a horizontal bioreactor. *Carbohydrate polymers*, 2019. 211: p. 349-359.
- [293] Du, J., et al., Enzymatic liquefaction and saccharification of pretreated corn stover at high-solids concentrations in a horizontal rotating bioreactor. *Bioprocess Biosyst Eng*, 2014. 37(2): p. 173-81.
- [294] Jung, Y.H., et al., Fed-Batch Enzymatic Saccharification of High Solids Pretreated Lignocellulose for Obtaining High Titrers and High Yields of Glucose. *Applied Biochemistry and Biotechnology*, 2017. 182(3): p. 1108-1120.
- [295] Geng, W., et al., Strategies to achieve high-solids enzymatic hydrolysis of dilute-acid pretreated corn stover. *Bioresour Technol*, 2015. 187: p. 43-48.
- [296] Tai, C., et al., Optimal control strategy for fed-batch enzymatic hydrolysis of lignocellulosic biomass based on epidemic modeling. *Biotechnol Bioeng*, 2015. 112(7): p. 1376-82.
- [297] Sanford, G.R., et al., Comparative productivity of alternative cellulosic bioenergy cropping systems in the North Central USA. *Agriculture, Ecosystems & Environment*, 2016. 216: p. 344-355.

- [298] Sanford, G.R., et al., Biomass Production a Stronger Driver of Cellulosic Ethanol Yield than Biomass Quality. *Agronomy Journal*, 2017. 109(5): p. 1911-1922.
- [299] Sluiter, J.B., et al., Compositional analysis of lignocellulosic feedstocks. 1. Review and description of methods. *J Agric Food Chem*, 2010. 58(16): p. 9043-53.
- [300] Serate, J., et al., Controlling microbial contamination during hydrolysis of AFEX-pretreated corn stover and switchgrass: effects on hydrolysate composition, microbial response and fermentation. *Biotechnol Biofuels*, 2015. 8: p. 180.
- [301] Yang, S., et al., Complete genome sequence and the expression pattern of plasmids of the model ethanologen *Zymomonas mobilis* ZM4 and its xylose-utilizing derivatives 8b and 2032. *Biotechnol Biofuels*, 2018. 11: p. 125.
- [302] Sato, T.K., et al., Directed Evolution Reveals Unexpected Epistatic Interactions That Alter Metabolic Regulation and Enable Anaerobic Xylose Use by *Saccharomyces cerevisiae*. *PLoS Genet*, 2016. 12(10): p. e1006372.
- [303] Ioelovich, M. and E. Morag, Study of enzymatic hydrolysis of pretreated biomass at increased solids loading. *Bioresources*, 2012. 7(4): p. 4672-4682.
- [304] Kirsch, C., S. Surendran, and I. Smirnova, Pressure Effects on Lignocellulose-Degrading Enzymes. *Chemical Engineering & Technology*, 2016. 39(4): p. 786-790.
- [305] Qu, X.-S., B.-B. Hu, and M.-J. Zhu, Enhanced saccharification of cellulose and sugarcane bagasse by *Clostridium thermocellum* cultures with Triton X-100 and  $\beta$ -glucosidase/Cellic®CTec2 supplementation. *RSC Advances*, 2017. 7(35): p. 21360-21365.
- [306] Rodrigues, A.C., et al., Celluclast and Cellic(R) CTec2: Saccharification/fermentation of wheat straw, solid-liquid partition and potential of enzyme recycling by alkaline washing. *Enzyme Microb Technol*, 2015. 79-80: p. 70-7.
- [307] Zhang, Y., et al., Production of hydrolysates from unmilled AFEX-pretreated switchgrass and comparative fermentation with *Zymomonas mobilis*. *Bioresource Technology Reports*, 2020. 11.
- [308] Jin, M., et al., Two-step SSCF to convert AFEX-treated switchgrass to ethanol using commercial enzymes and *Saccharomyces cerevisiae* 424A(LNH-ST). *Bioresour Technol*, 2010. 101(21): p. 8171-8.
- [309] Daoud, I. and B. Searle, On-line monitoring of brewery fermentation by measurement of CO<sub>2</sub> evolution rate. *Journal of the Institute of Brewing*, 1990. 96(5): p. 297-302.
- [310] El Haloui, N., D. Picque, and G. Corrieu, Alcoholic fermentation in winemaking: On-line measurement of density and carbon dioxide evolution. *Journal of Food Engineering*, 1988. 8(1): p. 17-30.
- [311] Xue, S., et al., Sugar loss and enzyme inhibition due to oligosaccharide accumulation during high solids-loading enzymatic hydrolysis. *Biotechnol Biofuels*, 2015. 8: p. 195.

- [312] Liguori, R., et al., Bioreactors for lignocellulose conversion into fermentable sugars for production of high added value products. *Appl Microbiol Biotechnol*, 2016. 100(2): p. 597-611.
- [313] Tengborg, C., M. Galbe, and G. Zacchi, Influence of enzyme loading and physical parameters on the enzymatic hydrolysis of steam-pretreated softwood. *Biotechnol Prog*, 2001. 17(1): p. 110-7.
- [314] Ong, R.G., et al., Pre-senescence Harvest of Switchgrass Inhibits Xylose Utilization by Engineered Yeast. *Frontiers in Energy Research*, 2018. 6.
- [315] Dickinson, Q., et al., Mechanism of imidazolium ionic liquids toxicity in *Saccharomyces cerevisiae* and rational engineering of a tolerant, xylose-fermenting strain. *Microb Cell Fact*, 2016. 15: p. 17.
- [316] Piotrowski, J.S., et al., Chemical genomic profiling via barcode sequencing to predict compound mode of action, in *Chemical biology*. 2015, Springer. p. 299-318.
- [317] Zeng, Y., M.E. Himmel, and S.Y. Ding, Visualizing chemical functionality in plant cell walls. *Biotechnol Biofuels*, 2017. 10: p. 263.
- [318] Berezin, M.Y. and S. Achilefu, Fluorescence lifetime measurements and biological imaging. *Chemical reviews*, 2010. 110(5): p. 2641-2684.
- [319] Albinsson, B., et al., The origin of lignin fluorescence. *Journal of Molecular Structure*, 1999. 508(1-3): p. 19-27.
- [320] Escamez, S., et al., Fluorescence lifetime imaging as an in situ and label-free readout for the chemical composition of lignin. *ACS Sustainable Chemistry & Engineering*, 2021. 9(51): p. 17381-17392.
- [321] Zoghلامي, A., et al., Multimodal characterization of acid-pretreated poplar reveals spectral and structural parameters strongly correlate with saccharification. *Bioresource technology*, 2019. 293: p. 122015.
- [322] Gierlinger, N., T. Keplinger, and M. Harrington, Imaging of plant cell walls by confocal Raman microscopy. *Nature protocols*, 2012. 7(9): p. 1694-1708.
- [323] Saletnik, A., B. Saletnik, and C. Puchalski, Overview of popular techniques of Raman spectroscopy and their potential in the study of plant tissues. *Molecules*, 2021. 26(6): p. 1537.
- [324] Gierlinger, N. and M. Schwanninger, The potential of Raman microscopy and Raman imaging in plant research. *Journal of Spectroscopy*, 2007. 21: p. 69-89.
- [325] Alonso-Simón, A., et al., High-throughput microarray profiling of cell wall polymers during hydrothermal pre-treatment of wheat straw. *Biotechnology and bioengineering*, 2010. 105(3): p. 509-514.
- [326] Baldwin, L., et al., External nitrogen input affects pre-and post-harvest cell wall composition but not the enzymatic saccharification of wheat straw. *Biomass and Bioenergy*, 2017. 98: p. 70-79.
- [327] Pingali, S.V., et al., Understanding multiscale structural changes during dilute acid pretreatment of switchgrass and poplar. *ACS Sustainable Chemistry & Engineering*, 2017. 5(1): p. 426-435.



- [328] Sun, Q., et al., Comparison of changes in cellulose ultrastructure during different pretreatments of poplar. *Cellulose*, 2014. 21: p. 2419-2431.

## 9 SUPPLEMENTARY INFORMATION

### 9.1 Imaging reactor

**Table 9.1-1. Composition of untreated, dry biomass and the residual biomass after dilute acid and dilute alkali pretreatment. Values are reported as mean  $\pm$  S.D, n=3.**

	Untreated (mg/g untreated dry biomass)	Dilute acid (mg/g untreated dry biomass)	Dilute alkali (mg/g untreated dry biomass)
Crystalline cellulose	523.01 $\pm$ 17.34	413.47 $\pm$ 16.15	496.53 $\pm$ 26.16
Glucose	44.18 $\pm$ 0.55	40.61 $\pm$ 2.01	51.68 $\pm$ 1.64
Xylose	297.12 $\pm$ 0.88	328.25 $\pm$ 3.42	298.88 $\pm$ 4.72
Arabinose	19.23 $\pm$ 0.01	37.12 $\pm$ 0.26	47.05 $\pm$ 1.82
Galactose	4.62 $\pm$ 0.03	7.38 $\pm$ 0.12	11.80 $\pm$ 0.52
Mannose	1.29 $\pm$ 0.03	1.01 $\pm$ 0.04	2.42 $\pm$ 0.04
Rhamnose	1.35 $\pm$ 0.01	1.65 $\pm$ 0.06	2.73 $\pm$ 0.04
Fucose	0.12 $\pm$ 0.00	0.28 $\pm$ 0.02	0.50 $\pm$ 0.02

**Table 9.1-2. Composition of pretreatment supernatant at different time points of dilute acid and dilute alkali pretreatment. Values are reported as mean  $\pm$  S.D, n=2.**

	Dilute acid pretreatment supernatant composition (g/L)			Dilute alkali pretreatment supernatant composition (g/L)		
	15 min	30 min	45 min	15 min	30 min	45 min
Acetate	0	0.12 $\pm$ 0.02	0	0.28 $\pm$ 0.001	0	0
Ethanol	0.27 $\pm$ 0.005	0.10 $\pm$ 0.002	0.08 $\pm$ 0.002	0	0.21 $\pm$ 0.004	0
Glucose	0.01 $\pm$ 0.0002	0	0	0	0	0
Glycerol	0	0.10 $\pm$ 0.0002	0	0.13 $\pm$ 0.003	0.15 $\pm$ 0.003	0.22 $\pm$ 0.004
Lactate	0	0	0	0.05 $\pm$ 0.001	0.08 $\pm$ 0.002	0.34 $\pm$ 0.007
Pyruvate	0.23 $\pm$ 0.005	0.19 $\pm$ 0.004	0	0.25 $\pm$ 0.005	0.54 $\pm$ 0.011	0.53 $\pm$ 0.011
Cellobiose	0	0	0	0.02 $\pm$ 0.0001	0.07 $\pm$ 0.001	0.01 $\pm$ 0.0002
Xylose	0	0.13 $\pm$ 0.003	0.12 $\pm$ 0.002	0.09 $\pm$ 0.002	0	0

Xylitol	0.012 ± 0.0001	0.03 ± 0.001	0.01 ± 0.0002	0.01 ± 0.0002	0.01 ± 0.0002	0.02 ± 0.0004
---------	-------------------	--------------	---------------	---------------	---------------	---------------

**Table 9.1-3. Hydrolysate concentration was analyzed using HPLC at different time points during the enzymatic hydrolysis of the pretreated samples. Values are reported as mean ± S.D. n=2.**

<b>Dilute acid hydrolysate composition (g/L)</b>							
	<b>15 min</b>	<b>30 min</b>	<b>4 hr</b>	<b>8 hr</b>	<b>12 hr</b>	<b>24 hr</b>	<b>48 hr</b>
Acetate	0.1575 ± 0.0001	0.1115 ± 0.0000	0.0907 ± 0.0001	0.0669 ± 0.0000	0.1122 ± 0.0001	0	0
Ethanol	0.0292 ± 0.0001	0.2177 ± 0.0001	0.2143 ± 0.0001	0	0.0844 ± 0.0002	0.2592 ± 0.0001	0.1727 ± 0.0001
Glucose	1.2574 ± 0.000	1.2857 ± 0.0000	1.7676 ± 0.0000	0.3229 ± 0.0000	0.0079 ± 0.0000	0	0
Glycerol	0.0231 ± 0.0000	0.0496 ± 0.0001	0.0192 ± 0.0000	0	0.074 ± 0.0002	0.0949 ± 0.0000	0.0948 ± 0.0000
Lactate	0.0246 ± 0.0000	0.0227 ± 0.0000	0	0	0	0	0
Pyruvate	0	0	0	0	0.1717 ± 0.0000	0.1877 ± 0.0001	0
Cellobiose	0.6764 ± 0.0000	0.6665 ± 0.0000	1.2321 ± 0.0001	0.1851 ± 0.0000	0	0	0
Xylose	0.6318 ± 0.0000	0.5962 ± 0.0001	1.0167 ± 0.0000	0.1111 ± 0.0001	0.0132 ± 0.0001	0	0.1109 ± 0.0002
Xylitol	0.0037 ± 0.0000	0	0.0069 ± 0.0002	0	0.0381 ± 0.0000	0.0548 ± 0.0000	0.0143 ± 0.0001

<b>Dilute alkali hydrolysate composition (g/L)</b>							
	<b>15 min</b>	<b>30 min</b>	<b>4 hr</b>	<b>8 hr</b>	<b>12 hr</b>	<b>24 hr</b>	<b>48 hr</b>
Acetate	0.0427 ± 0.0001	0.3085 ± 0.0000	0.2963 ± 0.0001	0.3847 ± 0.0001	0	0.0475 ± 0.0001	0
Ethanol	0.0496 ± 0.0000	0.3396 ± 0.0001	0.1425 ± 0.0001	0	0	0.0634 ± 0.0002	0.0248 ± 0.00001
Glucose	0	0	0	0	1.4803 ± 0.0002	1.3045 ± 0.0002	0
Glycerol	0	0.1435 ± 0.0000	0.1256 ± 0.0001	0.1835 ± 0.0000	0	0.0376 ± 0.0000	0

Lactate	0	0.0687 ± 0.0001	0.0706 ± 0.0000	0.066 ± 0.0000	0	0	0
Pyruvate	0	0.011 ± 0.0000	0.0193 ± 0.0000	0.1141 ± 0.0000	0	0	0
Cellobiose	0.0176 ± 0.0000	0.0152 ± 0.0001	0.0146 ± 0.0001	0.0152 ± 0.0000	0.8282 ± 0.0002	0.7088 ± 0.0001	0
Xylose	0	0.0526 ± 0.0001	0.0171 ± 0.0000	0	0.7422 ± 0.0000	0.6044 ± 0.0001	0
Xylitol	0	0.028 ± 0.0001	0.0282 ± 0.0000	0.0519 ±0.0001	0	0	0

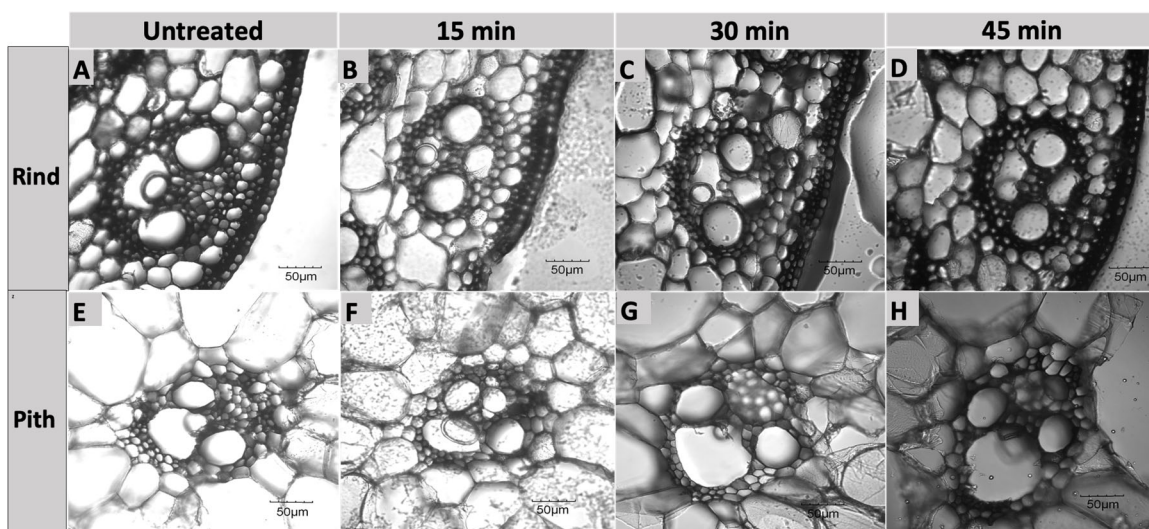


**Figure 9.1. Vascular bundles in the rind (A-D) and pith (E-H) regions did not show any significant structural changes after dilute acid pretreatment after 15 min (B, F), 30 min (C, G), and 45 min (D, H). Dilute acid pretreatment was performed on a 60 μm thick corn stem section using 1 M sulfuric acid at 100 °C.**

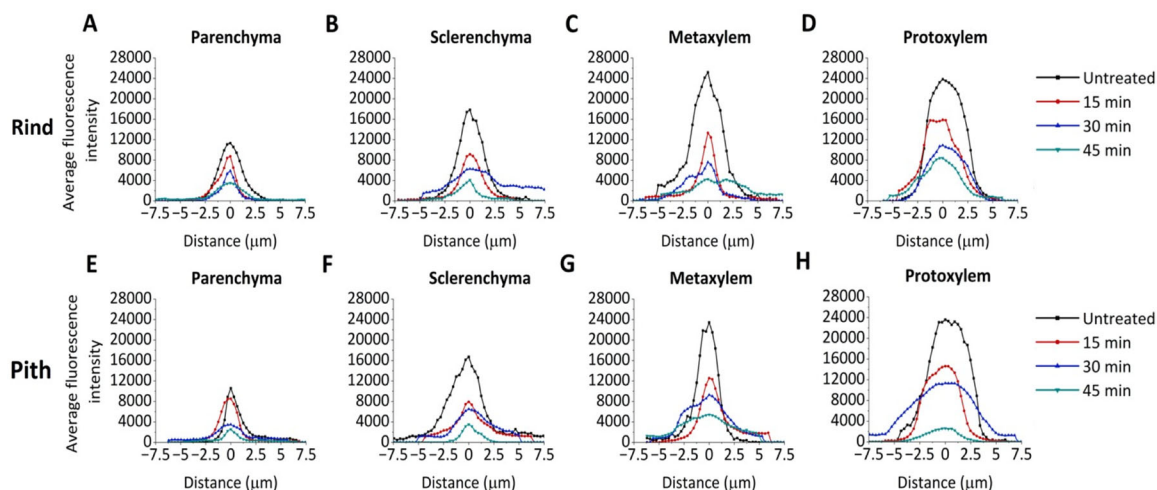


**Figure 9.2.** Different cell types in the rind (A-D) and pith (E-H) showed variation in initial fluorescence followed by rapid loss of fluorescence signals during the first 15 min of dilute alkali pretreatment using 62.5 mM NaOH.

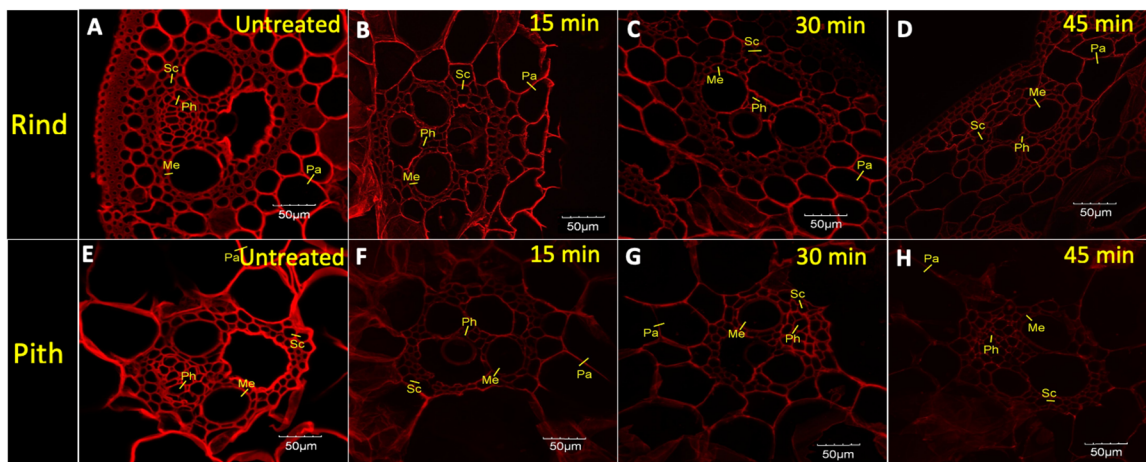


**Figure 9.3.** (A-D) CLSM images of a vascular bundle of corn stem in the rind region with immunolabeling for arabinoxylan using LM11 monoclonal antibody and Alexa Fluor 568 secondary antibody for untreated, 15 min, 30 min, and 45 min dilute acid pretreated samples. (E-F) CLSM images of a vascular bundle in the pith region with immunolabeling for arabinoxylan using LM11 monoclonal antibody and Alexa Fluor 568 secondary antibody for untreated, 15 min, 30 min, and 45 min dilute acid pretreated samples. The samples were excited using a 559 nm laser and with emission at 580-620 nm. The different cell types, including parenchyma (Pa), sclerenchyma (Sc), metaxylem (Me), and protoxylem (Pr) were selected as regions of interest (ROI) to quantify changes in the LM11 binding across the various samples.

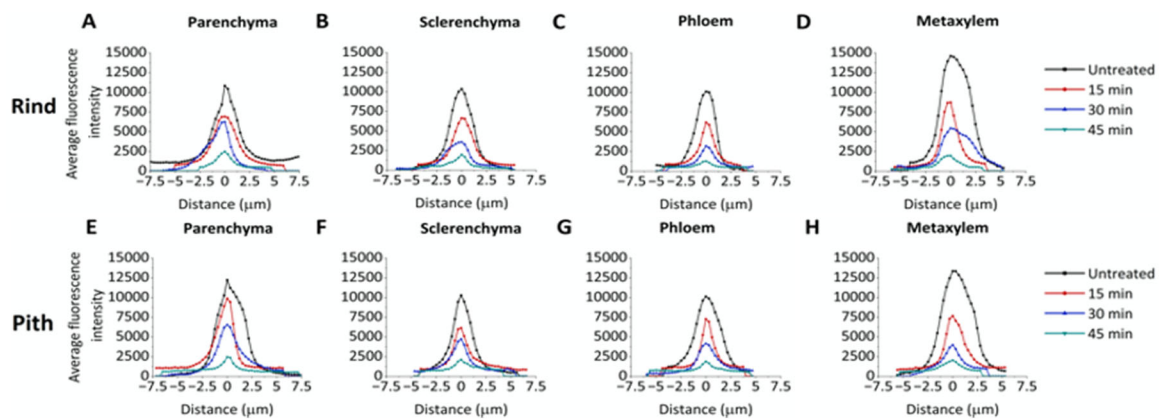


**Figure 9.4. Different cell types in the rind (A-D) and pith (E-H) did not show much variation in the LM11 fluorescence signals in the untreated samples, while there was a gradual loss of LM11 fluorescence signals for all cell types in the 15 min, 30 min, and 45 min dilute acid pretreated samples.**

## 9.2 Roller bottle

Table 9.2-1. Untreated feedstock composition for different types of cellulosic biomass.

Feedstock composition	2008 Corn stover (CS)	2014 Sorghum (SOR)	2010 Switchgrass (SG)	2012 Switchgrass (SG)	2014 Miscanthus (MSC)	2014 Restored prairie (RP)
Total structural sugars	59.15 ± 0.28	61.37 ± 0.15	60.41 ± 0.18	53.70 ± 0.39	65.99 ± 0.17	61.93 ± 0.51
Glucan	34.47 ± 0.16	37.19 ± 0.12	34.86 ± 0.11	30.35 ± 0.39	41.28 ± 0.11	36.97 ± 0.48
Xylan	20.17 ± 0.23	20.54 ± 0.06	21.60 ± 0.13	18.98 ± 0.04	21.39 ± 0.11	20.40 ± 0.15
Galactan	2.90 ± 0.03	0.91 ± 0.01	1.48 ± 0.03	1.62 ± 0.03	1.09 ± 0.03	1.45 ± 0.06
Arabinan	1.61 ± 0.04	1.83 ± 0.03	2.47 ± 0.03	2.76 ± 0.01	2.17 ± 0.05	2.05 ± 0.03
Mannan	NM*	0.9 ± 0.08	NM*	ND**	0.05 ± 0.0	1.06 ± 0.05
Acetyl groups	2.60 ± 0.10	2.50 ± 0.11	2.58 ± 0.11	2.15 ± 0.06	2.24 ± 0.03	2.63 ± 0.03
Lignin	13.79 ± 0.27	16.18 ± 0.17	18.59 ± 0.11	15.38 ± 0.06	20.13 ± 0.54	18.98 ± 0.34
Acid insoluble lignin (Klason lignin)	12.45 ± 0.05	15.21 ± 0.17	17.87 ± 0.10	14.31 ± 0.06	19.12 ± 0.54	17.86 ± 0.34
Acid soluble lignin	1.35 ± 0.26	0.97 ± 0.02	0.73 ± 0.03	1.07 ± 0.01	1.01 ± 0.01	1.12 ± 0.03
Protein	3.72 ± 0.03	2.87 ± 0.15	3.19 ± 0.09	4.65 ± 0.08	2.54 ± 0.09	3.19 ± 0.11
Ash	6.28 ± 0.17	5.27 ± 0.05	5.56 ± 0.16	5.47 ± 0.08	3.98 ± 0.09	5.45 ± 0.10
Total extractives	19.04 ± 0.16	18.53 ± 0.11	14.90 ± 0.26	22.14 ± 0.21	8.74 ± 0.07	11.34 ± 0.13

\* NM= not measured

\*\*ND= not detected

Table 9.2-2. Summary of *Saccharomyces cerevisiae* Y945 fermentation results. Values are reported as the mean  $\pm$  s.d. (n=3 or 4).

	2008 CS	2010 SG	2012 SG	2014 MG	2014 RP	2014 SO
<b>Roller Bottle</b>						
Final OD	5.1 $\pm$ 0.4	4.1 $\pm$ 0.3	6.1 $\pm$ 0.5	5.3 $\pm$ 1.4	5.0 $\pm$ 0.0	5.4 $\pm$ 0.1
Glucose Consumption (%)	100 $\pm$ 0.0	100 $\pm$ 0	99.9 $\pm$ 0.3	100 $\pm$ 0	100 $\pm$ 0	100 $\pm$ 0
Xylose Consumption (%)	27.1 $\pm$ 2.4	38.2 $\pm$ 5.5	39.6 $\pm$ 14.2	44.6 $\pm$ 16.8	35.1 $\pm$ 2.5	51.1 $\pm$ 24.2
Glucose Consumption (g/L)	60.4 $\pm$ 0.8	49.2 $\pm$ 6.2	45.8 $\pm$ 0.6	46.2 $\pm$ 2.6	46.8 $\pm$ 2.3	53.6 $\pm$ 6.6
Xylose Consumption (g/L)	7.9 $\pm$ 0.8	13.3 $\pm$ 2.8	11.5 $\pm$ 4.2	12.4 $\pm$ 3.8	11.1 $\pm$ 1.1	15.3 $\pm$ 7.4
Ethanol Produced (g/L)	27.6 $\pm$ 1.4	21.9 $\pm$ 1.8	25.0 $\pm$ 2.1	22.3 $\pm$ 1.8	22.0 $\pm$ 0.4	25.8 $\pm$ 3.4
Process Ethanol Yield (%) <sup>§</sup>	60.7 $\pm$ 3.9	51.8 $\pm$ 9.3	65.4 $\pm$ 4.8	59.0 $\pm$ 8.4	55.1 $\pm$ 1.4	61.2 $\pm$ 10.3
Metabolic Ethanol Yield (%) <sup>‡</sup>	79.4 $\pm$ 5.0	69.8 $\pm$ 13.9	85.5 $\pm$ 3.2	74.5 $\pm$ 5.7	74.7 $\pm$ 3.1	74.2 $\pm$ 9.3
Maximum Rate of CO <sub>2</sub> Production ( $\mu$ L/hr)	1.6 $\pm$ 0.1	1.7 $\pm$ 0.2	2.0 $\pm$ 0.3	1.4 $\pm$ 0.1	1.7 $\pm$ 0.3	1.8 $\pm$ 0.3
Time to Maximum Rate of CO <sub>2</sub> Production (hr)	17.0 $\pm$ 7.2	10.2 $\pm$ 0.8	27.6 $\pm$ 5.0	10.9 $\pm$ 1.6	9.4 $\pm$ 0.1	10.1 $\pm$ 1.5
Time to Maximum Volume (hr)	36.2 $\pm$ 6.1	27.8 $\pm$ 8.8	42.6 $\pm$ 0.5	29.6 $\pm$ 13.4	25.7 $\pm$ 0	35.2 $\pm$ 8.7
Volume of CO <sub>2</sub> at Maximum Rate (mL)	35.9 $\pm$ 4.3	34.1 $\pm$ 0.8	32.0 $\pm$ 9.7	25.3 $\pm$ 7.2	27.2 $\pm$ 4.7	29.9 $\pm$ 3.4
Maximum CO <sub>2</sub> Volume (mL)	53.9 $\pm$ 4.6	50.1 $\pm$ 2.7	47.7 $\pm$ 10.2	40.4 $\pm$ 7.7	37.8 $\pm$ 3.5	52.4 $\pm$ 12.0
<b>Shake Flask</b>						
Final OD	3.6 $\pm$ 2.2	5 $\pm$ 0.6	3.1 $\pm$ 2.2	4.9 $\pm$ 0.3	4.7 $\pm$ 0.3	5.8 $\pm$ 1.7
Glucose Consumption (%)	75.1 $\pm$ 49.9	100 $\pm$ 0.0	60.6 $\pm$ 43.9	100 $\pm$ 0.0	100 $\pm$ 0.0	100 $\pm$ 0.0



Xylose Consumption (%)	8.6 ± 11.5	27.0 ± 8.0	-3.6 ± 5.1	21.9 ± 6.6	37.7 ± 4.2	23.1 ± 12.3
Glucose Consumption (g/L)	47.9 ± 32.0	48.2 ± 2.0	28.5 ± 20.7	53.6 ± 0.8	44.5 ± 0.7	55.9 ± 0.5
Xylose Consumption (g/L)	3.0 ± 3.9	9.1 ± 2.8	-1.2 ± 1.7	7.5 ± 2.3	11.5 ± 1.1	7.6 ± 4.0
Ethanol Produced (g/L)	24.1 ± 16.2	27.3 ± 2.4	15.4 ± 10.7	28.2 ± 1.3	25.6 ± 1.2	29.9 ± 2.4
Process Ethanol Yield (%) <sup>§</sup>	48.6 ± 32.3	65.4 ± 4.2	37.9 ± 26.2	63.2 ± 3.5	66.9 ± 4.1	65.8 ± 5.6
Metabolic Ethanol Yield (%) <sup>‡</sup>	72.6 ± 44.1	93.4 ± 3.2	115.6 ± 12.8	90.9 ± 7.3	89.6 ± 3.7	92.1 ± 2.5
Maximum Rate of CO <sub>2</sub> Production (μL/hr)	1.3 ± 0.6	1.9 ± 0.1	1.4 ± 0.6	1.6 ± 0.1	1.8 ± 0.3	1.7 ± 0.4
Time to Maximum Rate of CO <sub>2</sub> Production (hr)	17.8 ± 15.5	12.2 ± 2.5	42.0 ± 0.0	19.5 ± 3.6	11.3 ± 1.5	11.6 ± 1.5
Time to Maximum Volume (hr)	28.2 ± 13.9	35.7 ± 5.4	42.6 ± 0.5	35.9 ± 5.8	35.7 ± 5.5	31.6 ± 5.1
Volume of CO <sub>2</sub> at Maximum Rate (mL)	33.0 ± 21.5	37.3 ± 3.0	26.8 ± 15.7	33.1 ± 3.5	34.4 ± 1.4	34.2 ± 4.2
Maximum CO <sub>2</sub> Volume (mL)	49.2 ± 31.5	56.3 ± 0.1	29.5 ± 17.3	50.0 ± 5.9	51.9 ± 9.1	56.7 ± 12.2

<sup>‡</sup>The metabolic yield is the ratio of sugars (glucose and xylose) consumed during fermentation to ethanol produced assuming 0.51 g ethanol/g sugars as the theoretical maximum.

<sup>§</sup>The process yield is the ratio of sugars initially present in the hydrolysate (glucose and xylose) to ethanol produced assuming 0.51 g ethanol/g sugars as the theoretical maximum.

**Table 9.2-3. Summary of *Zymomonas mobilis* 2032 fermentation results. Values are reported as the mean  $\pm$  s.d. (n=3 or 4).**

	2008 CS	2010 SG	2012 SG	2014 MG	2014 RP	2014 SO
<b>Roller Bottle</b>						
Final OD	2.7 $\pm$ 1.4	3.0 $\pm$ 0.2	2.9 $\pm$ 0.6	3.3 $\pm$ 0.5	3.8 $\pm$ 0.3	3.4 $\pm$ 0.5
Glucose Consumption (%)	78.5 $\pm$ 43.0	100 $\pm$ 0.0	100 $\pm$ 0.0	100 $\pm$ 0.0	100 $\pm$ 0.0	100 $\pm$ 0.0
Xylose Consumption (%)	51.0 $\pm$ 32.8	90.1 $\pm$ 4.8	75.4 $\pm$ 20.0	81.7 $\pm$ 10.1	86.7 $\pm$ 0.5	81.8 $\pm$ 2.3
Glucose Consumption (g/L)	47.4 $\pm$ 25.9	49.2 $\pm$ 6.2	45.8 $\pm$ 0.8	45.5 $\pm$ 2.5	46.8 $\pm$ 2.3	53.6 $\pm$ 6.6
Xylose Consumption (g/L)	14.7 $\pm$ 9.4	31.4 $\pm$ 4.4	21.8 $\pm$ 5.6	22.7 $\pm$ 4.2	27.4 $\pm$ 0.7	24.3 $\pm$ 3.3
Ethanol Produced (g/L)	26.1 $\pm$ 16.7	31.8 $\pm$ 0.5	30.0 $\pm$ 2.2	29.3 $\pm$ 3.0	33.2 $\pm$ 0.4	32.0 $\pm$ 0.8
Process Ethanol Yield (%) <sup>§</sup>	57.4 $\pm$ 37.0	74.9 $\pm$ 9.1	78.8 $\pm$ 6.0	78.4 $\pm$ 4.0	83.2 $\pm$ 2.5	76.3 $\pm$ 10.2
Metabolic Ethanol Yield (%) <sup>‡</sup>	69.5 $\pm$ 31.8	78.3 $\pm$ 10.9	87.1 $\pm$ 0.9	84.2 $\pm$ 1.9	87.9 $\pm$ 2.5	81.6 $\pm$ 11.6
Maximum Rate of CO <sub>2</sub> Production ( $\mu$ L/hr)	1.2 $\pm$ 0.6	1.8 $\pm$ 0.1	1.7 $\pm$ 0.6	1.5 $\pm$ 0.1	1.9 $\pm$ 0.1	1.8 $\pm$ 0.1
Time to Maximum Rate of CO <sub>2</sub> Production (hr)	16 $\pm$ 13.2	14.9 $\pm$ 4.8	16.3 $\pm$ 4.7	21.8 $\pm$ 6.6	11.9 $\pm$ 0.1	15.4 $\pm$ 3.4
Time to Maximum Volume (hr)	39.4 $\pm$ 3.9	39.6 $\pm$ 4.7	37.2 $\pm$ 9.1	38.2 $\pm$ 4.7	36.2 $\pm$ 0.5	38.6 $\pm$ 3.3
Volume of CO <sub>2</sub> at Maximum Rate (mL)	28.6 $\pm$ 18.9	35.9 $\pm$ 2.8	36.0 $\pm$ 14.1	38.5 $\pm$ 5.1	35.2 $\pm$ 3.2	39.2 $\pm$ 5.0
Maximum CO <sub>2</sub> Volume (mL)	45.3 $\pm$ 27.1	60.1 $\pm$ 2.1	55.8 $\pm$ 17.1	53.2 $\pm$ 5.9	54.3 $\pm$ 5.9	59.0 $\pm$ 6.3
<b>Shake Flask</b>						
Final OD	2.2 $\pm$ 1.1	2.8 $\pm$ 0.4	3.0 $\pm$ 0.3	2.6 $\pm$ 1.0	3.6 $\pm$ 0.5	3.3 $\pm$ 0.7
Glucose Consumption (%)	73.6 $\pm$ 45.7	100 $\pm$ 0.0	100 $\pm$ 0.0	75.5 $\pm$ 40.7	100 $\pm$ 0.0	100 $\pm$ 0.0
Xylose Consumption (%)	35.0 $\pm$ 22.3	76.8 $\pm$ 10	72.1 $\pm$ 3.5	23.4 $\pm$ 26	85.9 $\pm$ 2.2	62.5 $\pm$ 12.4
Glucose Consumption (g/L)	46.5 $\pm$ 28.5	48.2 $\pm$ 2.0	47.5 $\pm$ 0.8	40.3 $\pm$ 21.5	44.5 $\pm$ 0.7	55.9 $\pm$ 0.5

Xylose Consumption (g/L)	11.5 ± 7.1	25.8 ± 3.6	23.8 ± 1.4	7.9 ± 8.8	26.3 ± 1.1	20.6 ± 3.7
Ethanol Produced (g/L)	27.5 ± 19.3	35.7 ± 2.1	35.3 ± 0.3	24.1 ± 14.2	34.5 ± 2.1	37.4 ± 3.0
Process Ethanol Yield (%) <sup>§</sup>	56.2 ± 39.9	85.7 ± 2.5	86.1 ± 1.8	54.2 ± 32.1	90.0 ± 5.2	82.5 ± 6.8
Metabolic Ethanol Yield (%) <sup>‡</sup>	84.5 ± 20.9	94.8 ± 2.8	97.2 ± 3.1	96.7 ± 4.5	95.5 ± 4.7	95.8 ± 2.4
Maximum Rate of CO <sub>2</sub> Production (μL/hr)	1.1 ± 0.4	1.6 ± 0.2	1.5 ± 0.3	1.3 ± 0.4	1.9 ± 0.1	1.6 ± 0.1
Time to Maximum Rate of CO <sub>2</sub> Production (hr)	16.3 ± 14.0	17.9 ± 5.0	19.1 ± 5.7	37.7 ± 7.0	18.5 ± 2.5	18.8 ± 6.9
Time to Maximum Volume (hr)	42.6 ± 0.4	41.4 ± 2.1	42.3 ± 1.0	42.6 ± 0.3	41.9 ± 0.4	42.1 ± 0.3
Volume of CO <sub>2</sub> at Maximum Rate (mL)	30.3 ± 24.9	40.6 ± 1.3	34.5 ± 4.3	36.0 ± 10.4	41.0 ± 4.2	39.6 ± 4.1
Maximum CO <sub>2</sub> Volume (mL)	51.7 ± 30.7	64.7 ± 2.0	57.0 ± 9.1	43.2 ± 17.9	62.3 ± 4.2	64.2 ± 5.0

<sup>‡</sup>The metabolic yield is the ratio of sugars (glucose and xylose) consumed during fermentation to ethanol produced assuming 0.51 g ethanol/g sugars as the theoretical maximum.

<sup>§</sup>The process yield is the ratio of sugars initially present in the hydrolysate (glucose and xylose) to ethanol produced assuming 0.51 g ethanol/g sugars as the theoretical maximum.

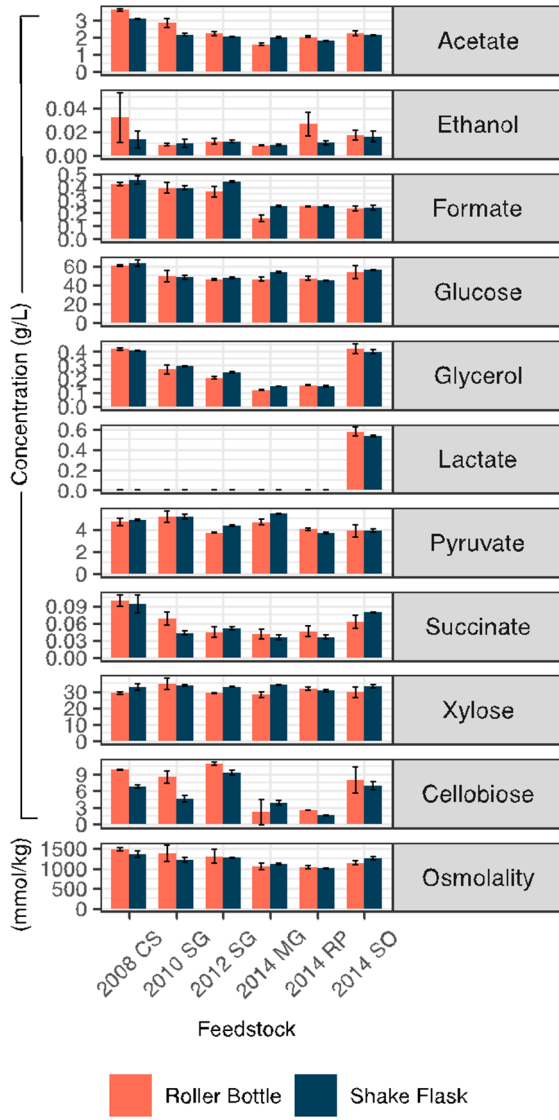


**Figure 9.5. Roller Bottle and shake flask hydrolysate composition. Bars represent the average with error bars as  $\pm$  standard deviation.**

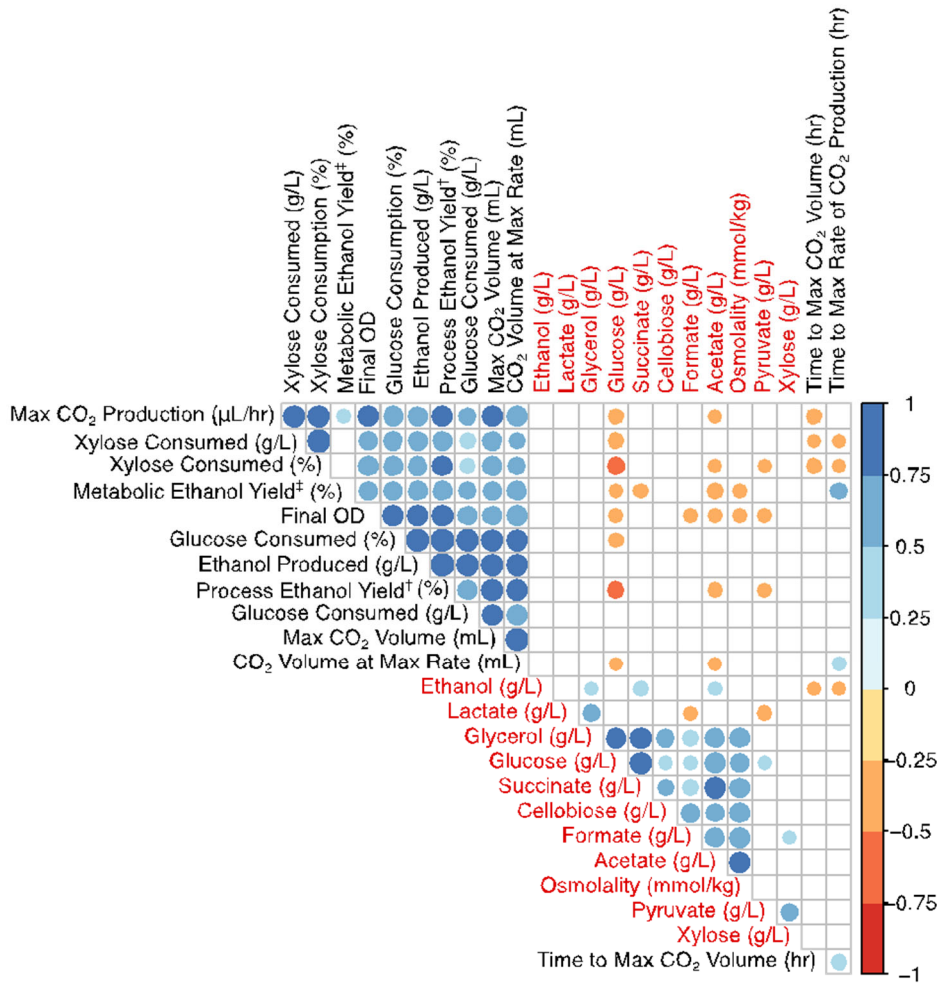


**Figure 9.6. Clustered correlation matrix for *Z. mobilis* 2032 fermentation data and hydrolysate composition (red text labels). The plot was generated using the corrplot package in R with hclust (hierarchical clustering order). The size and color correspond to the direction and magnitude of the correlation. Correlations that were insignificant ( $p < 0.05$ ) were not plotted.**

## A Copyrights documentation

### A.1 A high solids field-to-fuel research pipeline to identify interactions between feedstocks and biofuel production. Biotechnology for biofuels

7/10/23, 4:08 PM

Creative Commons — Attribution 4.0 International — CC BY 4.0

This page is available in the following languages:



**Creative Commons License De**  
Attribution 4.0 International (CC BY 4.0)



This is a human-readable summary of (and not a substitute for) the [license](#).

### You are free to:

**Share** — copy and redistribute the material in any medium or format

**Adapt** — remix, transform, and build upon the material

for any purpose, even commercially.

The licensor cannot revoke these freedoms as long as you follow the license terms.

### Under the following terms:



**Attribution** — You must give appropriate credit, provide a link to the license, and indicate if changes were made. You may do so in any reasonable manner, but not in any way that suggests the licensor endorses you or your use.

**No additional restrictions** — You may not apply legal terms or technological measures that legally restrict others from doing anything the license permits.

### Notices:

You do not have to comply with the license for elements of the material in the public domain or where your use is permitted by an applicable exception or limitation.

No warranties are given. The license may not give you all of the permissions necessary for your intended use. For example, other rights such as publicity, privacy, or moral rights may limit how you use the material.

<https://creativecommons.org/licenses/by/4.0/>

1/1